A UNIFIED FUEL SPRAY BREAKUP MODEL FOR INTERNAL COMBUSTION ENGINE APPLICATIONS

by

Christos Chryssakis

A dissertation submitted in partial fulfillment
of the requirements for the degree of
Doctor of Philosophy
(Mechanical Engineering)
in The University of Michigan
2005

Doctoral Committee:

Professor Dionissios N. Assanis, Chair
Professor Bram van Leer
Professor Volker Sick
Ales Alajbegovic, Exa Corporation

ACKNOWLEDGEMENTS

I would like to thank my advisor, Professor Dennis Assanis, for offering me the opportunity to work in his group at the W.E. Lay Automotive Laboratory and guiding me through my research over the last 5 years. I would also like to thank him for introducing me to experts in the field and making it possible to work with them.

I was very fortunate to meet Professor Gerard Faeth during my studies. His knowledge of spray atomization and his willingness to spend time with students and provide insight on his work has been crucial for my understanding of the physical processes in sprays. I appreciate the help of Professor Bram van Leer who served in my committee after Prof. Faeth’s unexpected passing away in January of 2005.

I would like to thank Professor Volker Sick for his assistance during my graduate studies, starting from my first paper to his last comments on my thesis. His expertise on experimental techniques has been very valuable for my understanding of the experimental data I have used in my work.

I am also thankful to Dr. Ales Alajbegovic for serving in my committee and providing guidance, encouragement in difficult times, and an industrial point of view.

I am very appreciative to have worked with Professor Keiya Nishida and Dr. Jeekuen Lee during my visit at the University of Hiroshima in June of 2002. The experimental data they provided have been very valuable for the completion both of my M.Sc. and my Ph.D. work. Professor Nishida’s assistance and friendship have been very important to me.

I was also very fortunate to be invited to work with Professor Choongsik Bae and Dr. Sanghoon Kook, in KAIST, in South Korea, in August of 2004. The quality of their

work and the experimental data they provided have been of great value for the validation of my computational model.

In addition, I would like to thank all my friends and colleagues in the W.E. Lay Automotive Lab., for making my stay here an enjoyable one. I am especially thankful to Aris Babajimopoulos, Ronald Grover and Bruno Vanzieleghem for helping me in my first steps of my research and for being very good friends as well. Dr. Zoran Filipi has also been a very significant source of advice, a great colleague and friend. I also appreciate the assistance from Dr. George Lavoie and his advice on both scientific and photographic questions. Finally, Susan Clair and Janet Lyons, for handling all the administrative work and my frequent travel expense reports.

Last, but definitely not least, I would like to thank my family and my friends in Greece and in Michigan for their help, support, and encouragement during the last 5 years.

TABLE OF CONTENTS

LIST OF FIGURES

LIST OF TABLES

LIST OF SYMBOLS

B_o, B_1	empirical constants, WAVE model
C_1-C_4	empirical constants for primary breakup model
C_c	empirical constant
C_D	aerodynamic drag coefficient
C_k, C_d C_b, C_f	empirical constants, TAB model
d	diameter
d_L	ligament diameter
D_p	diameter of parcel representing the liquid core
E	aspect ratio
$\dot{E}$	energy, DDB model
Eo	Eotvös number
F	external force
G	surface acceleration
h	film thickness
k	wave number
k_1	constant controlling the primary breakup rate
k_{avg}	average turbulent kinetic energy
K_{br}	breakup constant, E-TAB model
K_C	loss coefficient in the contraction corner
K_V	nozzle discharge coefficient
L	length
L_A	atomization length scale

L_t	turbulence length scale
L_w	wavelength of surface perturbation
m	mass
MMD	Mass Median Diameter
n	number of droplets
Oh	Ohnesorge number
Q	air-fuel density ratio
r	radius
r_{32}	Sauter Mean Radius (SMR)
Re	Reynolds number
s	area ratio at the nozzle contraction
SMD	Sauter Mean Diameter
t	time
t^*	characteristic time
U,u	velocity
V	volume
$\dot{W}$	work, DDB model
We	Weber number
y	dimensionless drop deformation

Greek Symbols

α	local acceleration of the drop
Γ	gamma function
ε_{avg}	average energy dissipation rate
η_o	initial amplitude of disturbance
θ	spray angle
Λ	wavelength corresponding to Ω

μ	viscosity
ν	kinematic viscosity
ρ	density
σ	surface tension
τ	breakup time for liquid sheet
τ_A	atomization time scale
τ_t	turbulence time scale
τ_w	wave growth time scale
ω	wave growth rate
Ω	maximum wave growth rate

Subscripts

c	cross-section
G	gas
L	liquid
max	maximum
min	minimum
o	original/initial

ABSTRACT

A unified approach towards modeling fuel sprays for internal combustion engines has been developed in this work. Based on a Lagrangian approach, the fuel injection process has been divided in three main subprocesses: primary atomization, drop deformation and aerodynamic drag, and secondary atomization. Two different models have been used for the primary atomization, depending on whether a high-pressure swirl atomizer or a multi-hole nozzle is used. The drop deformation and secondary atomization have been modeled based on the physical properties of the system, independent of the way the droplets were created. The secondary atomization has been further divided into four breakup regimes, based on experimental observations reported in the literature.

The model has been validated using a wide array of experimental conditions, ranging from gasoline to diesel sprays. For both types of sprays, low and high ambient pressures have been used, and for the diesel sprays different injection pressures have also been utilized. Finally, the capabilities of the model are illustrated by presenting gasoline and diesel engine simulations. Overall, the model performs satisfactorily, without the need for recalibration for each condition. Small discrepancies between model predictions and experimental measurements are observed for some cases, but they can be principally attributed to uncertainties in the boundary conditions and the primary breakup modeling.

CHAPTER 1

INTRODUCTION

The advantages and challenges of direct fuel injection in internal combustion engines are discussed in this chapter. A short overview of the spray atomization mechanisms is presented as well as the main characteristics of computational models currently used for fuel injection simulations. Finally, the problem statement and the overview of the following chapters are given.

1.1 Motivation – Direct Injection Engines

The design of more powerful, fuel-efficient, and environmentally friendly internal combustion engines is currently one of the main goals of engine researchers and manufacturers worldwide. With the advent of greater customer demands and increasingly stringent fuel consumption and emission standards, engine manufacturers face the challenging task of delivering conventional vehicles that abide by, or exceed, these regulations and expectations. These objectives are currently met by expanding the existing technologies and adopting new concepts, while ensuring that the standards set by governmental regulations and market demand are satisfied. The manner in which these technologies are applied varies according to national regulatory requirements imposed in various countries.

Direct injection gasoline and diesel engines have advantages of high thermal efficiency and low fuel consumption and are penetrating the passenger vehicle market at a fast pace. The essential feature of a diesel engine is the direct fuel injection into the engine cylinder toward the end of the compression stroke [Heywood, 1988]. The liquid fuel, injected at high velocity as one or more jets through small orifices in the injector tip, atomizes into small drops, evaporates, mixes with the high-temperature, high-pressure cylinder air and ignites. Some important consequences of this combustion process on engine operation are the following: (a) there is no knock limit, hence a higher compression ratio can be used improving the fuel conversion efficiency of the engine, (b) since the engine torque is controlled by varying the amount of fuel injected per cycle, the engine can be operated unthrottled, (c) because the diesel engine always operates with lean equivalence ratios, the effective value of the specific heat ratio, γ, over the expansion process is higher than in a stoichiometric charge, increasing the fuel conversion efficiency. The direct-fuel-injection concept in spark ignition engines has similar effects, but there is an additional challenge of achieving an appropriate stratified mixture, stoichiometric in the vicinity of the spark plug and lean elsewhere.

The major challenge in both diesel and gasoline direct-injected systems is the air utilization during combustion, which can lead to the formation of excessive amounts of soot that cannot be burned up prior to exhaust. The high temperatures developed locally in the combustion chamber can also lead to high NO_x formation rates, while the liquid wall films from the fuel spray impinging of the piston or cylinder walls can lead to unburned HC emissions. Hence, the injection and mixing processes have to be understood and optimized to achieve optimum engine performance with minimum pollutant emissions generation. The high flexibility of modern common rail injection systems in injection timing, pressure and number of injections enables emissions reduction without significantly sacrificing fuel economy. Computational models can be a valuable tool to gain insight on in-cylinder mixing phenomena and investigate injection strategies capable of minimizing harmful pollutants without compromising fuel economy. Optical diagnostic studies in constant volume bombs and in optical engines also offer insight on fuel injection, mixing and combustion processes and they can also be used to provide measurements for validation of Computational Fluid Dynamics (CFD) models.

1.2 Fuel Spray Formation and Breakup

Fuel sprays used in internal combustion engines are produced in many different ways, depending on the application and the requirements of each application. There are three basic processes associated with all methods of atomization; namely the internal flow in the nozzle, the primary and the secondary atomization processes. All these characteristics of the spray depend on the internal geometry of the nozzle, the injection pressure and the pressure and temperature conditions in the combustion chamber.

The *internal flow* in the nozzle includes flow separation and reattachment phenomena and in the limit cavitation that strongly enhance turbulence levels and the gas/liquid interface at the exit of the nozzle, which in turn affects atomization [Berg et al., 2005]. Additionally, the design of the nozzle has a major effect on the structure of the spray and its properties. A multi-hole injector nozzle, such as those used for diesel applications, results in dense solid-cone sprays favoring a stratified charge. On the other hand, swirl and fan injectors, typically used in Direct-Injection Spark-Ignition (DISI) engines, lead to a more disperse spray appropriate for a homogeneous or stratified charge.

The *primary atomization* of the spray also depends directly on the internal geometry of the nozzle and the internal flow phenomena, which dictate the structure of the emerging fluid. This structure can vary from a liquid core for diesel sprays to a liquid sheet (either flat or conical). These structures interact with the ambient gas and result in liquid fragmentation starting with large ligaments that further disintegrate into spherical droplets.

Once spherical drops are created, after the primary atomization has been completed, the *secondary atomization* starts and its governing mechanisms are common for any type of spray. It only depends on the initial droplet sizes, velocities and physical properties of the system, which are represented by the Weber and Ohnesorge numbers, as will be explained later. These parameters determine the breakup mechanism under which a droplet will further disintegrate. Even though in a given spray a certain mechanism may be dominant, it is most likely that more than one mechanism will be relevant and they all have to be modeled successfully. This is illustrated in Figure 1, where the four secondary atomization mechanisms are shown, along with their applicability for gasoline and diesel sprays. The fact that breakup mechanisms are independent of the primary atomization process, offers the flexibility of developing a breakup model that will be able to handle all possible cases if appropriate criteria can be established.

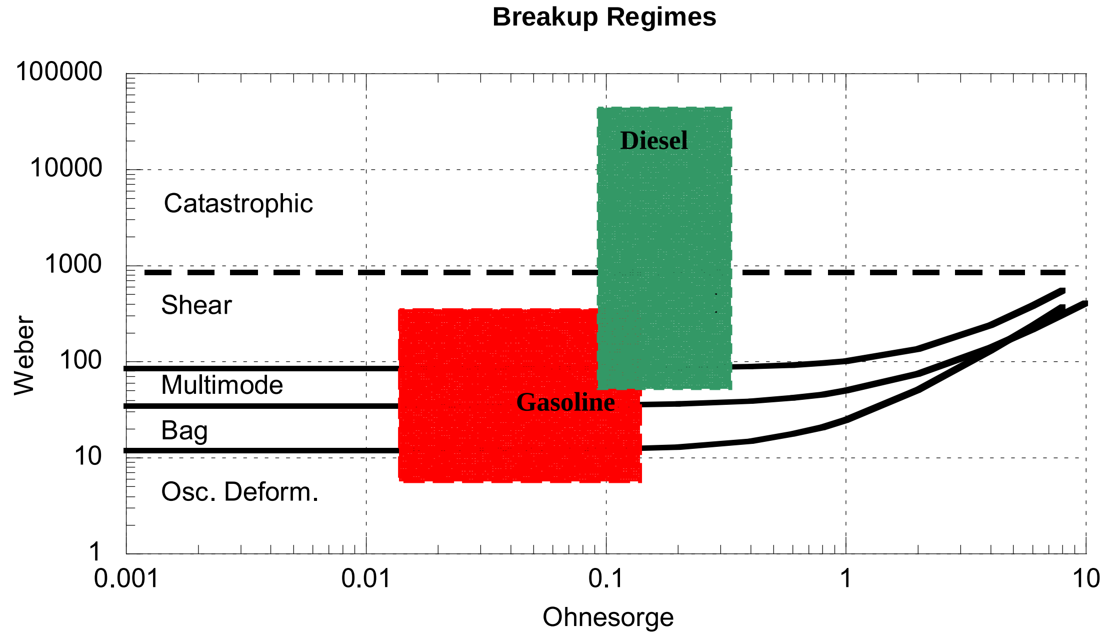

Figure 1: Breakup Regimes for various fuel sprays.

1.3 Modeling of Reactive Flows and Sprays for Internal Combustion Engine Simulations

Along with experimental studies that focus on understanding the spray structure, breakup mechanisms, evaporation rates and wall impingement effects, numerical investigations are also being conducted and in many cases offer great advantages to the researchers. CFD has become an established tool for the design and understanding of physical systems including fluid flows and/or combustion processes. Multidimensional models have proven their value in reducing the need for physical experimentation, the benefit of which has been a reduction in product development time and cost. Main benefit from numerical simulations is the possibility to conduct parametric studies and investigate the effect of various factors on engine operation, power output and emissions formation. In addition, CFD can be used in conjunction with experiments to shed light to phenomena that cannot be directly observed, such as in-cylinder processes in multi-cylinder engines. In order to successfully simulate the processes that take place inside the engine, several models are needed to handle every physical or chemical process, such as spray injection, droplet breakup and collisions, evaporation, ignition, combustion and emissions formation. A very powerful tool for these simulations is the numerical code KIVA-3V that has been developed at the Los Alamos National Laboratory.

The original KIVA program was publicly released in 1985 and was replaced by the improved version KIVA-II in 1989 [Amsden et al., 1989]. These earlier versions were performing quite well with confined in-cylinder flows and a variety of open combustion systems, but were rather inefficient when applied to complex geometries, such as long transfer ports or diesel pre-chambers. KIVA-3, released in 1993 [Amsden, 1993], has been improved by using block-structured meshes, as well as by reducing the computational time, by handling the data storage and boundary conditions in a more sophisticated and efficient way. KIVA-3V, made publicly available in 1997 [Amsden, 1997], retains all the features of previous versions, while offering the possibility to model intake and exhaust valves, making use of a moving mesh.

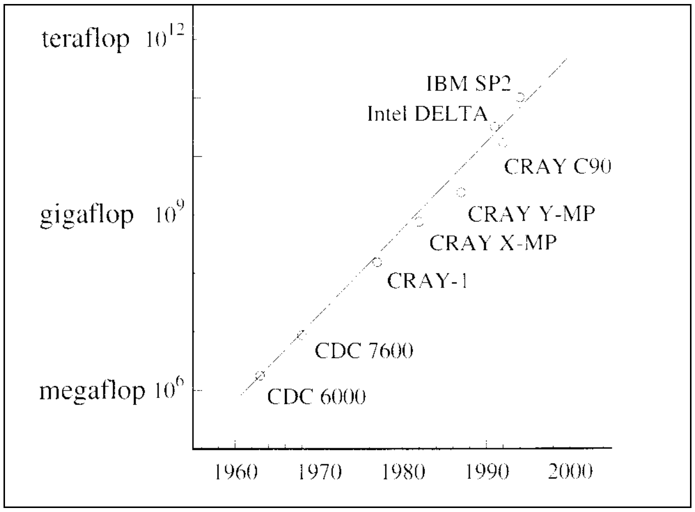

Figure 2: The speed of the fastest supercomputers against the year of their introduction [Pope, 2001]

Fuel sprays are typically represented using Lagrangian models for tracking the liquid droplets, as opposed to Eulerian models that can be more accurate but are still very time consuming and computationally intensive. The necessity of using a Lagrangian model can be illustrated by considering that droplets can have a diameter as small as 5 μm. In order to capture drop deformation and breakup, the computational cell size should be no larger than 1 μm. For a small diesel engine with cylinder displacement of 400 cm^3, the number of computational cells required would be in the order of $4 \cdot 10^{16}$. If we assume for simplicity that only 10^{13} cells are required (by using a coarse mesh in regions where drops are not likely to be found), this mesh is still 10^8 times larger than a typical mesh used nowadays. Assuming that computational power increases roughly 10 times every 5 years as shown in Figure 2 [Pope, 2001], the required computational speed to fully resolve a fuel spray with an Eulerian technique will be achieved in approximately 40 years from now. Alternatively, new Eulerian approaches can be used, based on the two-fluid model, which can predict spray evolution quite efficiently.

1.4 Modeling Fuel Sprays

Currently, the atomization process of fuel sprays is commonly modeled using a wave growth or aerodynamic theory that predicts spray parameters such as the spray angle and the drop diameter. The Taylor Analogy Breakup (TAB) model of O'Rourke and Amsden [1987], the surface wave instability model, proposed by Reitz [1987] and Reitz and Diwakar [1987], and the Kelvin-Helmholtz/Rayleigh-Taylor (KHRT) Instability model of Patterson and Reitz [1998], are widely used atomization models. These models are applicable in a short range of atomization conditions and cannot be used for modeling both gasoline and diesel sprays. Instead, the user selects the most appropriate model for each application, typically the TAB model for gasoline sprays and a WAVE-based model for diesel sprays.

A novel methodology to optimize the performance of fuel spray models has been developed by Grover [2005]. This methodology is based on a model framework that rigorously matches breakup time, drop size, and drag coefficients over a wide range of breakup regimes. The approach followed by Grover for the classification in secondary atomization regimes is also based on the Weber number of the droplets after primary atomization, as in the current work. The bag breakup regime is modeled based on the TAB approach, while the multimode, shear, and catastrophic breakup regimes are represented with models based on wave instabilities. These models are calibrated through an optimization process in order to provide accurate predictions for the breakup time and resulting droplet sizes.

In the current work, a new model based on physical concepts and experimental observations is developed, as opposed to optimizing existing atomization models for each breakup regime. This approach offers the flexibility of adding new physical process that are not represented from current models. In addition, Grover's work is focused on gasoline sprays, where injection and cylinder pressures are relatively low, compared to conditions in diesel engines, and the model validation is performed only for those sprays. In contrast, the new model developed here consists of submodels that can handle a wide range of conditions and has been validated against experimental data ranging from gasoline sprays to high injection pressures encountered in diesel applications.

1.5 Problem Statement – Overview of this Work

The objective of this work is to develop a spray atomization model based on physical concepts suitable for modeling typical fuel sprays used in internal combustion engines. The model should consist of three main parts: primary atomization, drop deformation and aerodynamic drag, and secondary atomization. The main challenge results from the fact that a wide range of conditions (e.g. injection pressures 5-210 MPa, ambient pressures 0.1-6.0 MPa and ambient temperatures 350-900 K) has to be considered, representing various applications, such as direct-injected gasoline engines with early or late injection timings or diesel engines with relatively early or late injection timings. This wide range of conditions implies that the physics controlling each process can vary considerably in each case and need to be modeled accordingly.

In order to model the primary atomization so as to provide initial conditions for the secondary atomization, simplified models are being used. Since the modeling is based on a Lagrangian approach different primary atomization models are necessary for different types of injectors. The drop deformation, aerodynamic drag and secondary atomization modeling are based on physical mechanisms and are common for all droplets, independently of the primary breakup mechanism that was used to create them. This approach has the advantage that a generic model can be developed for use in different applications. Only the primary breakup model will have to change when a new injector is introduced.

A description of the physical mechanisms governing primary and secondary atomization for typical gasoline and diesel sprays is given in Chapter 2. Currently used computational models are evaluated in Chapter 3 by analyzing their assumptions and exploring their limitations under various conditions. The proposed model is presented in Chapter 4, and includes primary atomization modeling, drop deformation and aerodynamic drag and secondary atomization. The drop deformation, aerodynamic drag and secondary atomization mechanisms are generic and do not depend on the type of injector, but only on physical properties of the system. The model validation is performed in Chapter 5, where model predictions are compared with experimental measurements for a wide range of sprays under various conditions. Furthermore, the behavior of the model in realistic engine geometries is demonstrated. Finally, in Chapter 6 the conclusions and recommendations for future work are presented.

CHAPTER 2

PHYSICAL MECHANISMS OF PRIMARY AND SECONDARY ATOMIZATION

The physical mechanisms governing fuel spray formation and atomization are reviewed in this chapter, focusing on sprays used in typical gasoline and diesel engine applications. Four aspects of the spray structure and properties are discussed, notably (i) the internal flow in the nozzle, (ii) the primary atomization properties, depending on the injector and nozzle characteristics, (iii) the spray structure in the dense area close to the nozzle, and (iv) the secondary atomization mechanisms.

2.1 Internal Flow in the Nozzle and Cavitation Phenomena

The flow characteristics inside the injector nozzle in conjunction with the nozzle geometry strongly affect the liquid structure emerging from the nozzle. Depending on the internal geometry of the nozzle, the turbulence levels can be significantly increased, hence contributing in faster primary atomization. Experimental and numerical studies have been performed both for typical gasoline and diesel injector nozzles to shed light to phenomena leading to primary atomization [Arcoumanis, Gavaises, 1998], [Soteriou et al., 1995], [Schmidt, Corradini, 2001], [v. Berg et al., 2005], [Kubo et al., 2001]. The discussion in this section is focused on phenomena occurring in typical diesel injector nozzles, including cavitation, which is the combined result of high injection pressures and sharp angles inside the nozzle.

One of the main difficulties with studying the internal flow in a nozzle stems from the fact that the geometrical dimensions are very small and gaining optical access to the orifice is not a trivial task. Scaled-up nozzles have been built to visualize the fluid flow; however the nature of the problem does not allow appropriate scaling of all the important variables. Changing the size of the device will alter not only the Reynolds number but also the time scale of the problem. In addition, the cavitation nuclei will be of different sizes compared to the model device. Changing the speed in order to maintain the Reynolds number can complicate the problem by further altering the time scale, as well as the cavitation number. The cavitation number definition varies among researchers but is indicative of the injection pressure required for the inception of cavitation. A final issue adding to the complexity of the problem is how to anticipate cavitation phenomena in one liquid based on data obtained in another. Most experiments are performed with water as the test liquid, while in engine conditions diesel fuel is utilized. The difference in fuel properties, particularly in surface tension, can significantly affect the interpretation of the experimental results. It should be noted here that once cavitation has become established, the phenomena that occur are much less sensitive to special factors [Brennen, 1995].

Despite the difficulties mentioned in the previous paragraph, considerable efforts have been done to understand and model cavitation and its effects on turbulence and primary atomization. It has been found that liquids are subject to cavitation in regions of critically low pressure. The cavitating region may consist either of a mass of small bubbles or foam, or of small bubbles in addition to a larger pocket or pockets of vapor and undissolved gas. There are two basic mechanisms that can lead to cavitation in diesel injector nozzles: dynamically- and geometry-induced cavitation [Soteriou et al., 1995]. Dynamically-induced cavitation occurs only in transient flow and is caused by pressure wave activity or needle movement. Geometry-induced cavitation can occur both in steady state and transient flow. It is initiated downstream of sudden changes in the flow path geometry, in regions of high velocity recirculating flow.

Soteriou et al. [1995] concluded that cavitation in the nozzle hole causes atomization of the jet immediately on exit and is beneficial for increasing the atomization rate. This cavitation process produces a homogeneous foam, rather than large voids. The cavitation occurs on one side of the orifice, therefore leading to asymmetric spray structures. Similar results have been obtained with multidimensional simulations of the cavitating internal flow and the resulting spray structure. Computational approaches typically utilize the two-fluid model within the injector for the cavitating flow. A primary atomization model is applied at the nozzle orifice where it is coupled with the standard discrete droplet model. Alternatively, the Eulerian multi-fluid model is applied for both the nozzle and spray regions [v. Berg et al., 2005].

In this work, the issues related to the internal flow in the nozzle are not addressed, as they are geometry dependent and findings cannot be readily generalized. Instead, it is assumed that the entire cross-sectional area is utilized and the injection velocity profile is specified. Given the boundary conditions, our effort is focused in modeling only the primary and secondary atomization.

2.2 Overview of Primary Atomization Mechanisms

The primary breakup mechanisms vary considerably with nozzle design, injection pressure, and engine operation. This is illustrated in Figure 3, where the primary breakup for a diesel spray (liquid core) and for a gasoline swirl spray (liquid sheet) is schematically shown. There are substantial differences on the size, shape and durations of these mechanisms. Their common feature is that they connect nozzle design properties and spray properties and they also define initial conditions for the dense sprays. The two cases of Figure 3 will be discussed in this section, due to their importance for typical fuel sprays in internal combustion engines.

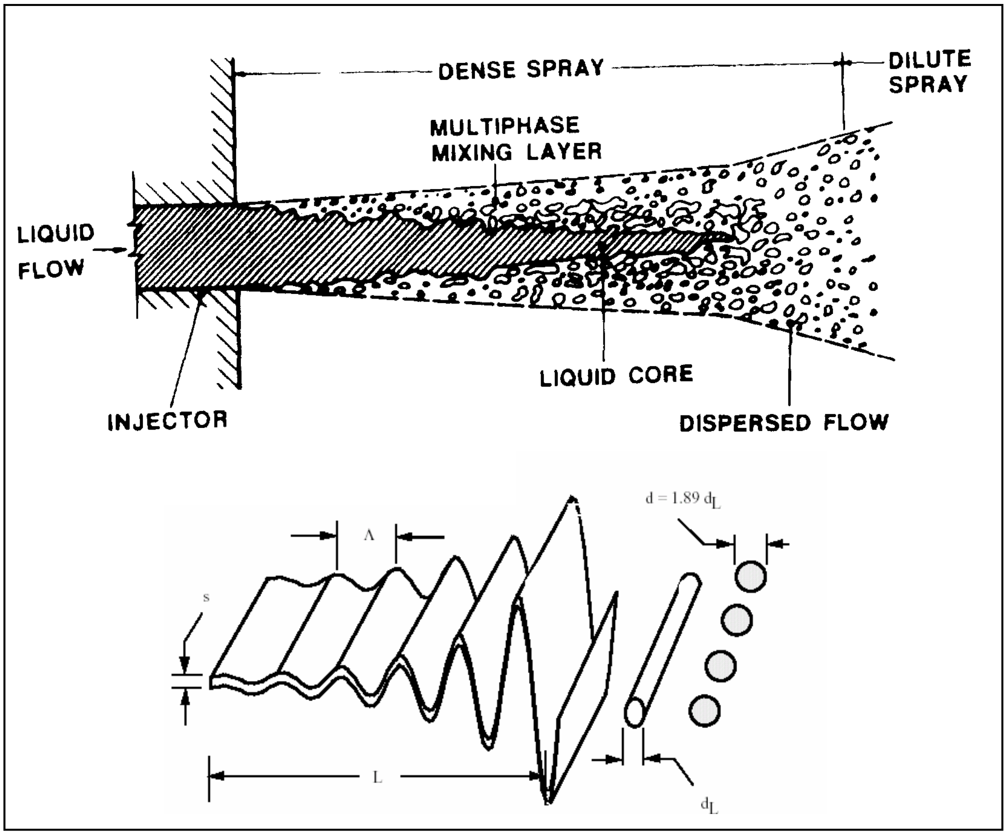

Figure 3: Primary atomization of (a) liquid jet, (b) liquid sheet.

Some phenomena that are common for the process of atomization include the development of waves on a liquid surface, the increase in their amplitude and the loss of stability. Waves form on the surfaces of the jets and sheets of liquid as well as on the surface of drops moving in the gaseous medium and disintegration is caused by these rapidly growing waves. The theoretical work that has been reported is based mainly on investigating instability by means of the method of small disturbances. According to this method, arbitrary small vibrations are superposed with the main fluid motion. These vibrations have various frequencies and are of internal and external origin. The internal causes stem from disturbances in the atomizer itself, such as swirling, liquid expansion due to pressure drop, disturbances on the edges of the inlet and outlet orifices and manufacturing imperfections. The external causes include the interaction with the surrounding media, that is the aerodynamic forces, which depend on the relative velocity, the density of the gas and the dimensions of the liquid leaving the nozzle [Bayvel and Orzechowski, 1993].

2.2.1 Stability and Disintegration of Liquid Jets

The properties of interest for liquid jets are the continuous length, which provides a measure of the growth rate of the disturbance, and the resulting drop size, which is a measure of the wave number of the most unstable disturbance. Also important is the manner in which the jet is disrupted. Four distinct breakup regimes in the disintegration of a liquid jet can be identified [Lefebvre, 1989], [Lin and Reitz, 1998].

(a) Drop formation without the influence of air (Rayleigh or varicose mechanism). Radially symmetric waves are formed by the interaction of primary disturbances in the liquid and surface tension forces. This regime is characterized by a linear relationship between the length of the jet prior to breakup and the jet velocity.

(b) Drop formation with air influence. As the jet velocity increases the aerodynamic forces of the surrounding air are no longer negligible and tent to accentuate the waves formed under the previous regime.

(c) Drop formation due to waves on the jet surface (“sinuous” jet). This regime is associated with increasing effectiveness of aerodynamic forces and reduced relative influence of the surface tension.

(d) Complete disintegration of the jet. The liquid is broken up at the nozzle in a chaotic and irregular manner.

The liquid core of a fuel spray, L_c, which is similar to the liquid length prior to drop formation of a single-phase jet, can be estimated as:

$$\frac{L_c}{d} = C_c \left(\frac{\rho_L}{\rho_G} \right)^{1/2} \tag{2.1}$$

where d is the injector diameter, ρ_L and ρ_G are the liquid and gas densities, respectively, and C_c an empirical constant with values in the range 7-16. Experimental data by Siebers [1998] show that equation (2.1) gives very good estimates for the liquid core length of diesel sprays, under a wide range of conditions. Particularly, the liquid core length depends linearly on the orifice diameter and the effect of the ambient pressure is very well described with the square root law. Only the effect of the ambient temperature is neglected in this equation but it can be taken into account if the empirical constant C_c is calibrated accordingly.

2.2.2 Stability and Disintegration of Liquid Sheets

Many atomizers form flat or conical liquid sheets instead of round jets. Conical sheets can be obtained if a liquid flowing in a pipe is deflected through an annular orifice, as in outwardly opening injectors, in which case the cone angle is controlled by the angle of deflection. A conical sheet can also be generated by pressure-swirl nozzles, where the liquid emerges from an orifice with strong angular momentum resulting from its passage through a number of tangential or helical slots. When a liquid sheet emerges from a nozzle, its subsequent development is influenced by its initial velocity and the physical properties of the fuel and the ambient gas.

The disintegration process for sheet disintegration has been described by Fraser and Eisenklam [1953], who define three modes of disintegration, referred to as rim, wave and perforated sheet disintegration. The *rim disintegration* takes place at the edge of the film, where, due to surface tension forces, rims are formed and disintegrate, similar to a jet, leading to relatively large droplets. *Perforated sheet disintegration* is characterized by the appearance of holes in the center region of the sheet, which grow bigger as the film extends radially. Also, the ligaments between the holes collapse into droplets. The *wavy film disintegration* process is generated by growing waves of the liquid film, initialized by the action on the surrounding air on the film surface. Reaching a certain maximum amplitude of the disturbances, the film breaks up into ligaments and finally to droplets.

Squire [1953], who investigated the instability of a moving inviscid liquid film, assumed the existence of a wavelength with maximum growth rate for Weber numbers much smaller than unity. This wavelength is responsible for the disintegration of the sheet into ligaments and Dombrowski and Johns [1963] extended this approach to viscous diminishing sheets. They suggest that the mean droplet sizes are roughly proportional to the square root of the film thickness.

A number of computational models appropriate for conical sheets utilized in gasoline direct-injected sprays have been developed in the last decade, including works from Dorfner et al. [1995], Han et al. [1997], Schmidt et al. [1999] and Senecal et al. [1999]. The model proposed by Schmidt and Senecal has been found to be less dependent on empirical parameters than the other two and is suitable for simulations of gasoline sprays emerging from swirl injectors [Chryssakis, 2002, Chryssakis et al. 2002, Chryssakis et al., 2003].

2.3 Dense Spray Structure and Drop Deformation

The dense spray structure of round pressure-atomized sprays in a still gas will be described here to illustrate the environment of dense sprays. There are two main flow regions of interest within dense sprays; namely the liquid core, described above and the dispersed flow region beyond the surface of the liquid core. The dispersed flow region is comprised of a multiphase mixing layer in the region where the liquid core is present and develops into a dilute round spray. Primary breakup occurs due to ligaments forming on the surface of the liquid core; therefore primary breakup rate tends to control the length of the liquid core.

The outcome of primary breakup frequently is irregular drops or ligaments while most liquid elements resulting from primary breakup are unstable to secondary breakup. Further insight can be gained from the structure properties plotted in Figure 4a,b. In Figure 2a [Faeth et al., 1995] results for round pressure-atomized water sprays at still air at various pressures are shown. The results, including the ellipticity of the drops, the Sauter Mean Diameter (SMD) of the spray and drop velocities for various drop diameters, are plotted as a function of radial distance from the nozzle exit. The region near the liquid surface consists of large, irregular, ligament-like elements (large ellipticity and SMD), whereas the dilute spray region near the edge of the flow involves smaller round drops.

Very similar observations have been made for the primary atomization of the pre-swirl spray, emerging from a swirl injector used in gasoline engines. The measurements performed at the University of Hiroshima by Lee and Nishida [2003] with an Image Processing technique, are summarized in Figure 4b and are presented as a function of time. Comparison of Figure 4 reveals that even though the sprays under investigation are the outcome of substantially different atomizer designs, both the average SMD and the ellipticity of the drops is of the same order of magnitude and has the same trends towards smaller, spherical drops, subject to secondary breakup.

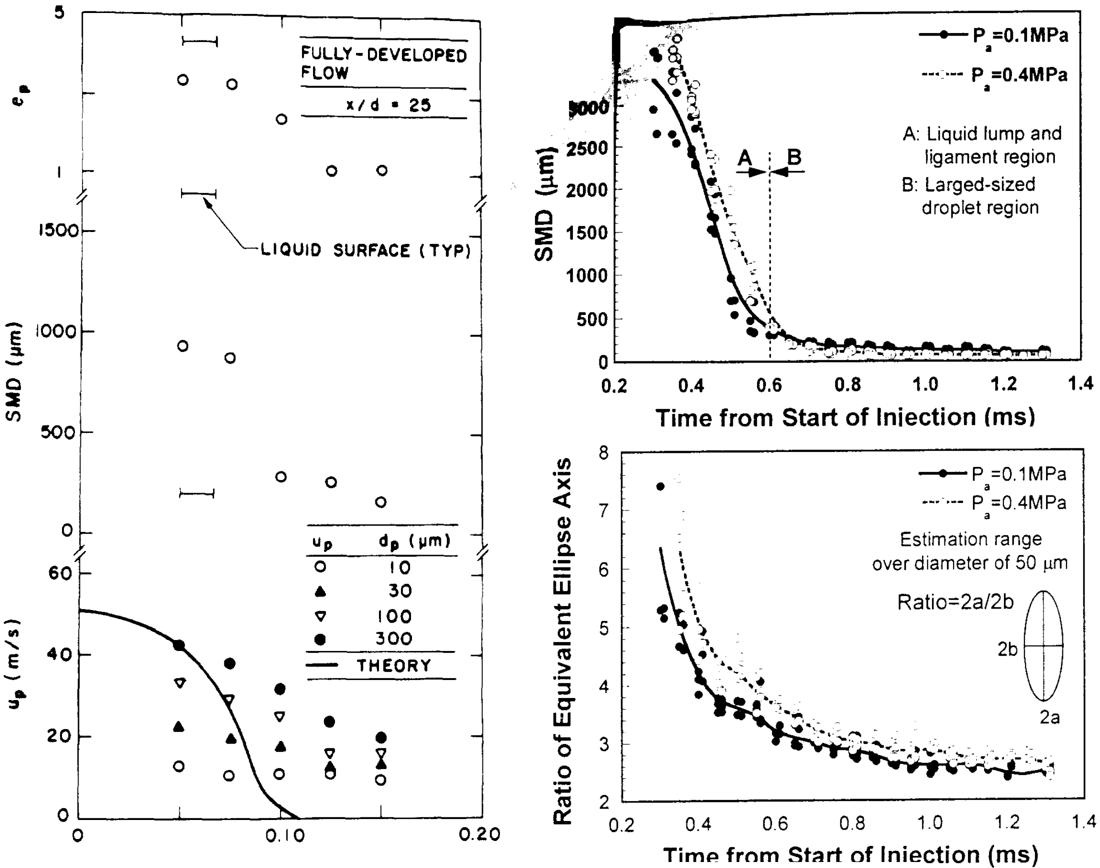

(a) Faeth et al. [1995]

(b) Lee, Nishida [2003]

Figure 4a,b: Primary atomization outcome, (a) Faeth et al. [1995], (b) Lee, Nishida [2003].

A complication that may occur when modeling the dense spray regions results from the fact that the secondary breakup mechanisms that will be described in the next section have been established through experiments on isolated drops. However, when droplets are no longer isolated, experimental evidence suggests that the value of the critical Weber numbers may not accurately represent breakup transitions [Lengsfeld et al., 2002]. If the droplet spacing between droplets is 3 to 5 diameters errors can result from applying the theory for isolated droplets. In particular, the effects of local vapor concentration, drag reduction by a lead droplet and surface tension dependence on decreasing liquid/gas density ratios should be studied. In this section the analysis will focus only on drop deformation and aerodynamic drag for isolated drops.

Two different aspects of the drop deformation process are of interest for sprays. First, drop behavior for $We<12$ will be described. These drops are not subject to secondary breakup and do not disintegrate into smaller droplets but they deform and obtain the shape of oblate spheroids, which significantly affects their aerodynamic drag properties. Subsequently, drop deformation for $We>12$ will be portrayed. These drops deform for a relatively long period of time before the disintegration process starts. As in the previous case, the drops become oblate spheroids and their aerodynamic drag coefficients approach the ones for a flat disk.

2.3.1 Drop Deformation for $We<12$

When the initial Weber number of a drop is $We<12$ the drop deforms and reaches a final condition or follows an oscillation mechanism, with drop shapes oscillating between two extreme conditions (oblate and prolate spheroids). Helenbrook and Edwards [2002] performed a numerical analysis of drop deformation for $We<10$ and $Re<200$ in order to predict the final stage of deformation of an initially spherical liquid drop in an ambient gas medium. Furthermore, they investigated the effect of deformation on the aerodynamic drag coefficient of the drop. Liquid-to-gas ratios between 5 and 500, viscosity ratios between 5 and 15, Weber numbers between 0.1 and 10 and Ohnesorge numbers between 10^{-4} and 10 were analyzed. Three distinct drop shapes were observed, as shown in Figure 5, namely prolate, oblate and dimpled spheroids and the conditions that cause the appearance of these shapes were determined.

Oblate drops are what is normally expected based on the knowledge of flow over a sphere. There is a high-pressure zone at the leading and trailing edges and low pressure zones near the equator. The peak pressure is at the stagnation point, at the leading edge, and the minimum on the equator. This pressure distribution tends to collapse the drop into an oblate shape. These shapes will be examined in more detail, as they are most relevant for practical spray applications.

Prolate shapes are opposite to the reasoning described in the previous paragraph. These shapes are caused by the internal liquid circulation of the droplet rather than the external gas flow. However, the internal circulation is strongly inhibited by contamination on the liquid/gas interface. According to Clift et al. [1978], in most practical systems surfactants cannot be eliminated, thus eliminating the internal circulation and preventing the drops from reaching prolate shapes.

Dimpled shapes are defined by a concave region at the rear of the drop. They appear at low Reynolds and relatively high Ohnesorge numbers (*Oh*>0.1). Therefore, dimpled shapes are more likely to be observed for falling drops than for injected ones.

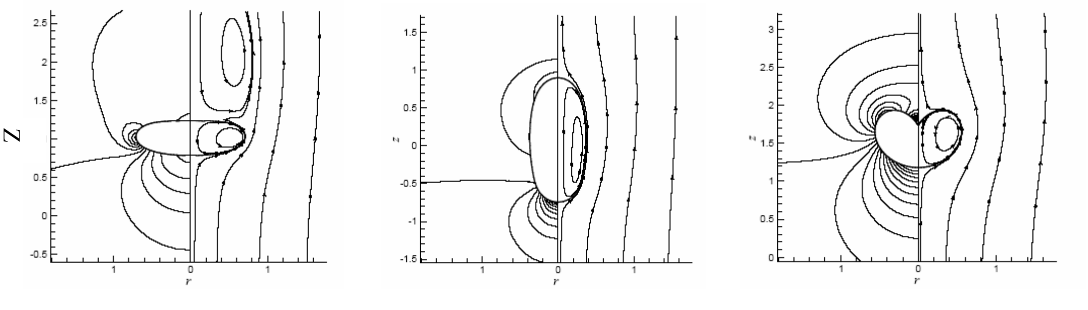

Figure 5: Oblate-, Prolate- and Dimpled-shaped drops [Helenbrook and Edwards, 2002]

The deformation of oblate spheroids is described by a single parameter, the aspect ratio, *E*. The aspect ratio is defined as the ratio of the centerline height to the equatorial diameter of the drop. The final drop deformation, observed when the drop reaches a steady-state condition, is given by:

$$\boldsymbol{E} = \frac{\boldsymbol{d}_{\min}}{\boldsymbol{d}_{\max}} = 1 - 0.11\boldsymbol{We}^{0.82} \tag{2.2}$$

Also, for oblate spheroids,

$$\boldsymbol{d}_{\min} = \frac{\boldsymbol{d}_{\boldsymbol{o}}^{3}}{\boldsymbol{d}_{\max}^{2}}, \tag{2.3}$$

where d_{max}=d_c, which is equal to the cross-sectional diameter, perpendicular to the gas flow. Therefore,

$$\frac{\boldsymbol{d}_{\boldsymbol{c}\max}}{\boldsymbol{d}_{\boldsymbol{o}}} = \left(1 - 0.11\boldsymbol{We}^{0.82}\right)^{-1/3}. \tag{2.4}$$

In Figure 6, the maximum distortion as a function of Weber number is plotted for *We*<12. The maximum value is 1.86, very close to the prediction of Hsiang and Faeth [1992] of 1.7, based on averaging of experimental observations.

According to Aalburg et al. [2003], the time required for a drop to reach its maximum deformation is given by:

$$\frac{\boldsymbol{t}_{\max}}{\boldsymbol{t}^{*}} = 1.53\left(\frac{\boldsymbol{d}_{\boldsymbol{c}\max}}{\boldsymbol{d}_{\boldsymbol{o}}} - 1\right)^{0.52}, \text{ for } Re>50. \tag{2.5}$$

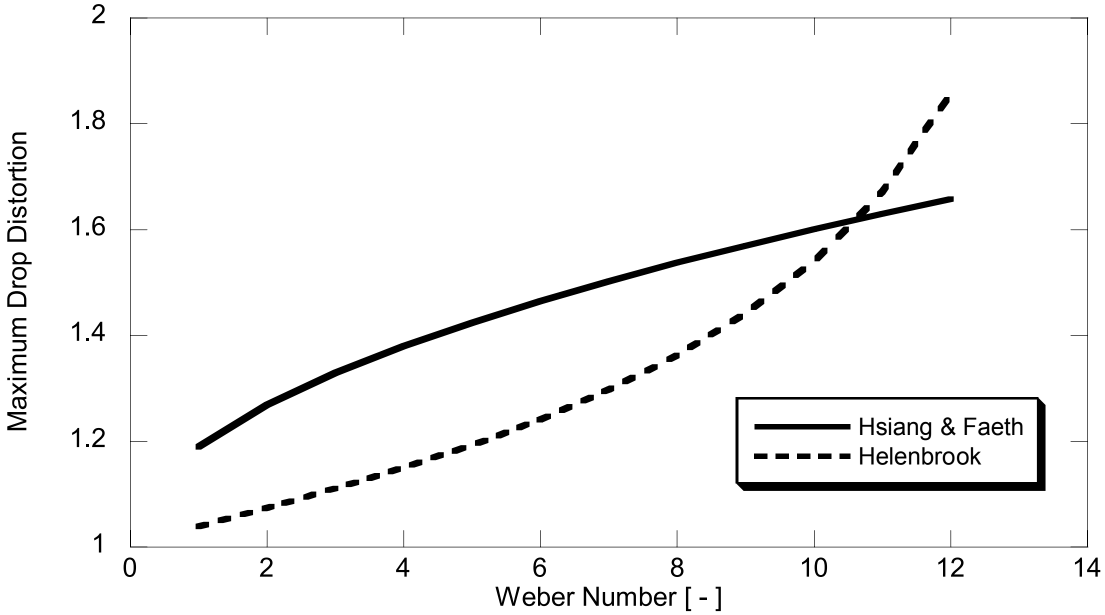

Figure 6: Maximum Drop Distortion as a function of Weber number.

Assuming that the deformation grows linearly with time, we have:

$$\frac{d_c}{d_o} = 1 + \left(\frac{d_{c\,\max}}{d_o} - 1 \right) \frac{t}{t_{\max}} . \qquad (2.6)$$

2.3.2 Drop Deformation for *We*>12

When the initial Weber number of a drop is *We*>12, the drop can undergo secondary breakup, provided that the Eotvös number criterion is also satisfied (*Eo*>16), as explained in the next section. In the time prior to breakup the drop deforms and reaches an ellipsoidal shape, similar to the one described above. Hsiang and Faeth [1992] made experiments over a wide range of conditions and concluded that the maximum drop distortion can be given as

$$\frac{d_{c\,\max}}{d_o} = 1 + 0.19 We^{1/2}\,,\ Oh<0.1,\ We<100 \tag{2.7}$$

and

$$\frac{d_{c\,\max}}{d_o} \approx 2\,,\ Oh<0.1,\ We>100. \tag{2.8}$$

Assuming linear increase of the drop deformation with time, as for the previous case, yields:

$$\frac{d_c}{d_o} = 1 + \left(\frac{d_{c\,\max}}{d_o} - 1 \right) \frac{t}{t_{\max}}\,. \tag{2.9}$$

2.3.3 Aerodynamic Drag Coefficients

The aerodynamic drag forces on a drop can be calculated if the aerodynamic drag coefficient and the cross-sectional area of the drop (normal to the flow) are known. The cross-sectional area can be calculated based on the maximum drop diameter, d_c, since we assume that deformed drops are oblate spheroids. The aerodynamic drag coefficient can be estimated based on the knowledge for drag coefficients for solid bodies of similar shape.

According to Clift et al. [1978], when a fluid sphere exhibits little internal circulation, either because of high viscosity ratio or because of surface contaminants, the external flow is indistinguishable from that around a solid sphere at the same Reynolds number. Surface contaminants tend to eliminate internal circulation and they exist in most systems of practical importance. Even if bubbles and drops are relatively free of surfactants upon injection, internal circulation decays rapidly as contaminant molecules accumulate at the liquid-gas interface. Considering the fact that the liquid-to-gas viscosity ratio in sprays is high, we can assume that internal circulation is not a significant parameter and rigid-body aerodynamic drag correlations can be used.

The correlation adopted here (from Clift et al. [1978]) for the drag coefficient of a liquid sphere (E=1), is:

$$\boldsymbol{C_D} = \frac{24}{\mathrm{Re}}\left[1+0.15\,\mathrm{Re}^{0.687}\right]+\frac{0.42}{1+4.25\,\mathrm{Re}^{-1.16}\cdot 10^{4}}\,,\ Re<3\times 10^{5}. \tag{2.10}$$

For liquid disks, one can use [Clift et al., 1978]

$$\boldsymbol{C_D} = \frac{64}{\boldsymbol{\pi}\,\mathrm{Re}}\left(1+0.138\,\mathrm{Re}^{0.792}\right),\ 1.5<Re<133 \tag{2.11}$$

$$C_D=1.17,\ Re>133 \tag{2.12}$$

For oblate spheroids with aspect ratio E=0.5, Clift et al. suggest:

$$\boldsymbol{C_D} = 108.42\,\mathrm{Re}^{\left(-1.66+.3958\log \mathrm{Re}-0.03\log^{2}\mathrm{Re}\right)},\ 40<Re<10^{4}. \tag{2.13}$$

The three equations describing drag for the sphere, the disk and the spheroid are plotted in Figure 7. For intermediate values of the aspect ratio, E, linear interpolation will be used in the model. The Reynolds number in the correlations for the disk and the spheroid is based on the cross-sectional diameter, d_c, which is calculated according to the equations described in the previous sections.

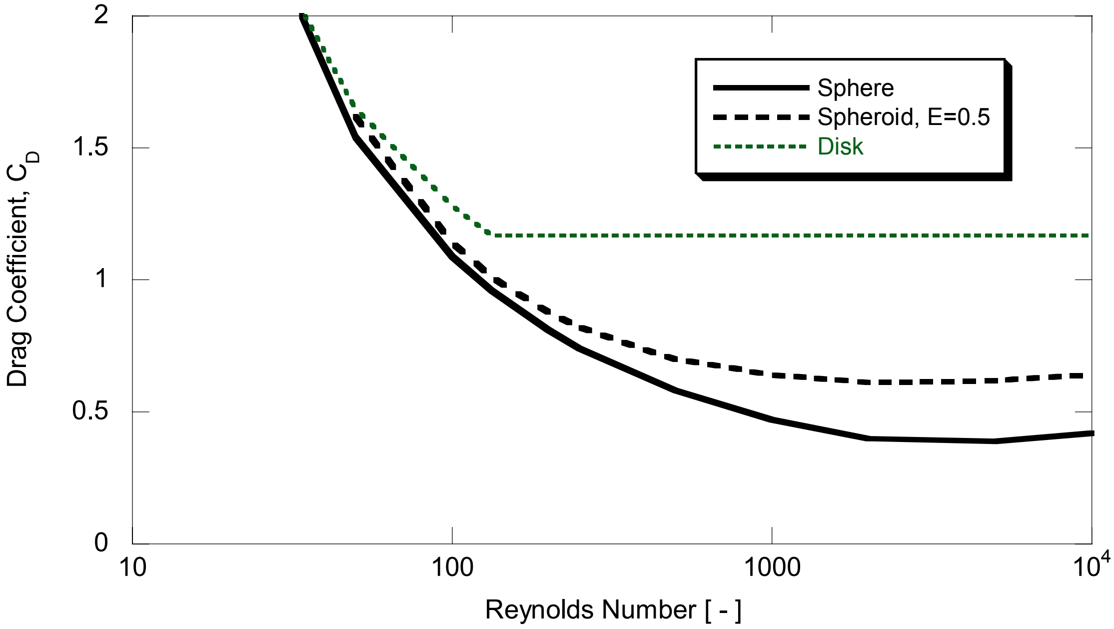

Figure 7: Aerodynamic Drag Coefficients of Sphere, Spheroid and Disk.

2.4 Secondary Atomization Mechanisms

The secondary breakup of drops is a multiphase flow process that is common for all sprays, independently of their primary atomization mechanism. Numerous studies of dilute sprays, as well as of isolated droplets have been performed in order to increase our understanding of this spray region. Early work by Hinze [1955], Ranger and Nicholls [1969], Krzeczkowski [1980] and Gelfand [1996] shows good agreement with detailed measurements obtained by Faeth and coworkers more recently.

Existing experimental observations of secondary breakup generally involve liquid/gas density ratios greater than 50 and drop Reynolds numbers greater than 50. At these conditions, Hinze [1955] shows that breakup regime transitions are functions of the initial Weber and Ohnesorge number of a drop, where:

$$We = \frac{\rho_G d_o u_o^2}{\sigma} \text{ and } Oh = \frac{\mu_L}{\left(\rho_L d_o \sigma\right)^{1/2}}, \qquad (2.14)$$

which are the ratio of aerodynamic and liquid viscous forces to surface tension forces respectively. In Figure 8 a plot compiled by Hsiang and Faeth [1995] is shown, including results from other researchers as well, demonstrating very good agreement with Hsiang's measurements. It is very interesting to note that for small Ohnesorge numbers (Oh<0.1), the transition between regimes is a function of the Weber number only, whereas Oh becomes important for Oh>0.1. This can be interpreted by considering that for small Oh, the liquid viscous forces are small and aerodynamic drag forces can only be balanced by surface tension effects. However, as liquid viscosity increases, liquid viscous forces stabilize gas dynamic forces.

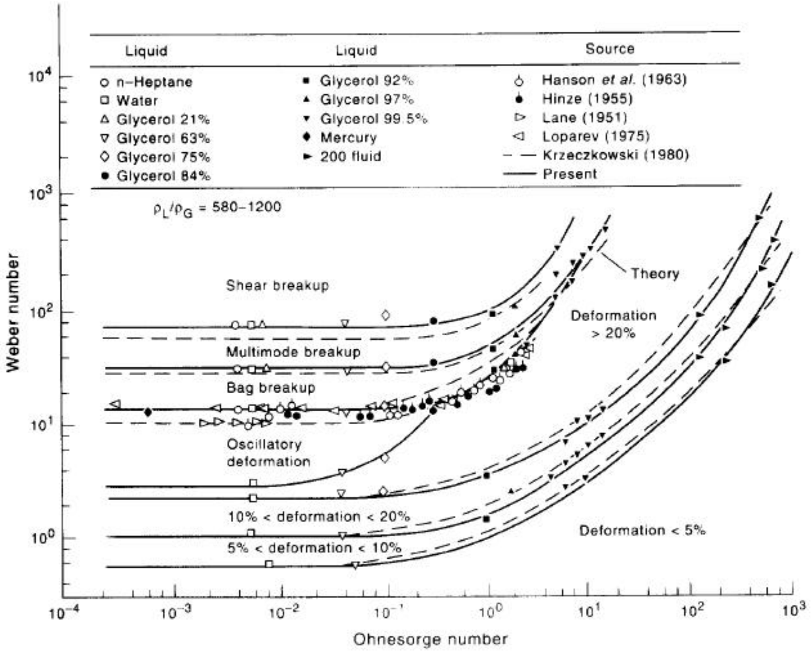

Figure 8: Drop deformation and breakup mechanism map [Hsiang and Faeth, 1995]

In summary, Figure 8 illustrates four deformation regimes (5%, 10%, 20% and oscillatory deformation), the bag breakup regime for 12<We<35, the multimode breakup for 35<We<80, the shear breakup for 80<We<850 and the catastrophic breakup regime for We>850. These limits increase as the Oh number increases and there is an uncertainty for high Ohnesorge and Weber numbers since experiments cannot be easily performed under these conditions.

In Figure 9 these breakup mechanisms are illustrated. It is obvious that the physical mechanisms involved in each case present big differences. For example, in the bag breakup a large number of small fragments and a small number of large fragments are created. On the other hand, in the shear breakup regime a coherent residual drop exists during the entire breakup process, while a large number of small fragments are created through a "sheet stripping" mechanism. Therefore, each regime should be modeled according to its governing physical mechanisms in order for a model to take into account any given spray under different ambient conditions. In the followings, other aspects of secondary breakup will be discussed, such as drop deformation and aerodynamic drag, breakup time and breakup rates and resulting droplet sizes. These aspects are critical for a computational model and they have to be considered in order to achieve a satisfying prediction capability.

2.4.1 Breakup Times

A dimensionless time characteristic of drop breakup has been proposed by Ranger & Nicholls [1969] as:

$$t^* = \frac{d_o}{u_o}\left(\frac{\rho_L}{\rho_g}\right)^{1/2} . \tag{2.15}$$

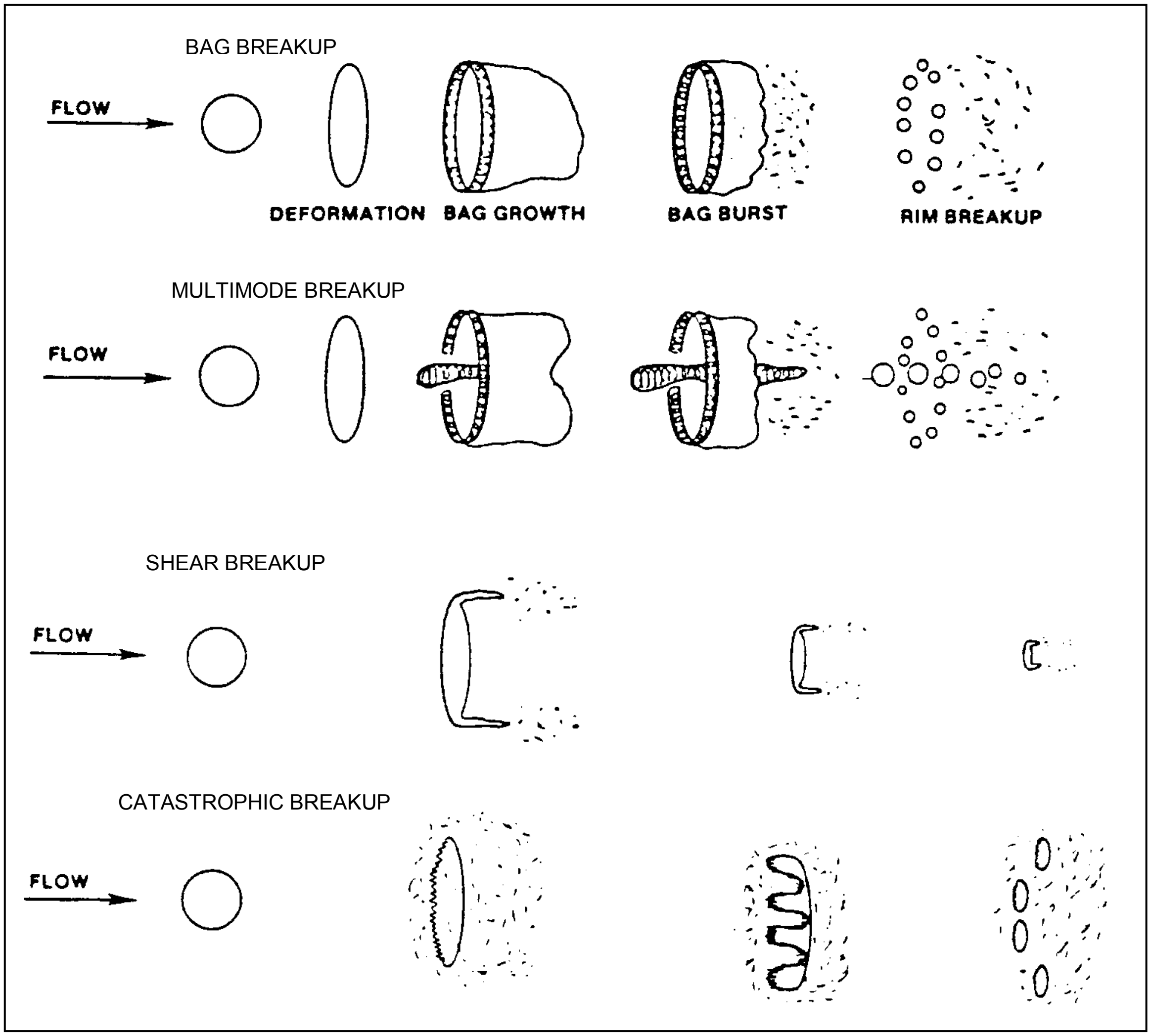

Figure 9: Bag, Multimode, Shear and Catastrophic breakup mechanisms (from Pilch and Erdman [1987]).

Two characteristic times are of interest: initiation and end of breakup [Pilch and Erdman, 1987]. The definition for initiation of breakup is somewhat arbitrary and depends on the breakup mechanism. Start of bag formation marks initiation of breakup for the bag and multimode breakup regimes. The first sign of sheet being drawn downstream from the drop marks the initiation of shear breakup and the first sign of mist generated around the drop surface signals the initiation of catastrophic breakup.

The dimensionless time characteristic required to initiate breakup decreases continuously with increasing Weber number. A simple empirical correlation is proposed by Pilch and Erdman [1987] that adequately describes the breakup initiation time for both low and high Ohnesorge numbers:

$$\frac{t}{t^*} = 1.9 \cdot (We - 12)^{-1/4}\left(1 + 2.2 Oh^{1.6}\right), \tag{2.16}$$

where t^* is obtained from equation (2.15).

End of breakup is defined as the time when the drop (if a coherent drop still exists) and all its fragments no longer undergo further breakup. Correlations for total breakup time are given by Pilch and Erdman [1987]:

$$t/t^* = 6(We-12)^{-1/4}, \qquad 12 < We < 18 \tag{2.17}$$

$$t/t^* = 2.45(We-12)^{1/4}, \qquad 18 < We < 45 \tag{2.18}$$

$$t/t^* = 14.1(We-12)^{-1/4}, \qquad 45 < We < 351 \tag{2.19}$$

$$t/t^* = 0.766(We-12)^{1/4}, \qquad 351 < We < 2670 \tag{2.20}$$

$$t/t^* = 5.5, \qquad 2670 < We \tag{2.21}$$

The end of breakup times given by equations (2.17-21) are valid for low viscosity drops, $Oh<0.1$. For highly viscous drops, Gelfand [1996] proposed a correlation based on a limited collection of data:

$$t/t^* = 4.5(1+1.2Oh^{1.64}), \qquad We < 228. \tag{2.22}$$

In Figure 10 the initiation and end of breakup time are plotted in dimensionless form as a function of the Weber number, for $Oh<0.1$.

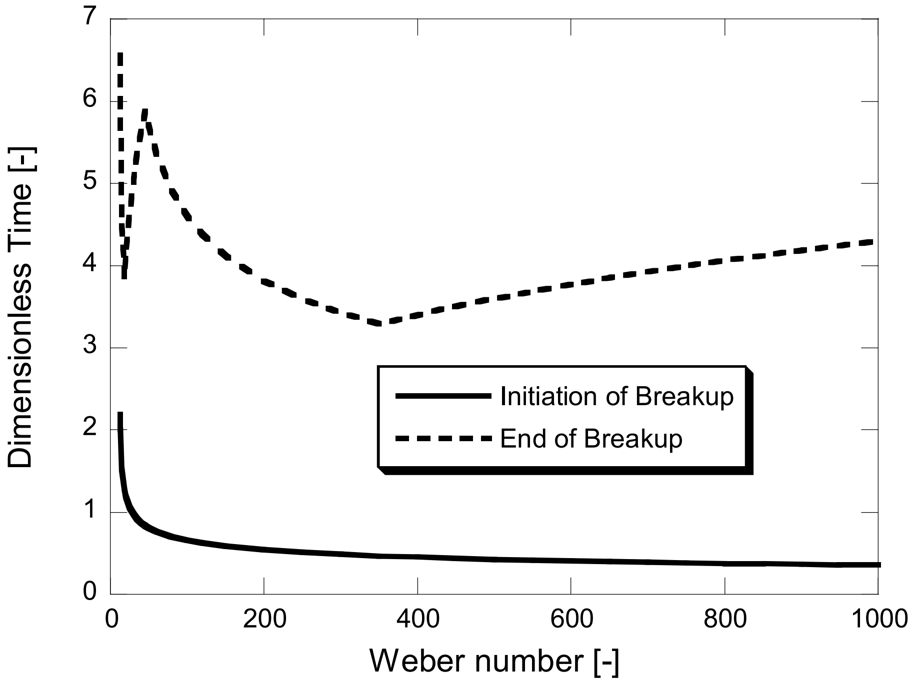

Figure 10: Initiation and end of breakup times for Oh<0.1.

After the end of breakup time has been reached secondary breakup finishes; however there are still droplets, especially parent drops remaining from shear breakup, with size and velocity sufficiently large to fall in the category of $We>12$. According to the previous discussion on breakup regimes these droplets should be subject to tertiary breakup according to the mechanism determined by the combination of their We and Oh numbers. However, it has been found by Hsiang and Faeth [1993] and Faeth [2002] that tertiary breakup does not occur. The criterion for the completion of breakup is associated to conditions indicating that the drop has been adjusted to the ambient flow over the secondary breakup period. Deformations and breakup transitions for gradual disturbances are correlated in terms of the *Eötvös* number, *Eo*, defined as:

$$Eo = \frac{a\rho_L d^2}{\sigma} \tag{2.23}$$

where a is the local acceleration of the drop. It was found that drop stripping for shear breakup ended for $Eo=16$ for the parent drop.

2.4.2 Resulting Drop Sizes

It has been found that the size distributions of drops produced by secondary breakup at each instant of time can be expressed using the universal root normal distribution function, *MMD/SMD,* where *MMD* and *SMD* denote the mass median and the Sauter mean diameters of the drop size distribution, respectively [Lefebvre, 1989]. The SMD, or D_{32}, is the diameter of the drop whose ratio of volume to surface area is the same as that of the entire spray, whereas the MMD, or $D_{0.5}$, is a drop diameter such that 50% of the total liquid volume is in drops of smaller diameter. The locations of various representative diameters on a drop size frequency curve can be found assuming a Rosin-Rammler distribution. This is convenient because all the representative diameters in the spray are uniquely related to each other via the distribution parameter q. We have

$$\frac{MMD}{SMD} = \left(0.693\right)^{1/q}\Gamma\left(1-\frac{1}{q}\right), \qquad (2.24)$$

where Γ denotes the gamma function. Hence, if the *MMD/SMD* ratio is known, the droplet size distribution can be calculated from the Rosin-Rammler distribution.

For the bag breakup regime, Chou and Faeth [1998] found that $MMD/SMD=1.2$, similar to their findings for the shear breakup regime. However, when only the bag (and not the rim) is considered, MMD/SMD=1.04, a result implying that the size distribution is nearly monodisperse, because the bag membrane appears to have a relatively uniform thickness.

In the multimode breakup regime, the drop sizes of ring, plume and core drops have been separately considered, while the drops of the bag have been found to have the same sizes as the ones in the bag breakup mechanism [Dai and Faeth, 2001]. In Figure 11 the sizes of the ring, plume and core drops are given as a function of the Weber number.

In the shear breakup regime the universal root size distribution can again be used with value *MMD/SMD*=1.2. However, in this case the temporal variation of the drop sizes is very interesting to study. An important parameter is the dimensionless number, where v_L is the kinematic viscosity of the liquid phase. For values of this number less than 0.002, the SMD/d_o ratio varies from 0.03 to 0.09, while for larger values, SMD/d_o remains constant at 0.09 [Chou et al., 1997].

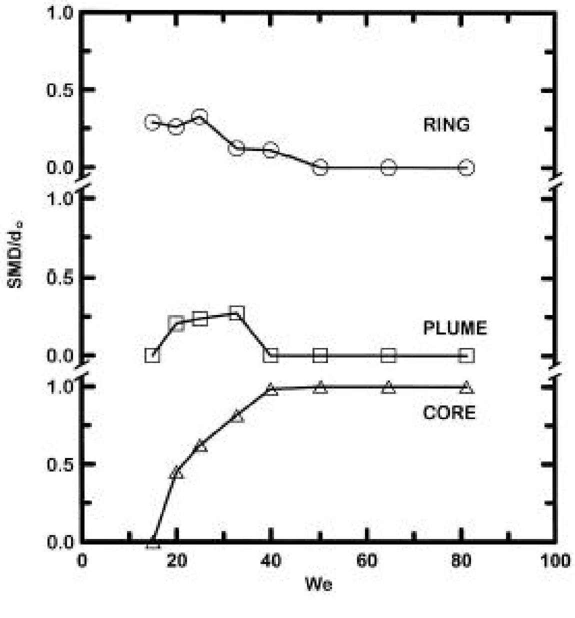

Figure 11: Drop sizes for plume, core and ring, as a function of Weber number [Dai and Faeth, 2001]

From the above discussion becomes obvious that the MMD/SMD ratio remains constant for bag, multimode and shear breakup mechanisms, but a closer look at each regime shows that differences exist and they have to be considered in a computational model.

CHAPTER 3

EVALUATION OF CURRENT FUEL SPRAY MODELING APPROACHES

In an effort to characterize fuel sprays a number of spray breakup models have been developed over the last decades. The primary atomization in swirl sprays for gasoline engines is typically modeled using liquid sheet instability theories, while the jet breakup is modeled considering growing wave instabilities on the jet surface or a combination of turbulence perturbations and instability theories. The most popular approaches for the secondary atomization are the Taylor Analogy Breakup (TAB) model, developed by O'Rourke and Amsden [1987] and the WAVE model, developed by Reitz and Diwakar [1987] and further refined by Reitz [1987]. Variations and improvements of these models have also been proposed by other researchers. In this chapter a brief overview of the most representative models used nowadays is given along with an evaluation of their main features.

3.1 Modeling Fuel Sprays in KIVA-3V

The KIVA-3V code has the ability to calculate complex in-cylinder flows, including evaporating fuel sprays interacting with flowing multicomponent gases undergoing mixing, ignition, chemical reactions and heat transfer with arbitrarily shaped piston geometries. A Lagrangian approach is used for modeling fuel sprays due to the very large number of droplets and their very small dimensions compared with the engine size. If an Eulerian approach was selected, the size of the computational cells would be in the order of a few micrometers, resulting in several millions of computational cells and raising immensely the computational cost and time, thus rendering the simulations virtually impossible.

In the current approach, the method of *computational parcels* is followed. Each parcel contains a number of drops with the same geometrical characteristics. The number of drops in each parcel depends on the number of computational parcels used to represent the fuel spray. Typical values are 3,000-30,000 parcels. In the current work the primary atomization is initialized with approximately 10,000 parcels and new parcels are created during the secondary atomization process including droplets produced during the various phases of breakup, with properties different than those of the parent drops.

3.2 Primary Breakup Models for Liquid Sheets and Jets

In Chapter 2 the physics governing the primary atomization mechanisms governing gasoline and diesel sprays were briefly discussed. In this section two computational models are presented that are currently used in CFD codes to capture the primary atomization process for each one of these applications. The Liquid Sheet Atomization Model has been adopted for gasoline sprays based on findings from Chryssakis et al. [2002, 2003].

3.2.1 Liquid Instability Sheet Atomization (LISA)

The Linearized Instability Sheet Atomization model (LISA) has been proposed by Schmidt et al. [1999] and Senecal et al. [1999] and is based on fluid mechanics principles in an attempt to eliminate the required experimental data. Due to centrifugal forces, at the exit of the orifice a liquid film is formed on the nozzle walls. The thickness of this film, h_o, is calculated from the mass flow rate equation:

$$\dot{m}_l = \pi \rho_l u h_o \left(d_o - h_o\right), \tag{3.1}$$

where u is the axial component of velocity at the nozzle exit. It is calculated from:

$$u = U \cdot cos\theta, \tag{3.2}$$

where θ is the half spray angle and U the relative fuel-air velocity, which is assumed to be equal to the liquid velocity, as the air is considered to be initially quiescent. The total velocity, is calculated as in Han at al, [1997], by

$$\mathrm{U} = \mathrm{K}_\mathrm{v} \sqrt{\frac{2\Delta \mathrm{P}_\mathrm{l}}{\rho_\mathrm{l}}} \,. \tag{3.3}$$

However, the relation of Lefebvre [1989] for K_v is not used here, as it may give values greater than unity, which are not desirable. Instead, it has been assumed that the swirl ports, in the interior of the injector are nozzles and a value of 0.7 has been selected, averaging the literature estimates. To guarantee that K_v is large enough to allow for sufficient mass flow, the following final expression has been used:

$$K_v = max\left[0.7, \frac{4\dot{m}_l}{\pi d_o^2 \rho_l \cos\theta} \sqrt{\frac{\rho_l}{2\Delta p}}\right]. \tag{3.4}$$

It should be noted here that values of up to K_v=0.85 have been experimentally measured.

Once the liquid sheet parameters have been calculated, the sheet breakup model is used. It assumes two-dimensional, viscous, incompressible liquid sheet with thickness 2*h* and velocity *U*, moving through a quiescent, inviscid, incompressible gas medium. The breakup occurs due to wave disturbances, with a growth rate approximated as:

$$\omega_r = -2\nu_l k^2 + \sqrt{4\nu_l^2 k^4 + QU^2k^2 - \frac{\sigma k^3}{\rho_l}}, \qquad (3.5)$$

where *Q* is the air-fuel density ratio and *k* the wave number. This expression is numerically maximized to find the maximum growth rate, *Ω*, which is then used for the evaluation of breakup time and length:

$$\tau = \frac{1}{\Omega}\ln\left(\frac{\eta_b}{\eta_o}\right) \qquad (3.6)$$

and

$$L = U\tau = \frac{U}{\Omega}\ln\left(\frac{\eta_b}{\eta_o}\right), \qquad (3.7)$$

where $\ln(\eta_b/\eta_o)$=12. The sheet half-thickness at *L* is given by:

$$h = \frac{2h_o\left[d_o - h_o\right]/\cos\theta}{2L\sin\theta + d_o - h_o} \quad , \qquad (3.8)$$

where δ_o is the film thickness, measured perpendicular to the injector axis, at the nozzle exit. At the point of breakup, fluid ligaments are formed with diameter calculated from the mass balance, as:

$$d_L = \sqrt{\frac{16h}{K_S}}, \qquad (3.9)$$

where K_S is the wave number corresponding to the maximum growth rate *Ω* and *h* the sheet thickness at the breakup location. The ligaments break up once the amplitude of the unstable waves is equal to the radius of the ligaments, giving droplets with diameter:

$$d_D = \left(\frac{3\pi d_L^2}{K_L} \right)^{1/3}, \tag{3.10}$$

with

$$K_L = \left[\frac{1}{2} + \frac{3\mu_l}{2(\rho_l \sigma d_L)^{1/2}} \right]^{-1/2} \cdot \frac{1}{d_L}, \tag{3.11}$$

which is the Weber result for the wave number corresponding to the maximum growth rate for the breakup of a cylindrical, viscous liquid column (the ligament in this case). From that point, the TAB model is used for the secondary breakup of the occurring droplets, which have sizes according to the Rosin-Rammler distribution. To take into account the turbulent drop-dispersion, the RNG k-ε model is used [Amsden, 1993].

3.2.2 Primary Jet Breakup

Solid cone sprays in KIVA are typically modeled by assuming a liquid core emerging from the nozzle, which disintegrates very fast into droplets. The liquid jet is modeled as “blobs” with initial diameter equal to the nozzle size. The WAVE breakup model [Reitz, 1987], [Reitz and Diwakar, 1987], is commonly used both for the primary and secondary atomization processes. This model is based on a linearized analysis of a Kelvin-Helmholtz instability of a stationary, round liquid jet immersed into a quiescent, incompressible gas. The result is a general dispersion equation, which relates the growth rate of an initial surface perturbation to its wavelength. Under the assumption that the size of the stripped off product droplets are proportional to the length of the fastest growing surface wave and that the rate of droplet generation is proportional to the maximal jet disturbance growth rate one obtains the expression for the radius and the time constant of the stripped off product droplet. The model is explained in detail in section 3.3.2.

3.3 Secondary Breakup Models

Five widely used secondary atomization models are described in this section, namely the TAB, WAVE, E-TAB, DDB and I-TAB models, and their behavior under different conditions is evaluated.

3.3.1 TAB Model

The TAB (Taylor Analogy Breakup) breakup model has been developed by O'Rourke and Amsden [1987] and is considered one of the standard models used for spray breakup calculations. The model is based on an analogy, suggested by Taylor and improved by Amsden and O'Rourke, between an oscillating and distorting droplet and a spring-mass system. The restoring force of the spring is analogous to the surface tension forces, while the external force on the mass is analogous to the gas aerodynamic force and the damping force represents the liquid viscosity effects. The advantage of the model over earlier approaches to the problem is the fact that it predicts that there is not a unique critical Weber number, but breakup of each droplet depends on the history of its velocity relative to the gas.

The main limitation of the TAB model is that it can only keep track of one oscillation mode, while in reality more than one oscillation modes exist. The model keeps track only of the fundamental mode, corresponding to the lowest order harmonic whose axis is aligned with the relative velocity vector between droplet and gas. This is the most important oscillation mode but for large Weber numbers other modes are also contributing significantly to drop breakup. Despite this limitation, rather good agreement is achieved between the numerical and experimental results for low Weber numbers.

The equation of a damped, forced harmonic oscillator is given by:

$$m\ddot{x} = F - kx - d\dot{x}\,, \tag{3.12}$$

where x is the displacement of the equator of the droplet from its equilibrium position, F are the external forces, k the spring's constant and d the damping parameter. In accordance with the Taylor analogy, the physical dependencies of the coefficients in Eq. (3.12) are

$$\begin{aligned} \frac{\boldsymbol{F}}{\boldsymbol{m}} &= \boldsymbol{C}_{\boldsymbol{f}} \frac{\boldsymbol{\rho}_{\boldsymbol{g}} \boldsymbol{u}^2}{\boldsymbol{\rho}_{\boldsymbol{l}} \boldsymbol{r}}, \\ \frac{\boldsymbol{k}}{\boldsymbol{m}} &= \boldsymbol{C}_{\boldsymbol{k}} \frac{\boldsymbol{\sigma}}{\boldsymbol{\rho}_{\boldsymbol{l}} \boldsymbol{r}^3}, \\ \frac{\boldsymbol{d}}{\boldsymbol{m}} &= \boldsymbol{C}_{\boldsymbol{d}} \frac{\boldsymbol{\mu}_{\boldsymbol{l}}}{\boldsymbol{\rho}_{\boldsymbol{l}} \boldsymbol{r}^2} \end{aligned} \tag{3.13}$$

where C_f, C_k, and C_d are dimensionless numbers. In addition, C_b is used to nondimensionalize x, by defining $y = x/(C_b r)$. Now, Eq. (3.12) can be written as:

$$\ddot{y} = \frac{C_f}{C_b} \frac{\rho_g}{\rho_l} \frac{u^2}{r^2} - \frac{C_k \sigma}{\rho_l r^3} y - \frac{C_d \mu_l}{\rho_l r^2} \dot{y}\,, \tag{3.14}$$

with breakup occurring if and only if $y>1$. Also, it is assumed that breakup occurs if and only if the amplitude of oscillation of the north and south poles equals the drop radius. The dimensionless constants C_f, C_k, and C_d are determined by comparing with experimental and theoretical results and have the following values: $C_k = 8$, $C_d = 5$, $C_b = 0.5$ and $C_f = 1/3$.

In order to predict the drop sizes after breakup, an equation based on energy conservation analysis is derived. The analysis equals the energy of the parent drop before breakup with the energies of the subsequent product drops after breakup and it yields:

$$\frac{r}{r_{32}} = 1 + \frac{8K}{20} + \frac{\rho_l r^3}{\sigma} \dot{y}^2 \left(\frac{6K-5}{120} \right), \tag{3.15}$$

where K must be evaluated experimentally by measuring drop sizes. In this work, a value of K=10/3, as suggested in [O'Rourke and Amsden, 1987] has been used.

Finally, the drop drag coefficient is assumed to depend on the magnitude of the drop deformation as follows:

$$C_D = C_{D,sphere}(1+2.632y), \tag{3.16}$$

which tends to overestimate the aerodynamic drag as will be shown in the next chapter.

3.3.2 WAVE Model

The WAVE breakup model was developed by Reitz and Diwakar [1987] and has been improved by Reitz [1987] and is based on a linearized analysis of a Kelvin-Helmholtz instability of a stationary, round liquid jet immersed into a quiescent, incompressible gas. The result is a general dispersion equation, which relates the growth rate of an initial surface perturbation to its wavelength. From numerical solutions it is shown that the maximum growth rate, Ω, and its corresponding wavelength, Λ, are approximated by:

$$\frac{\Lambda}{r_o} = 9.02\frac{\left(1+0.45Z^{0.5}\right)\left(1+0.4T^{0.7}\right)}{\left(1+0.87We^{1.67}\right)^{0.6}} \tag{3.17}$$

$$\Omega\left[\frac{\rho_L r_o^3}{\sigma}\right]^{0.5} = \frac{0.34+0.38We^{1.5}}{\left(1+Z\right)\left(1+1.4T^{0.6}\right)}, \tag{3.18}$$

where $Z=(We_L)^{1/2}/Re_L$, $T=Z(We_G)^{1/2}$. Under the assumption that the size of the stripped off product droplets are proportional to the length of the fastest growing surface wave and that the rate of droplet generation is proportional to the maximal jet disturbance growth rate, Ω, one obtains the expression for the radius, r, and the time constant, τ, of the stripped off product droplet as:

$$r=B_o\Lambda \tag{3.19}$$

$$\tau = 3.726B_1\frac{r_o}{\Lambda\Omega} \tag{3.20}$$

where the constants B_o=0.61 and B_1 is subject to further debate but suggested values are in the range 10-20. It is shown that in the limits $We \rightarrow 0$ and $We \rightarrow \infty$ the characteristic breakup time, τ, takes the form:

$$\tau = \begin{cases} 0.82 B_1 \sqrt{\dfrac{\rho_L r_o^3}{\sigma}}, \text{ for bag breakup} \\ B_1 \sqrt{\dfrac{\rho_L}{\rho_G}} \dfrac{r_o}{|U|}, \text{ for shear breakup} \end{cases} . \quad (3.21)$$

The conditions for bag and shear breakup are taken from experiments to be $We>6$ and $We/\sqrt{\mathrm{Re}_G} > 0.5$, respectively, with the Weber and Reynolds numbers based on the drop radius. The rate of change of the radius of the parent drop, r_o, is given by an exponential law so that the parent drop approaches the stripping drop size asymptotically:

$$\frac{dr_o}{dt} = -\frac{r_o - r}{\tau}, \quad r \le r_o \quad (3.22)$$

The difference of the models presented by Reitz & Diwakar [1987] and Reitz [1987] lies in the handling of the product droplets. In the first approach no distinction is made between the parent and product drops when their size is updated. In fact, the parent drop decays into products of identical size and no small drops are created. In the second approach the product droplets and the parent droplets are treated differently. While the size of the parent drop is still governed by the same rate equation, its mass decrease is compensated by the creation of product droplets of size r. With this breakup strategy there are more small droplets produced.

3.3.3 E-TAB Model

The Enhanced-TAB breakup model has been developed by Tanner [1997] in order to account for the different breakup regimes occurring in diesel engines environments. The dynamics of the TAB model have been left unchanged, but a different interpretation of the initial condition allows the modeling of the jet breakup, leading to considerably extended drop lifetimes. The rate of product drop creation is assumed to be proportional to the number of the product droplets and the proportionality constant depends on the breakup regime. In combination with the mass conservation principle this leads to an exponential decay law relating the mean mass of the product drops to the breakup time.

The main assumption made in the E-TAB model is that the rate of product droplet generation, $dn(t)/dt$, is proportional to the number of the product droplets, where the proportionality constant, K_{br}, depends on the breakup regime. According to this assumption:

$$\frac{dn(t)}{dt} = 3K_{br}n(t)\,, \tag{3.23}$$

where the factor 3 is introduced to simplify later expressions in the model. The model considers two breakup regimes, namely bag and stripping (shear) breakup. Bag breakup occurs if $We<160$ and stripping if $We>160$ (based on the diameter). The proportionality constant has values:

$$K_{br} = \begin{cases} k_1\omega, & \mathrm{We} \le 160 \\ k_2\omega\sqrt{We}, & \mathrm{We} > 160 \end{cases} \tag{3.24}$$

The values of k_1 and k_2 have been determined as $k_1 \approx k_2 = 4.5^{-1}$, but a smoothing function has been used to obtain a smooth transition between the two breakup regimes, making the transition insensitive to the limiting Weber number between the two regimes.

A uniform product droplet size distribution has been assumed and the new droplet radius is estimated as:

$$\frac{r}{r_o} = e^{-K_{br} t} , \tag{3.25}$$

where r_o and r are the radii of the parent and product drops, respectively. The breakup time in equation (3.25) is calculated as in the TAB model.

3.3.4 Droplet Deformation Breakup (DDB)

Ibrahim et al. [1993] proposed the Droplet Deformation Breakup (DDB) model, which is based on the drops dynamics in terms of the motion of the center-of-mass of the half-droplet. It is assumed that the liquid drop is deformed due to a pure extensional flow from an initial spherical shape of radius r_o into an oblate spheroid having an ellipsoidal cross-section with major semi-axis a and minor semi-axis b. The internal energy of the half-drop comes from the sum of its kinetic and potential energies, $\dot{E}$, expressed as follows:

$$\dot{E} = \frac{2}{3}\pi r_o^3 \rho_L \dot{y}_1 \ddot{y}_1 + \frac{9\pi^2\sigma}{8} y_1 \left[1 - 2\left(\frac{c y_1}{r_o} \right)^{-6} \right] \dot{y}_1 \tag{3.26}$$

where $c=3\pi/4$ and y_1 is the distance from the center-of-mass of the deforming half-droplet to its pole. It is assumed that $\dot{E}$ is equal to the work done by pressure and viscous forces, $\dot{W}$, which can be expressed as follows:

$$\dot{W} = -\frac{\pi}{4} r_o^2 \rho_G u^2 \dot{y}_1 + \frac{8}{3}\pi r_o^3 \mu_L \left(\frac{\dot{y}_1}{y_1} \right)^2 \tag{3.27}$$

Letting $y^*_1 = y_1/r_o$ to non-dimensionalize and dropping the asterisk, equations (3.26) and (3.27) yield:

$$\ddot{y}_1 + \frac{4N}{\mathrm{Re}K}\frac{1}{y_1^2}\dot{y}_1 + \frac{27\pi^2}{16WeK}y_1\left[1-2(cy_1)^{-6}\right] = \frac{3}{8K}, \tag{3.28}$$

where *K* is the liquid-gas density ratio, *N* the liquid-gas viscosity ratio and *Re* and *We* numbers are based on the drop radius. By solving equation (3.28) the major and minor semi-axes of the droplet can be obtained as:

$$a = 3\pi r_o \frac{y_1}{4},\ b = \frac{r_o^3}{a^2} \tag{3.29}$$

The DDB model is applicable to the shear breakup regime (assumed to start at *We>40*). The aerodynamic drag coefficient is proportional to the deformed droplet normal cross-sectional area:

$$C_D = C_{D,sphere}\frac{a^2}{r_o^2} = C_{D,sphere}\frac{9\pi^2}{16}y_1^2, \tag{3.30}$$

which is an improvement over the previous approach followed by TAB and E-TAB.

3.3.5 Improved TAB Model

An Improved TAB model has been proposed by Park, Yoon & Hwang [2002]. The effects of the drop deformation on the aerodynamic drag have been considered and two breakup regimes (bag and shear breakup) are taken into account. A new breakup criterion has been introduced to predict more accurate breakup times; it is assumed that breakup occurs when the internal liquid-phase pressure of the deformed droplet at the equator is greater than that of the pole.

The deformed droplet shape is assumed to be an oblate spheroid having an ellipsoidal cross-section, the same as in the DDB model. The surface tension restoring force and the viscous damping force are the same as in the TAB model but the aerodynamic drag force, *F*, is:

$$\frac{F}{m} = C_F \frac{\rho_G a^2 u^2}{\rho_L r_o^3} \tag{3.31}$$

with

$$a = r_o + x = r_o(1 + C_b y) = r_o(1 + 0.5y) \tag{3.32}$$

Hence, equation (3.12) can be written as:

$$\ddot{y} + \frac{5N}{\mathrm{Re}\,K}\dot{y} + \frac{1}{K}y\left(\frac{8}{We} - 2C_F - 0.5C_F y\right) = \frac{2C_F}{K}, \tag{3.33}$$

where *K* is the liquid-gas density ratio, *N* the liquid-gas viscosity ratio and *Re* and *We* numbers are based on the drop radius. This equation is being solved with a 4th order Runge Kutta ordinary differential equation solver. The aerodynamic external force coefficient, C_F, has been determined as C_F=4/19, by assuming that the critical Weber number (based on the radius) is 6, as in the TAB model.

The transition criterion between the bag and the shear breakup regime has been set to We=19 (base on radius, corresponding to 38 based on diameter). If *We*>19 the increased external force is greater than the restoring surface tension force and this tends to increase the droplet major semi-axis. It is proposed that atomization occurs when the rate of change of the external force with respect to the droplet major semi-axis is greater than the rate of change of the restoring force:

$$\frac{\partial F_{external}}{\partial a} > \frac{\partial F_{restoring}}{\partial a}. \tag{3.34}$$

The breakup criterion for this model has been based on the assumption that breakup occurs when the internal liquid-phase pressure of the deformed droplet at the equator is greater than that of the pole. An analysis of the internal flow in the drop, leads to the following criterion, based on the drop deformation:

$$2(1+0.5y)^5+(1+0.5y)^{-1}-4(10.5y)^{-4}>2.5107We. \tag{3.35}$$

Finally, the aerodynamic drag coefficient is proportional to the deformed droplet cross-sectional area:

$$C_D = C_{D,sphere}\frac{a^2}{r_o^2} = C_{D,sphere}(1+0.5y)^2. \tag{3.36}$$

3.4 Evaluation of Secondary Breakup Models

A large number of simplifying assumptions and adjustable empirical parameters have been required in the early days of spray modeling in order to achieve satisfying representation of some common fuel sprays. It is of particular interest to evaluate these models by comparing their predictions with the physical concepts presented in Chapter 2. It will be shown here that the assumptions used, as well as the lack of detailed knowledge of the physical phenomena, led to models that can perform well under a narrow range of conditions but re-calibration is required if the model is to be used for a different nozzle or even for different ambient conditions. The evaluation includes the breakup criteria for various breakup regimes, breakup times, and resulting droplet sizes.

3.4.1 Breakup Regimes

Evaluation of the secondary breakup models in terms of the breakup regimes will be done based on the classification provided by Faeth, as described in Chapter 2. In Figure 12 the *We* and *Oh* number are plotted for droplets found in typical gasoline and diesel sprays, under various ambient conditions. For gasoline sprays used in direct-injected spark-ignited systems, swirl sprays have been simulated with injection pressure of 5 MPa and ambient pressures varying from 0.1 to 1.0 MPa, representing early to late injection timings respectively. The shaded area represents both the pre-swirl and the main part of the spray. The diesel spray calculations have been performed with injection pressures of 30-210 MPa, ambient pressures 3-6 MPa and ambient temperature 400-800 K. It is very interesting to note that all calculations yield $Oh<0.2$, resulting in breakup regimes that can be determined only as a function of *We*.

For gasoline sprays it has been observed that as the ambient pressure increases, *We* increases as well, due to its dependency on the ambient gas density. A wide range of breakup regimes, including the oscillatory deformation, bag, multimode and shear breakup are important for gasoline sprays, according to injection pressure and ambient conditions. It has been also found [Chryssakis, 2002, Chryssakis et al., 2003] that the pre-swirl spray is not successfully represented when the TAB model is used both for the main and the pre-swirl spray breakup.

For diesel sprays it appears that the shear and catastrophic breakup regimes are the main areas of interest and in the limit of low injection and ambient pressures the multimode breakup mechanism plays a role as well. For early injection timings, such as the ones used in premixed diesel combustion strategies (60-40 deg. before TDC), the cylinder pressure is considerably lower, leading to much lower *Weber* numbers. Finally, the effect of secondary atomization in small bore diesel engines might be negligible compared to the effect of wall impingement phenomena. In these engines, the mean time for a drop to hit the wall is of the order of 0.1-0.2 ms, which is the same order of magnitude with the initiation of breakup time, as will be shown in the followings.

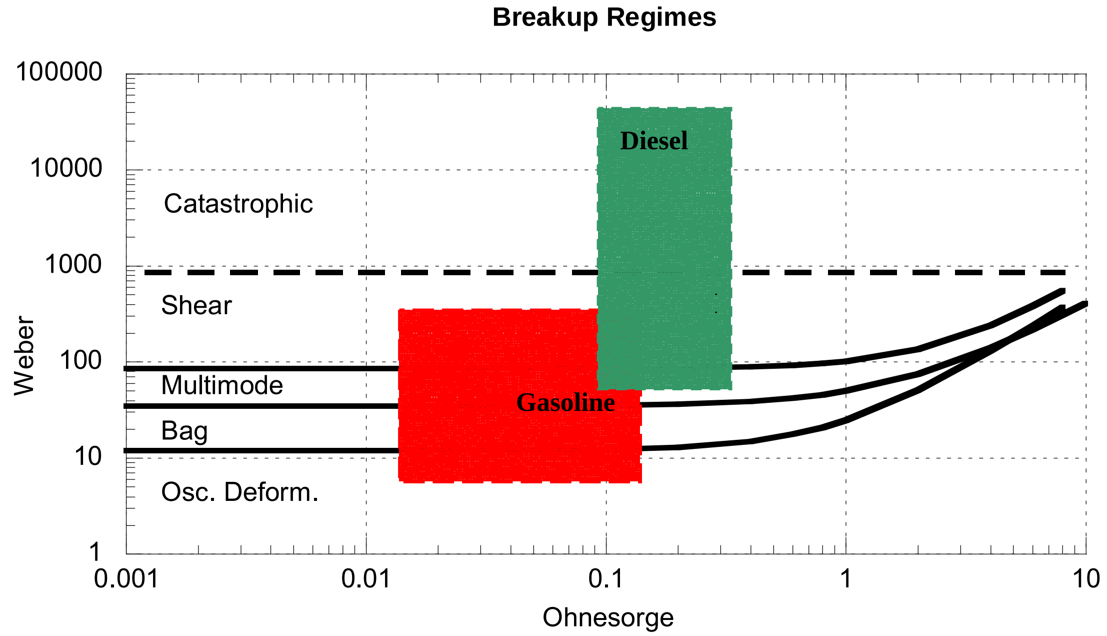

Figure 12: Breakup Regimes for various fuel sprays.

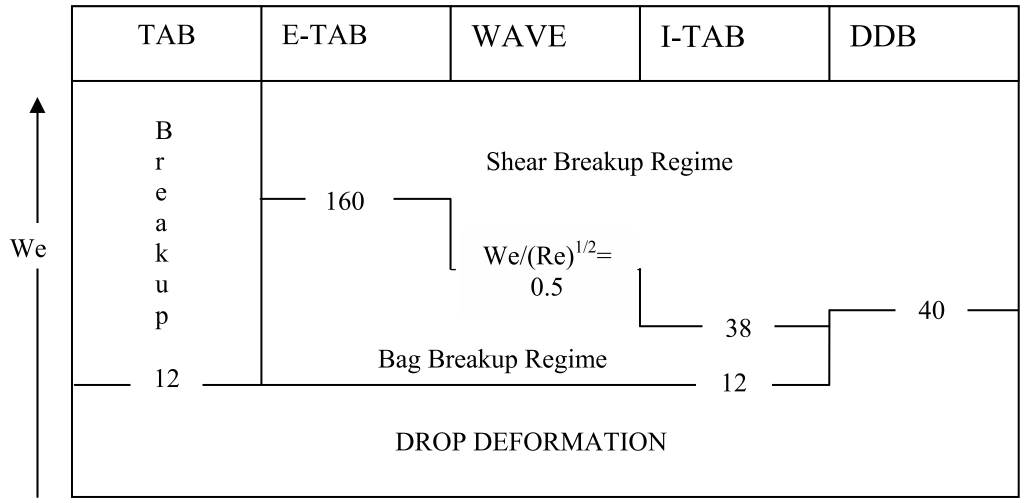

Figure 13: Breakup Regimes for various secondary atomization models.

In Figure 13 the models reviewed in the previous sections are compared on the basis of the breakup regime consideration. The TAB and DDB models only account for one breakup regime, while E-TAB, WAVE and I-TAB predict two regimes, namely the bag and shear breakup, in addition to the drop deformation.

The E-TAB and I-TAB models employ transition criteria based on the *We* number. The transition criterion between the two regimes has been set to 160 for the E-TAB model and 38 for I-TAB. Hence, it can be concluded that the multimode breakup is assumed to be part of the shear breakup mechanism in the I-TAB and part of the bag breakup for E-TAB. The WAVE model has its own transition criterion, based on observations by [Nicholls, 1972], involving not only the *We* but also the *Re* of a drop. It can be proven that this is strongly dependent on the ambient conditions and can lead to erroneous judgment on the breakup mechanism selection, since in some cases it can predict that the drops are in the shear breakup regime even for *We* very close to 12. The DDB model considers only the shear breakup mechanism, starting at *We*=40.

The breakup regime determines the physical mechanism governing the breakup process of a given droplet; however it is not sufficient to judge whether a drop will breakup or not. There are three criteria that have to be simultaneously fulfilled in order for a drop to breakup. First, the *We* number of the drop has to be larger than a lower limit, set to 12 for low *Oh* numbers. Second, the initiation of breakup time has to be reached and third, the drop acceleration should be high enough in order to trigger surface disturbances that will result in drop breakup. In Chapter 2 the *Eötvös* number that controls this process has been defined. It has been found experimentally that for *Eo*<16 breakup no longer occurs. In experiments performed by [Hsiang and Faeth, 1993] the *Eo* was always below this limit after secondary breakup, thus preventing tertiary breakup from happening, even though the *We* might be in one of the breakup regimes. Therefore, this criterion should be included in a secondary breakup model to avoid tertiary breakup calculations that do not represent real processes.

3.4.2 Initiation and End of Breakup Times

The secondary breakup is a process that does not occur instantaneously but can last hundreds of microseconds. It starts at the initiation of breakup time and is completed at the end of breakup time. In Chapter 2 these times were defined and empirical correlations have been provided for estimating the dimensionless time as a function of the *We* number. Here these correlations are used to estimate the process in real time and compare the theoretical equations with predictions from the computational model. A big drawback of most of the models is that they only provide a single breakup time, corresponding to an instantly occurring breakup. Only the WAVE model introduces a breakup rate that can be adjusted to match experimental measurements. The breakup times are defined in a similar way for the TAB, E-TAB and WAVE models, varying only on the constants used. They are all based on the equation:

$$\tau = \begin{cases} C_1\sqrt{\dfrac{\rho_L r_o^3}{\sigma}}, \text{ for bag breakup} \\ C_2\sqrt{\dfrac{\rho_L}{\rho_G}}\dfrac{r_o}{|U|}, \text{ for shear breakup} \end{cases} \tag{3.37}$$

where bag and shear breakup are determined according to the criteria shown in Figure 13. The TAB model uses two different equations for estimating the breakup time, according to the *We* number. However, the mechanism used for drop breakup, deformation and aerodynamic drag do not depend on the *We* number. In Table 1 the values of C_1 and C_2 are summarized for the three models.

	TAB	**E-TAB**	**WAVE**
C_1	1.11	1.59	2.221
C_2	1.732	1.59	1.732-20

Table 1: Constants used for estimation of breakup time.

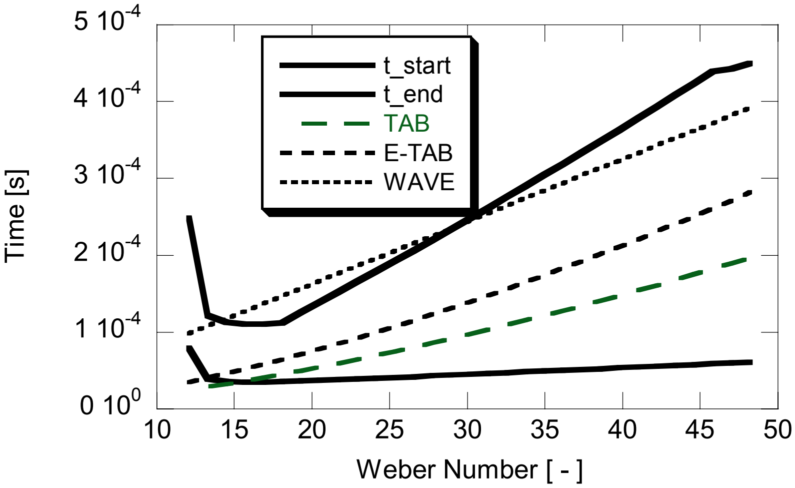

Figure 14: Comparison of breakup times for the TAB, E-TAB and WAVE models, ambient pressure 0.1 MPa.

A comparison of the three above listed models plotted against theoretical predictions for the initiation and end of breakup is demonstrated in Figure 14 and Figure 15 for typical gasoline sprays injected in ambient pressures 0.1 and 0.4 MPa, where t_1 and t_2 denote initiation and end of breakup times respectively. For the WAVE model a value of C_2=10 has been used. It is remarkable that the combination of *We* and *Re* indicated that the drops are in the shear breakup regime throughout the entire range of *We* numbers. It appears that the TAB breakup model predicts quite well the start of breakup, especially for low *We*, but it has the drawback that breakup occurs instantaneously. The effect of this flaw increases for high Weber numbers, when the breakup duration in the order of

0.5-1.0ms and can lead to significant inaccuracies in the droplet size and aerodynamic drag on the droplets.

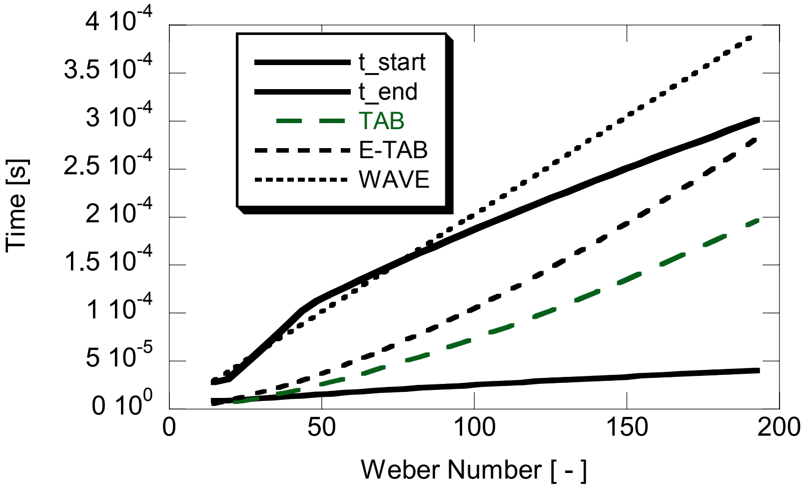

Figure 15: Comparison of breakup times for the TAB, E-TAB and WAVE models, ambient pressure 0.4 MPa.

Also, from Figure 14 and Figure 15 it can be concluded that the E-TAB model provides an average breakup time, while the constant C_2 in the WAVE model should be tuned to give acceptable results.

The DDB model has not been evaluated here since it is only applicable in the shear breakup regime. The I-TAB breakup criterion is based on more complicated breakup time factors, determined by considering the internal flow of a drop and cannot be expressed with a simple expression.

3.4.3 Resulting Droplet Sizes

To predict the drop sizes after breakup the TAB model uses an energy conservation equation considering the minimum surface energy and the energy in oscillation and distortion. It is assumed that after breakup the product drops are not distorted or oscillating. Hence, the energy after breakup is the sum of the minimum surface and the kinetic energy of the product drops. In the bag breakup regime (low *We*) this energy balance yields

$$r=(3/7)r_o \tag{3.38}$$

while for large *We*:

$$r \approx \frac{6\sigma}{\rho_G u^2}, \tag{3.39}$$

which corresponds to a *We*=12 (based on diameter), indicating that the calculation is still relate to the bag breakup mechanism criteria.

The E-TAB follows a different strategy for estimating the resulting drop size after breakup. It is assumed that the rate of product droplet generation is proportional to the number of the product droplets, where the proportionality constant, K_{br}, depends on the breakup regime. This assumption, combined with a uniform product droplet size distribution leads to:

$$r = r_o e^{-K_{br}t} \tag{3.40}$$

with the proportionality constant having the values:

$$K_{br} = \begin{cases} \omega/4.5, & \mathrm{We} \le 160 \\ \omega\sqrt{We}/4.5, & \mathrm{We} > 160 \end{cases}, \tag{3.41}$$

where ω is given by:

$$\omega = \sqrt{8\frac{\sigma}{\rho_L r^3} - \frac{1}{t_d^2}} \quad \text{and} \quad t_d = \frac{2\rho_L r^2}{5\mu_L}. \tag{3.42}$$

The selection of a uniform size distribution is not realistic but it is expected to provide good approximations when averaged over a wide range of drop sizes because parent drops of different sizes and *We* numbers will in general yield a wide range of product droplet sizes.

The WAVE breakup model adopts a fundamentally different approach for the calculation of the product drop size. New drops are formed from a parent drop with radius:

$$r = \begin{cases} B_o\Lambda, & B_o\Lambda \le r_o \\ \min\begin{bmatrix} \left(3\pi r_o^2 u/2\Omega\right)^{1/3} \\ \left(3r_o^2\Lambda/4\right)^{1/3} \end{bmatrix}, & \mathrm{B_o}\Lambda > r_o \end{cases} \tag{3.43}$$

where B_o, Λ, Ω are defined in the description of the WAVE model in Chapter 3. The breakup times given in equation (3.37) and Table 1 are used for the onset of breakup. In case of shear breakup, a breakup rate is defined (equation 3.25), providing a gradual decrease for the diameter of the core drop. This is a good approximation, provided that the breakup time constants are correctly adjusted and the transition between bag and shear breakup regimes is well established.

CHAPTER 4

PROPOSED DROP DEFORMATION AND BREAKUP MODEL

The computational model developed in this work is described in this chapter and it consists of three main parts: primary atomization, drop deformation and aerodynamic drag, and secondary atomization. Each one of these components is thoroughly presented along with parametric studies of the behavior of each component under various conditions.

4.1 Primary Atomization

The primary atomization model used in this study is based on the work of Huh, Lee and Koo [1998]. The model considers the effects of both infinitesimal wave growth on the jet surface and jet turbulence including cavitation dynamics. Initial perturbations on the jet surface are induced by the turbulent fluctuations in the jet, originating from the shear stress along the nozzle wall and possible cavitation effects. This approach overcomes the inherent difficulty of wave growth models, where the exponential wave growth rate becomes zero at zero perturbation amplitude.

The model is based on two main assumptions:

(i) the length scale of turbulence is the dominant length scale of atomization:

$$L_A = C_1 L_t = C_2 L_w \tag{4.1}$$

where L_t and L_w are the turbulence length scale and the wavelength of surface perturbations respectively.

(ii) the time scale of atomization is the linear sum of the turbulence and wave growth time scales:

$$\tau_A = C_3\tau_t + C_4\tau_w \tag{4.2}$$

where τ_t is the turbulence time scale and τ_w the wave growth time scale that determines the exponential growth rate. The empirical constants C_1 to C_4 are set to 2.0, 0.5, 1.2 and 0.5 respectively.

The initial turbulence length and time scale are calculated using average quantities for the turbulent kinetic energy and energy dissipation rate as:

$$\boldsymbol{L}_t^0 = \boldsymbol{C}_\mu \frac{\boldsymbol{k}_{avg}^{3/2}}{\boldsymbol{\varepsilon}_{avg}} \tag{4.3}$$

$$\boldsymbol{\tau}_t^0 = \boldsymbol{C}_\mu \frac{\boldsymbol{k}_{avg}}{\boldsymbol{\varepsilon}_{avg}} \tag{4.4}$$

where C_μ=0.09 and the average quantities are estimated as:

$$\boldsymbol{k}_{avg} = \frac{\boldsymbol{U}^2}{8(\boldsymbol{L}/\boldsymbol{D})}\left[\frac{1}{\boldsymbol{c}_d^2} - \boldsymbol{K}_c - \left(1-\boldsymbol{s}^2\right)\right] \tag{4.5}$$

$$\boldsymbol{\varepsilon}_{avg} = \boldsymbol{K}_\varepsilon \frac{\boldsymbol{U}^3}{2\boldsymbol{L}}\left[\frac{1}{\boldsymbol{c}_d^2} - \boldsymbol{K}_c - \left(1-\boldsymbol{s}^2\right)\right] \tag{4.6}$$

where *L, D* are the nozzle length and diameter, c_d the nozzle discharge coefficient, K_c is a constant taking into account losses in the contraction corner (typically set to 0.45), K_ε is a constant for average turbulent energy dissipation, set to 0.27, and *s* is the area ratio at the nozzle contraction.

The resulting turbulence length and time scale are given as a function of the time and the initial turbulence conditions as:

$$\boldsymbol{L}_{\boldsymbol{t}}(\boldsymbol{t}) = \boldsymbol{L}_{\boldsymbol{t}}^{0}\left(1 + \frac{0.0828\boldsymbol{t}}{\boldsymbol{\tau}_{\boldsymbol{t}}^{0}}\right)^{0.457} \tag{4.7}$$

$$\boldsymbol{\tau}_{\boldsymbol{t}}(\boldsymbol{t}) = \boldsymbol{\tau}_{\boldsymbol{t}}^{0} + 0.0828\boldsymbol{t} \tag{4.8}$$

The wave growth timescale is approximated by neglecting the surface tension and viscous effects and maintaining only the aerodynamic destabilizing term:

$$\boldsymbol{\tau}_{\boldsymbol{w}} = \frac{\boldsymbol{L}_{\boldsymbol{w}}}{\boldsymbol{U}}\sqrt{\frac{\rho_{\boldsymbol{L}}}{\rho_{\boldsymbol{G}}}} \tag{4.9}$$

The liquid jet is represented in the form of computational parcels with breakup rate proportional to the ratio of the atomization length and time scale:

$$\frac{\boldsymbol{dD}_{\boldsymbol{p}}}{\boldsymbol{dt}} = \boldsymbol{k}_{1}\frac{\boldsymbol{L}_{\boldsymbol{A}}}{\boldsymbol{t}_{\boldsymbol{A}}} \tag{4.10}$$

where the constant k_1 has been set to 0.5. The resulting drop size is assumed to be equal to the atomization length scale, L_A, as calculated with equation (4.1). When the reduced primary parcel reaches the size of the secondary droplet, the primary atomization process for this parcel is assumed to be completed and the secondary atomization model is engaged to model its behavior.

In order to take into account the aerodynamic forces on the liquid core, is assumed that the liquid core is wedge-shaped, with an aerodynamic drag coefficient of C_D=0.3, according to [Munson, Young and Okiishi, 1994]. This assumption may have to be corrected by increasing the drag coefficient to take into account the instabilities on the liquid/gas interface that disturb the liquid surface and the gas flow around the liquid core.

4.1.1 Effect of Turbulence Modeling on Primary Atomization

A sensitivity analysis has been performed in order to evaluate the behavior of the primary atomization model and to explore the effect of the turbulence parameters on breakup time, breakup rate, liquid core length and resulting drop size. The effect of K_ε, used for estimating the average turbulent energy dissipation, is studied here.

The effect of K_ε is studied by testing values ranging from 50% to 200% of the original value proposed by Huh et al. [1998]. As shown in Figure 16, increasing K_ε results in faster atomization rates, shorter breakup time and increased resulting drop size. The longer breakup times obtained with low K_ε values lead some of the parcels representing the liquid core to travel very far before undergoing primary atomization. To illustrate this, a parcel with velocity of 300 m/s undergoing primary breakup at 0.05 msec after injection, will travel 15 mm before a spherical drop is created. This is a reasonable liquid core breakup length, according to Siebers [1998]; however, a breakup time of 0.15 or 0.2 msec would result in a breakup length of approximately 45-60 mm, which is very long under these conditions. Therefore, a larger rather than a lower value of K_ε is more likely to give meaningful results.

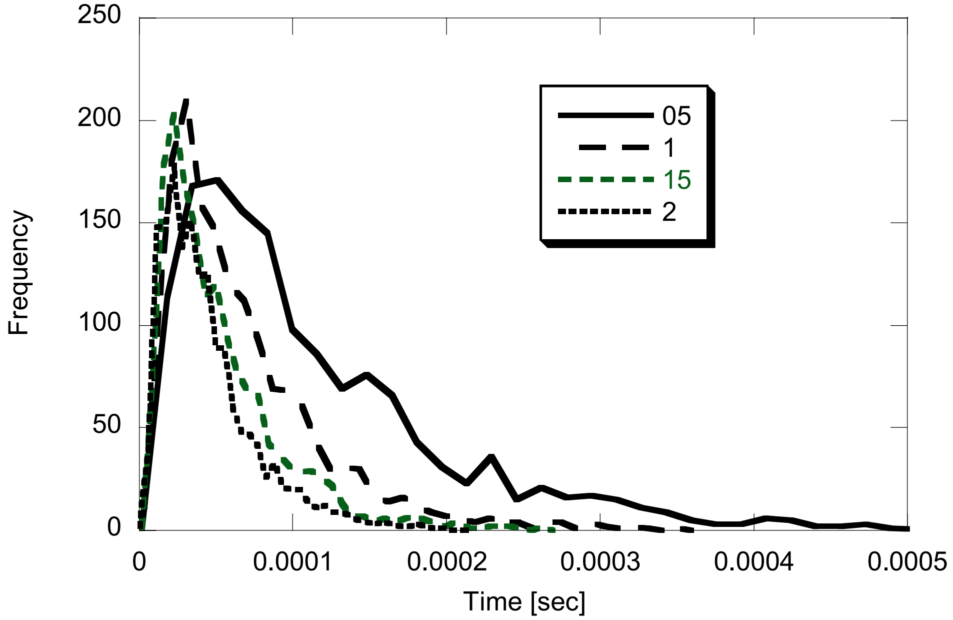

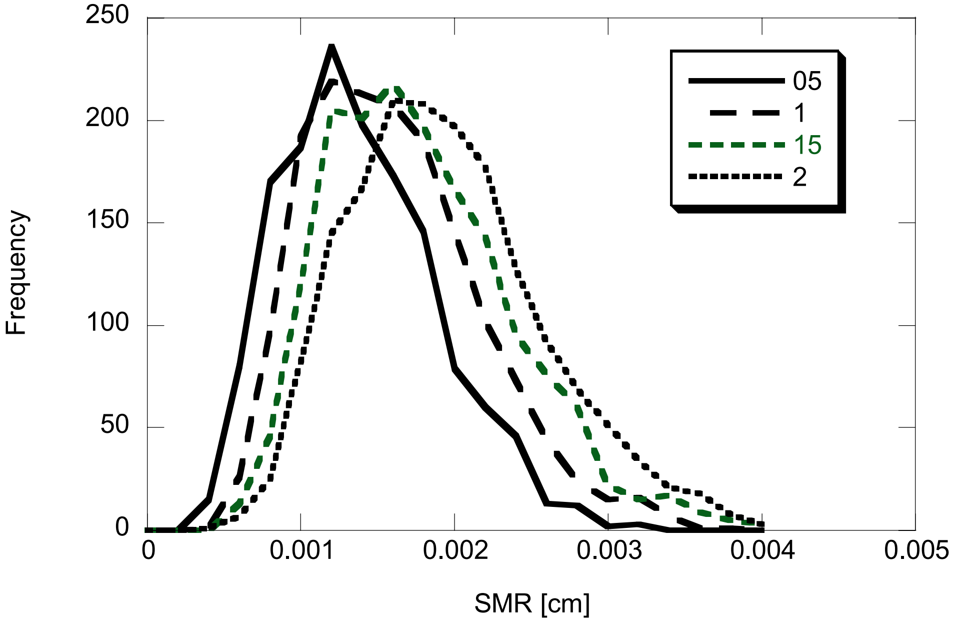

Figure 16: Effect of parameter $\boldsymbol{K_\varepsilon}$ on primary breakup rate and predicted drop size.

4.1.2 Spray Cone Angle Predictions

The cone angle of the spray can be predicted if the normal component of the velocity of the resulting drops is known. According to Hue et al. [1998], the cone angle can be estimated as:

$$\tan\frac{\boldsymbol{\theta}}{2} = \frac{\boldsymbol{L_A}/\boldsymbol{\tau_A}}{\boldsymbol{U}} \tag{4.11}$$

It was found in this work that the predictions, based on the new C_μ and K_ε values tend to underestimate the spray cone angle. This has been corrected by introducing an empirical factor, doubling the model predictions:

$$\boldsymbol{\theta} = 4 \cdot \tan^{-1}\left(\frac{\boldsymbol{L_A}/\boldsymbol{\tau_A}}{\boldsymbol{U}}\right) \tag{4.12}$$

The corrected equation predicts the measured spray cone angles very well, as will be shown in the next chapter.

The spray cone angle prediction has been introduced in KIVA by injecting the primary parcels with velocity parallel to the injector axis and assigning a normal component of velocity to the produced spherical drops, corresponding to the predicted cone angle.

4.2 Drop Deformation and Aerodynamic Drag

Drops created as a result of the primary atomization of the liquid core are assumed to have the shape of a perfect sphere. These drops start deforming, taking the shape of an oblate spheroid as they start moving through the ambient gas. As explained in Chapter 2, the maximum drop distortion can be:

$$\frac{\boldsymbol{d}_{\boldsymbol{c}\,\max}}{\boldsymbol{d}_{\boldsymbol{o}}} = \begin{cases} 1 + 0.19\boldsymbol{We}^{1/2}, & 100 < \boldsymbol{We} \\ 2 & We > 100 \end{cases} \tag{4.13}$$

The drop distortion as a function of time is given by:

$$\frac{\boldsymbol{d}_{\boldsymbol{c}}}{\boldsymbol{d}_{\boldsymbol{o}}} = 1 + \left(\frac{\boldsymbol{d}_{\boldsymbol{c}\,\max}}{\boldsymbol{d}_{\boldsymbol{o}}} - 1 \right) \frac{\boldsymbol{t}}{\boldsymbol{t}_{\max}}, \tag{4.14}$$

where

$$\frac{\boldsymbol{t}_{\max}}{\boldsymbol{t}^{*}} = 1.53 \left(\frac{\boldsymbol{d}_{\boldsymbol{c}\,\max}}{\boldsymbol{d}_{\boldsymbol{o}}} - 1 \right)^{0.52}, \text{ for } Re\text{>}50. \tag{4.15}$$

Once the drop distortion is known, the aspect ratio can be calculated, as:

$$\boldsymbol{E} = \frac{\boldsymbol{d}_{\min}}{\boldsymbol{d}_{\max}} = \frac{1}{\boldsymbol{d}_{\max}} \cdot \frac{\boldsymbol{d}_{\boldsymbol{o}}^{3}}{\boldsymbol{d}_{\max}^{2}} = \left(\frac{\boldsymbol{d}_{\boldsymbol{o}}}{\boldsymbol{d}_{\max}} \right)^{3} \tag{4.16}$$

The correlation adopted here (from Clift et al. [1978]) for the drag coefficient of a liquid sphere (E=1), is:

$$\boldsymbol{C}_{\boldsymbol{D}} = \frac{24}{\mathrm{Re}} \left[1 + 0.15\,\mathrm{Re}^{0.687} \right] + \frac{0.42}{1 + 4.25\,\mathrm{Re}^{-1.16} \cdot 10^{4}}, \; Re\text{<}3\times10^{5}. \tag{4.17}$$

For liquid disks, $E \rightarrow 0$, one can use

$$\boldsymbol{C}_{\boldsymbol{D}} = \frac{64}{\boldsymbol{\pi}\,\mathrm{Re}} \left(1 + 0.138\,\mathrm{Re}^{0.792} \right), \; 1.5\text{<}Re\text{<}133 \tag{4.18}$$

$$C_D=1.17,\ Re>133 \tag{4.19}$$

For oblate spheroids with aspect ratio E=0.5, Clift et al. suggest:

$$\boldsymbol{C_D} = 108.42\,\mathrm{Re}^{\left(-1.66+.3958\log \mathrm{Re}-0.03\log^2 \mathrm{Re}\right)},\ 40<Re<10^4. \tag{4.20}$$

For intermediate values of the aspect ratio, E, linear interpolation is used in the model. The Reynolds number in the correlations for the disk and the spheroid is based on the cross-sectional diameter, d_c.

4.3 Secondary Atomization

The secondary atomization is modeled using a classification of breakup mechanisms in four breakup regimes, as described by [Faeth, Hsiang and Wu, 1995] and [Pilch and Erdman, 1987]. This classification includes the bag, multimode, shear and catastrophic breakup regimes. The modeling approach for each one of these mechanisms is described in this section and the main characteristic is that the secondary atomization is modeled as a rate process and does not occur instantaneously. The initiation and end of breakup times are given by equations (2.16)-(2.21).

4.3.1 Bag Breakup Regime

Liquid drops are subject to the *bag* breakup mechanism for Weber numbers $12<We<20$ and $Oh<0.1$. Even though this mechanism covers only a very narrow range of Weber numbers, it is worth studying because a large number of droplets fall in this regime for gasoline sprays injected under atmospheric conditions (usually encountered in early injection strategies for homogeneous charge). Furthermore, it is the basis for modeling part of the *multimode* breakup mechanism.

According to the bag breakup mechanism, a drop is separated into two distinct parts, the basal ring and the bag. Each one of these parts deforms and breaks up into smaller drops. Therefore, for accurate representation of the mechanism, for each parcel undergoing bag breakup, an additional parcel will be created to represent the bag, while the original parcel will represent the basal ring. The formation and breakup process of these two entities is described here as a function of time.

According to experimental observations by [Chou and Faeth, 1998], the basal ring forms at t/t^*=2 and starts growing until t/t^*=5, where it breaks up. The mean ring diameter can be described as:

$$\frac{\boldsymbol{d_p}}{\boldsymbol{d_o}} = \begin{cases} \frac{1}{4}\left(\frac{\boldsymbol{t}}{\boldsymbol{t}^*}\right)^2 - 0.18\left(\frac{\boldsymbol{t}}{\boldsymbol{t}^*}\right) + 1.43, & \mathbf{2} \le \left(\frac{\boldsymbol{t}}{\boldsymbol{t}^*}\right) \le 4 \\ 1.79\left(\frac{\boldsymbol{t}}{\boldsymbol{t}^*}\right) - 2.51, & \mathbf{4} \le \left(\frac{\boldsymbol{t}}{\boldsymbol{t}^*}\right) \le 5 \end{cases} \tag{4.21}$$

The ratio of the liquid volume in the basal ring, V_r, to the initial volume of the parent drop, V_o, has been measured to be approximately 0.56, even though later experiments [Dai and Faeth, 2001] did not confirm this value. The diameter of the tube that forms the ring is given by:

$$\frac{\boldsymbol{d_r}}{\boldsymbol{d_o}} = 0.35\left(\frac{1}{\boldsymbol{d_p}/\boldsymbol{d_o}}\right)^{1/2} \tag{4.22}$$

Upon breakup, two types of drops are formed from the basal ring: node drops and drops from the cylindrical portions of the ring between the nodes. From the ring-like portions, drops are produced according to the Rayleigh mechanism, as confirmed by experimental observation. Accounting for both types of drops, the average drop diameter is $0.3d_o$.. Based on conservation of mass considerations, 21 drops are produced from the basal ring (with a diameter equal to $0.29876d_o$, for mass conservation) and their diameters are distributed around the mean value as:

$$MMD/SMD=1.2. \tag{4.23}$$

The aerodynamic drag coefficient for the ring is assumed to be equal to the aerodynamic drag coefficient for a cylinder in cross-flow, since $d_p>>d_r$. The drag coefficient for a cylinder is given by [White, 1990], as:

$$\boldsymbol{C}_{\boldsymbol{D}} = 1 + \frac{10}{\mathrm{Re}_{\boldsymbol{D}}^{2/3}}. \tag{4.24}$$

The cross-sectional area used for the calculation of the aerodynamic force is given as the cross-sectional area of the cylinder, $A=\pi d_p d_r$. The Reynolds number is based on the tube diameter, d_r. This value should be used for $t/t^*>3$. For earlier timings, the value for the bag will be used.

The bag starts forming forms at $t/t^*=2$ and growing up to $t/t^*=3$, when it starts disintegrating. A very fine, approximately monodisperse drop cloud is formed, with drop diameters equal to $0.04d_o$. The volume of the bag was measured at 0.44 of the total volume. Mass continuity results to 6875 droplets produced from this process.

The aerodynamic drag coefficient in this case will be assumed to be equal to the average of the drag coefficient of a perfect sphere and the one of a flat disc. These coefficients will be calculated based on the correlations given above for the drop deformation phase and Reynolds number based on the ring diameter, d_p. The frontal area used for calculating the aerodynamic force is given as $A=\pi d_p^2$. These values will be used for $2< t/t^*<3$, since the bag is still attached to the ring during this period of time.

4.3.2 Multimode Breakup Regime

A drop undergoes *multimode* breakup when its initial Weber number is in the range of $20<We<80$. The multimode breakup regime can be subdivided into a bag/plume regime for $20<We<40$, and a plume/shear regime for $40<We<80$. The first mechanism resembles the bag breakup mechanism, while the second one has similarities with the shear breakup, described in the next sections. In the bag/plume regime, a bag forms and grows, while a "plume" also appears. As the Weber number increases, the bag shrinks until it disappears and only a small plume and a core drop are apparent.

After the initial drop deformation for $t/t^*<2$, a ring and a bag structure start forming for relatively low We numbers ($We<40$). In addition, a "plume" drop appears in the middle of the bag, in the form of a cylinder, aligned with the flow. For higher We numbers, $We>40$, a small plume and a core drop appear and the ring and bag structures are not observed any longer. In the followings, correlations for the volume of each one of these parts are given, as a function of the Weber number. It will be assumed that each one of these parts has constant volume for the short period of time of its existence.

In Table 2, the volume fractions, normalized using the initial volume of the drop, are given as functions of the Weber number for $We<40$. For $40<We<80$, it is assumed that the core drop equals to 90% of the initial drop volume, while the plume takes up the rest 10% of the volume [Dai, Faeth, 2001].

STRUCTURE	VOLUME FRACTION
Ring	$V_{ring}/V_o=1.5-0.0375We$
Bag	$V_{bag}/V_o=\begin{cases}0.25, & We<30\\ 1-0.025We, & 30<We<40\end{cases}$
Core	$V_{core}/V_o=0.05We-1$
Plume	$V_{plume}/V_o=1-\frac{V_{bag}+V_{ring}+V_{core}}{V_o}$

Table 2: Volume fraction of structures observed during multimode breakup, $We<40$.

The aerodynamic drag coefficients for the bag and the ring are the same as the ones used in the bag breakup regime. The plume has a very low drag coefficient, assumed to be equal to 0.3, the same as wedge-shaped drops, according to [Munson, Young and Okiishi, 1994]. The core drop is assumed to have the same aspect ratio as its parent drop, therefore its aerodynamic drag coefficient will be the same as the one for the parent drop.

STRUCTURE	WEBER NUMBER	BREAKUP TIME t/t^*	DROP SIZE SMD/d_o
Bag	20-30	3	0.02
	30-40	2.5	
Ring	20-30	3.5	0.2
	30-40	3	
Plume	20-80	4	0.2
Core	40-80	$9-0.0375We$	Remaining drop

Table 3: Weber number range and breakup times for multimode breakup.

It is assumed that all structures appear after the initial deformation phase, when secondary breakup starts, according to Eq. (2.16). In Table 3, the breakup times for each one of these structures are given, as well as the range of *We* numbers for which they appear. The average drop sizes resulting from the disintegration are also given, normalized using the initial drop diameter.

4.3.3 Shear Breakup Regime

The shear breakup mechanism is dominant for Weber numbers ranging from 80-800 [Chou, Hsiang and Faeth, 1997]. After the initial deformation phase, the drop disintegration process includes an extensive system of ligaments protruding from the periphery of the parent drop, with numerous individual drops near the downstream end of the ligaments. It has been observed that drop sizes mainly depend on the viscosity rather than on the surface tension of the liquid phase. A boundary layer stripping approach has been adopted here to model this breakup mechanism and the results show very good agreement with observations from isolated drops in shock tubes.

The rate of disintegration is found by integrating over the thickness of the liquid boundary layer to determine the mass flux in the layer and by assuming that this flux leaves the surface of the drop at its equator, as shown in Figure 17 [Ranger and Nicholls, 1969]. A steady-state solution for the velocity profile is sought, both in the air stream and inside the drop, assuming axisymmetric, incompressible flow. Based on these assumptions, the boundary layer momentum integral equations for the gas are:

$$\frac{\partial}{\partial \boldsymbol{x}}\int_0^\infty \boldsymbol{u_G}(\boldsymbol{U}-\boldsymbol{u_G})\boldsymbol{dy}+\frac{\boldsymbol{dU}}{\boldsymbol{dx}}\int_0^\infty (\boldsymbol{U}-\boldsymbol{u_G})\boldsymbol{dy}+\frac{1}{\boldsymbol{r}}\frac{\boldsymbol{dr}}{\boldsymbol{dx}}\int_0^\infty \boldsymbol{u_G}(\boldsymbol{U}-\boldsymbol{u_G})\boldsymbol{dy}=\boldsymbol{\nu_G}\left(\frac{\partial \boldsymbol{u_G}}{\partial \boldsymbol{y}}\right)_{y=0} \tag{4.25}$$

and for the liquid:

$$\frac{\partial}{\partial x}\int_0^\infty u_L^2 dy + \frac{1}{r}\frac{dr}{dx}\int_0^\infty u_L^2 dy = -\nu_L\left(\frac{\partial u_L}{\partial y}\right)_{y=0} - \frac{1}{\rho_L}\frac{dp}{dx}\delta_L \tag{4.26}$$

Equating the shear stress in the gas layer to that in the liquid layer at the interface, yields a third equation:

$$-\mu_L\left(\frac{\partial u_L}{\partial y}\right)_{y=0} = \mu_G\left(\frac{\partial u_G}{\partial y}\right)_{y=0} \quad . \tag{4.27}$$

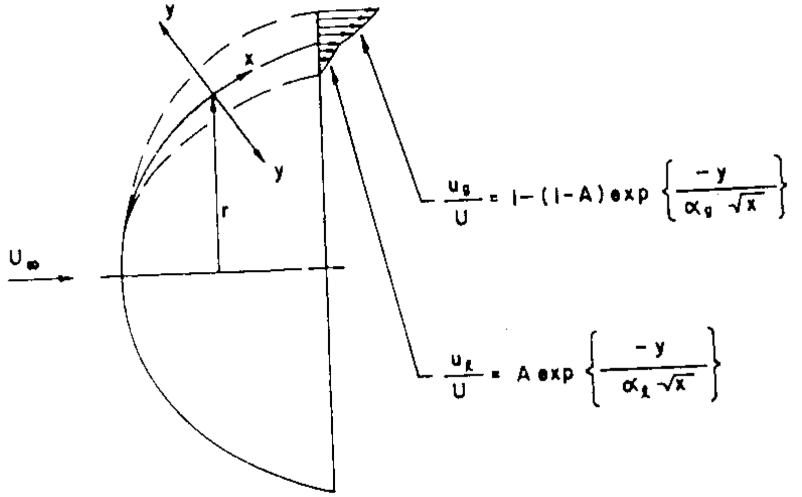

Figure 17: Schematics of Boundary Layer stripping analysis [Ranger and Nicholls, 1969]

The velocity distributions in the liquid and gas phases can be derived using Blasius series analysis [Schlichting, 1968], [Ranger, 1968], [Fishburn, 1974], but this method results in a system of differential equations. Assuming that the drop shape is similar to that of a sphere, it can be shown that at the equator,

$$a_L = \sqrt{\frac{8}{3}\frac{\nu_L}{AU_\infty}}, \qquad A = \left(\frac{\rho_G}{\rho_L}\right)^{2/3}\left(\frac{\nu_G}{\nu_L}\right)^{1/3}. \tag{4.28}$$

The mass of fluid in the circumferential liquid layer being swept along by the gas stream at a distance *x=πD/4* from the stagnation point is:

$$\frac{dm}{dt} = \pi D\rho_L \int_0^\infty u_L dy = \frac{3}{4}(\pi D)^{3/2}\rho_L A a_L U_\infty, \tag{4.29}$$

where U_∞ is the relative velocity of the drop.

The boundary layer stripping mechanism has been evaluated by comparing the mass stripping rate with the correlation given by [Chou et al., 1997]:

$$\dot{m}_p = 0.42\frac{\pi\rho_L d_o^3}{6t^*}e^{\left[0.8\left(t/t^* - 3.5\right)^2\right]}, \quad 1.5 \le t/t^* \le 5.5. \tag{4.30}$$

The correlation provides the mass rate of formation of dispersed drops due to boundary layer stripping and according to Chou et al. it provides a reasonably good fit for the rate of removal of drop liquid from the parent drop, except for the singular points at the beginning and end of the period where drop mass is being removed. In Figure 18 the comparison between the two methods is shown. The conditions used for this comparison include an initial droplet size of 20 μm, velocity of 200 m/s, ambient pressure of 15 bar and surface tension of 0.02 N/m, which results in a Weber number of 600. The comparison shows very good agreement with the correlation for $2.5<t/t^*<4.5$. The dimensionless time here refers to the time from the beginning of the secondary atomization process. It is interesting to note that experimental measurements were available only for this time period and the correlation has been developed based on that.

The disagreement in Figure 18 is found only for early and late timings, where an extrapolation was used to correlate the experimental measurements. The initial conditions of the problem (such as velocity, drop diameter and ambient pressure) have been varied and a wide range of Weber numbers have been tested. The agreement is excellent both for the shear breakup regime (80<We<800), for which the correlation has been originally developed, as well as for the catastrophic breakup regime (800<We).

The diameter of the stripping drops can be estimated by assuming that their size is equal to the Boundary Layer thickness at the point of detachment. Experimental observation from [Chou, Hsiang and Faeth, 1997] reveal that the boundary layer development undergoes a transient phase, shortly after the start of breakup, particularly when the viscosity is low so that the temporal growth rate of the thickness of the boundary layer is relatively slow. In this case the resulting drop size is given by:

$$\boldsymbol{SMD} = 2\sqrt{\boldsymbol{\nu_L t}}, \boldsymbol{t} / \boldsymbol{t_c} < 1 \tag{4.31}$$

where the time, t, in equation (4.31) is the time after the start of breakup and t_c is the time after which the transition is completed, given as:

$$\boldsymbol{t_c} / \boldsymbol{t}^* = 0.002\sqrt{\frac{\boldsymbol{\rho_G}}{\boldsymbol{\rho_L}} \frac{\boldsymbol{u_o d_o}}{\boldsymbol{\nu_L}}}\,. \tag{4.32}$$

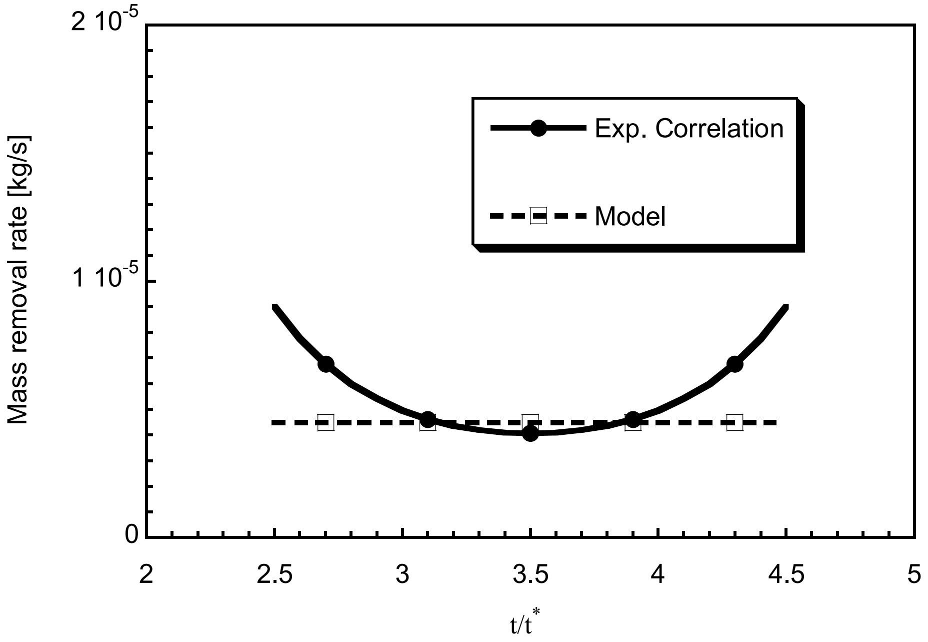

Figure 18: Comparison of Boundary Layer Stripping model with experimental correlation, We=600.

After the transition has been completed, a reasonable estimate for the resulting drop size can be given as:

$$SMD=0.09d_o. \tag{4.33}$$

4.3.4 Catastrophic Breakup Regime

The catastrophic breakup mechanism is typically observed for Weber numbers larger than 800 and has certain similarities with the shear breakup mechanism. A boundary layer stripping mechanism is present, combined with large waves on the surface of the drop. The growth of instability coupled with the drop deformation into a thin disk is sufficient to shatter the parent drop into a cloud of fragments, which are still large compared to the boundary layer thickness. The resulting fragments further disintegrate through the boundary layer stripping mechanism, thus accelerating the drop disintegration into a fine mist of small droplets. These two mechanisms were studied experimentally by [Ranger, 1968]and [Ranger and Nicholls, 1969].

A mechanism for fragmenting the liquid drop is evident in the instability of the drop windward surface that is observed as early as t^*=0.4. Imbalance between applied pressure, inertia and surface tension effects results into instability of the accelerating interface. Wavelengths of these disturbances are large compared to the boundary layer thickness, so their growth is not significantly influenced by the existence of the boundary layer. An instability analysis based on the work done by Fishburn will be presented here to model the drop fragmentation process [Fishburn, 1974]. The process of drop fragmentation combined with the boundary layer stripping mechanism is schematically shown in Figure 19. This approach is different from the KH-RT model proposed by [Patterson and Reitz, 1998], who only consider two different instability mechanisms and the fastest one is selected to model the drop atomization, but do not take into account the stripping from the drop boundaries.

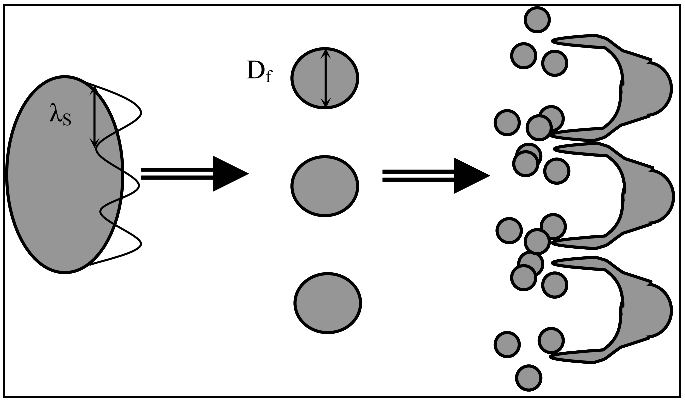

Figure 19: Catastrophic breakup concept

The initial growth rate of a small amplitude sinusoidal disturbance on an accelerating gas-liquid interface is given as [Taylor, 1950]:

$$\eta = \eta_o \exp\left(kG - k^3 \frac{\sigma}{\rho_L} \right)^{1/2} t\,, \tag{4.34}$$

where G is the surface acceleration and k the wavenumber. The surface acceleration can be estimated as:

$$G = 2.2 \frac{\rho_G}{\rho_L} \frac{u_G^2}{D_o}\,. \tag{4.35}$$

The wavenumber $k=k_S$ maximizing the expression

$$kG - k^o \frac{\sigma}{\rho_L} \tag{4.36}$$

is used to calculate the wavelength, $\lambda_S=2\pi/k_S$. The initial amplitude of the disturbance, η_o, is given by:

$$\eta_o = \sqrt{\frac{\nu_L D_o}{2u}} \tag{4.37}$$

The dimensionless time, t/t^*, required for a bubble to penetrate into the liquid drop is assumed to be equal to the drop fragmentation time and is determined from:

$$\boldsymbol{D_o} = \frac{3}{2}\left\{0.2\boldsymbol{\lambda} + 0.33\sqrt{\boldsymbol{G\lambda}}\cdot\boldsymbol{B}\right\}(1+\boldsymbol{bt})^2,$$

$$\boldsymbol{B} = \left[\frac{\boldsymbol{D_o}}{\boldsymbol{u_G}}\sqrt{\frac{\boldsymbol{\rho_L}}{\boldsymbol{\rho_G}}}\boldsymbol{t}^* - \frac{\ln\left(0.2\boldsymbol{\lambda}/\boldsymbol{\eta_o}\right)}{\sqrt{\boldsymbol{kG} - \boldsymbol{k}^3\boldsymbol{\sigma}/\boldsymbol{\rho_L}}}\right] \tag{4.38}$$

if the difference in the square brackets is positive, otherwise:

$$\boldsymbol{D_o} = \frac{2}{3}\boldsymbol{\eta_o}\exp\left[\sqrt{\boldsymbol{kG} - \boldsymbol{k}^3\boldsymbol{\sigma}/\boldsymbol{\rho_L}}\,\frac{\boldsymbol{D_o}}{\boldsymbol{u_G}}\sqrt{\frac{\boldsymbol{\rho_L}}{\boldsymbol{\rho_G}}}\boldsymbol{t}^*\right](1+\boldsymbol{bt})^2 \tag{4.39}$$

where b=1.6, based on [Ranger and Nicholls, 1969]. The diameter of the resulting drop fragments, D_f, is assumed to be equal to the wavelength λ_S. Drop fragments created with this mechanism are subject to boundary layer stripping, as described in the previous section, thus accelerating the disintegration process.

CHAPTER 5

MODEL VALIDATION AND BEHAVIOR IN ENGINE APPLICATIONS

The computational model for the fuel spray atomization has been evaluated by comparing the model predictions with several sets of experimental data, including gasoline and diesel sprays. The gasoline sprays cover the lower spectrum of Weber numbers, typically bag, multimode and to the limit shear breakup, while the diesel sprays extend to the shear and catastrophic breakup regimes. In addition, case studies are presented in this chapter, where the use of the models is demonstrated in realistic engine environments.

5.1 Gasoline Sprays

Fuel sprays used in Gasoline Direct Injection engines are typically generated using High-Pressure Swirl (HPS) injectors or Slit/Fan injectors. Injection pressures range from 4–15 MPa and cylinder pressures from atmospheric, for early injections, to 1 MPa for late injections close to TDC. Depending on the combination of the injection and cylinder pressure, as well as on the primary atomization mechanism, secondary atomization occurs following the bag and multimode breakup mechanisms and in the limit of high injection/cylinder pressures the shear breakup mechanism.

A complete set of data has been acquired at the Spray and Combustion Laboratory of the University of Hiroshima using Mie Scattering, PIV and Holography techniques to characterize a High-Pressure Swirl Injector, provided by Mitsubishi Electric Company.

The measurements have been obtained in an optical static cell, with size 10×10×10 cm and a non-evaporating dry solvent was used as fuel. The ambient gas was Nitrogen (N_2). The injector has 6 tangential slots and a nominal spray cone angle of 50^o at atmospheric pressure. A schematic of the injector geometry is given in Figure 20. The experimental conditions are given in Table 4 and the fuel properties, compared to the properties of commercial gasoline, in Table 5.

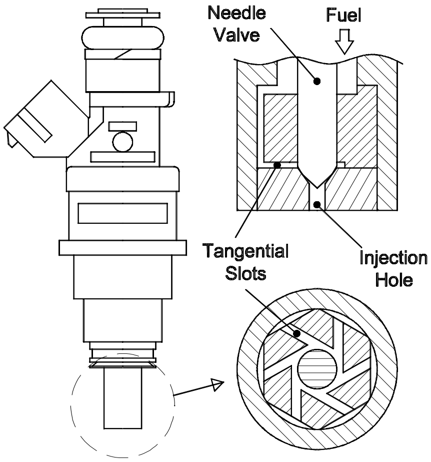

Figure 20: High-Pressure Swirl Injector characterized at the University of Hiroshima.

Nozzle	**Type**	High-Pressure Swirl Injector
	Number of Tangential Slots	6
Cone Angle [deg.]		50 at atm. pressure
Injection Pressure [MPa]		5
Injection Duration [ms]		1.25
Injection Quantity [mg/inj.]		7.24
Ambient Temperature [K]		293
Ambient Pressure [MPa]		0.1, 0.4

Table 4: Injector specifications and experimental conditions.

The data were acquired both for 0.1 and 0.4 MPa ambient pressure and include spray tomograms (using a PIV system) and Mie-scattering images, acquired with a high-speed (up to 20,000 frames/second) digital camera, as well as SMD versus time at various locations downstream of the injector using a Laser Drop Sizing Analyzer (LDSA). Also, measurements especially focused on the pre-spray have been performed and the individual droplet sizes have been measured using holography. The 2-D PIV system specifications are given in Table 6.

Comparison of Fuel Properties			
Property	**Gasoline**	**Dry Solvent**	**$n\text{-}C_8H_{18}$**
Density [kg/m^3]	745	770	702.67
Kin. Viscosity [mm^2/s]	2.25	1.032	0.926
Surface Tension [N/m]	2.25×10^{-2}	2.45×10^{-2}	2.207×10^{-2}
Flash Point [K]	230	443	286

Table 5: Dry solvent properties compared to commercial gasoline.

Item	2-D PIV
Laser type	TSI Y25-20E
Wavelength	532 nm
Laser energy	25 mJ
Laser pulse duration	5 ns
Laser sheet thickness	1 mm
CCD camera	TSI PIVCAM 10-30
CCD pixel	1008x1018 pixels

Table 6: Specifications of 2-D PIV System.

For the computations in KIVA a grid spacing of 2.5 mm has been used and 5,000 computational parcels have been initially injected. Isooctane ($n\text{-}C_8H_{18}$) has been used as a fuel in the computations, with properties slightly different than the ones of the dry-solvent used in the experiments.

Typical breakup lengths for liquid sheets are on the order of 1-2 mm downstream of the nozzle exit. In this region, the spray is very dense and accurate experimental data cannot be acquired with conventional laser techniques. While a promising time-resolved x-radiography method for visualizing and measuring dense sprays has been recently developed at the Argonne National Laboratory [Yue et al., 2002, Powel et al., 2002], data for validation of liquid sheet formation in HPS injector sprays are not readily available. Consequently, the spray model can only be validated based on data collected far downstream (at least 20-25 mm downstream the orifice). However, in these downstream locations, other phenomena, such as secondary atomization, evaporation, air entrainment and potentially collisions between droplets take place and affect the spray shape and droplet sizes. Nevertheless, useful conclusions can be extracted from qualitative comparisons of the development of the overall spray structure, as well as from quantitative comparison of spray tip penetration and droplet sizes at such downstream locations.

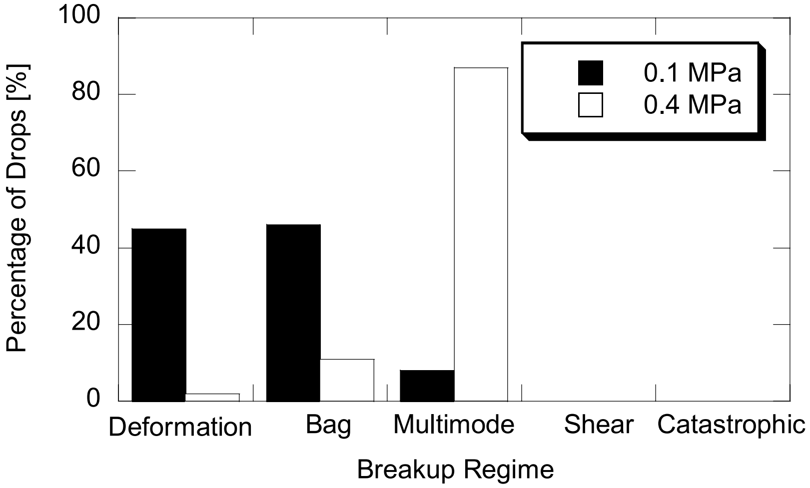

Figure 21: Secondary atomization mechanisms encountered in typical gasoline sprays

The secondary atomization mechanisms encountered are shown in Figure 21. When the ambient pressure is low the majority of droplets has Weber number less than 20, therefore it undergoes deformation without further disintegrating or it breaks up according to the bag breakup mechanism. When the ambient pressure increases the Weber number also increases and most of the droplets are found in the multimode breakup regime. It is expected that for higher injection or ambient pressures a number of droplets will be in the shear breakup regime.

5.1.1 Injection under P_{amb}=0.1 MPa

A qualitative comparison of the observed and predicted spray structure is presented in Figure 22, where five different snapshots are shown at 0.1 ms intervals from 0.1 ms to 1.0 ms after the Start Of Injection (SOI). Both experimental and CFD images represent a domain of 7.2×7.2 cm. The left part of each image shows a spray tomogram, obtained with the Mie-scattering technique. On the right hand side, the discrete computational parcels used in the numerical simulations are shown.

At 0.1 ms and 0.2 ms after SOI, a very dense spray with small cone angle can be seen. At this early timing, the main spray has not started forming yet. At 0.4 ms after SOI, the main spray is fully developed and the pre-spray can be easily distinguished from the main spray. At 1.0 ms, both parts of the spray are still noticeable but the model tends to overpredict the pre-spray. An interesting observation is that the distance between the pre- and the main spray has now increased and that the size of the pre-spray has decreased. Also, a recirculation region appears for the first time after 0.7 ms close to the bottom of the main spray. This is driven by the vortices that are illustrated clearly with the aid of velocity plots, shown in Figure 23.

0.1 ms		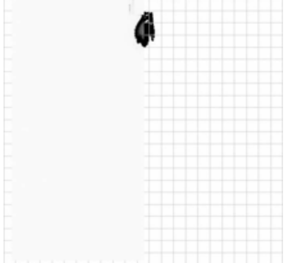	0.2 ms
0.3 ms	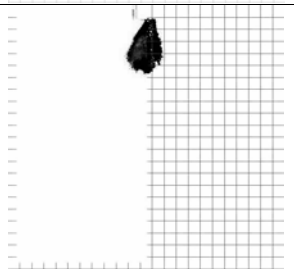	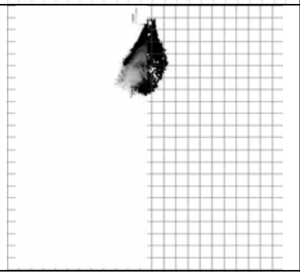	0.4 ms
0.5 ms	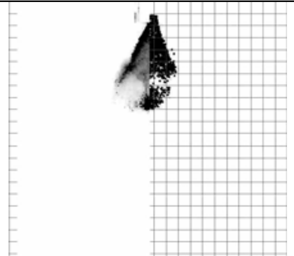	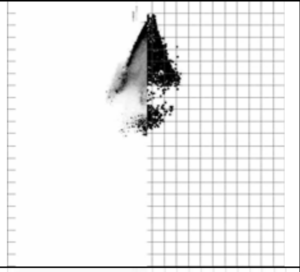	0.6 ms
0.7 ms	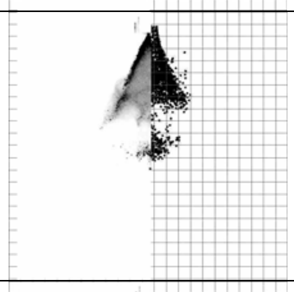	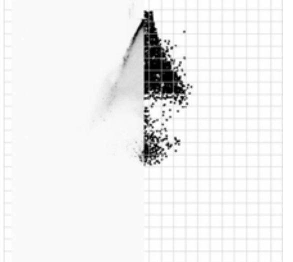	0.8 ms
0.9 ms	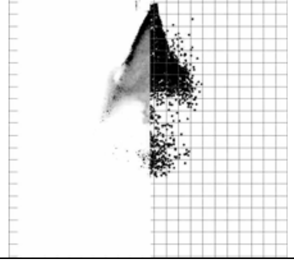	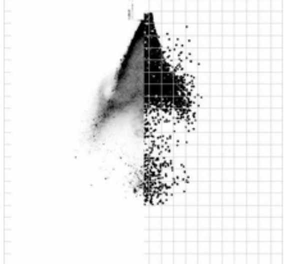	1.0 ms

Figure 22: Comparison of spray tomograms (left) with KIVA-3V computational parcels (right) at various instants, under ambient pressure (0.1 MPa), T=293 K

Overall, the snapshots shown in Figure 22 indicate reasonably good predictions of both the pre-spray and the main spray features. For late timings, where the pre-spray has moved farther away from the main spray, it appears that the model can only predict correctly the main spray structure. This is probably due to the primary atomization mechanism for the pre-spray, which fails to predict the correct droplet size and breakup regimes for the droplets comprising the pre-spray.

Figure 23 compares PIV-LIF measured and KIVA-3V predicted ambient air vector plots at 0.8 ms, 1.3 ms and 1.8 ms after the SOI. On the left hand side of the images, the experimental results are shown and on the right hand side the numerical ones, both within a domain of 75×40 mm. From a qualitative point of view, predictions are in very good agreement with measurements. In particular, the same vortex patterns are observed, driving the recirculation of spray droplets near the spray boundary. In addition, the predicted center of the vortex patterns appears to correlate well with velocity measurements for early instants. However, later on, it appears that the predicted center of vortex activity trails behind the location of the observed one.

In Figure 24 the comparison between the experimentally measured and the CFD-predicted tip penetration is shown. The agreement is very good both for the pre- and the main spray and only in late timings the model tends to overpredict the penetration of the pre-spray.

More insight on the behavior of the model can be gained if the calculated SMD is compared to the experimental measurements at two planes located 27 mm and 36 mm downstream of the injector, as shown in Figure 25. In order to ensure the presence of a large enough number of computational parcels at a given plane to produce statistically meaningful SMD results, the sampling was done within planes located ±2 mm of the specified location. Inspection of Figure 25 reveals that while the SMD predictions agree very well with measurements for early and late timings, the droplet sizes are strongly underestimated for intermediate timings. This discrepancy is attributed to the uncertainties and simplifications that were made in the development of the bag breakup model. As a result of these simplifications, the end of breakup time in the model may be somewhat lower than in the experiment and this is causing the droplet size to be reduced faster.

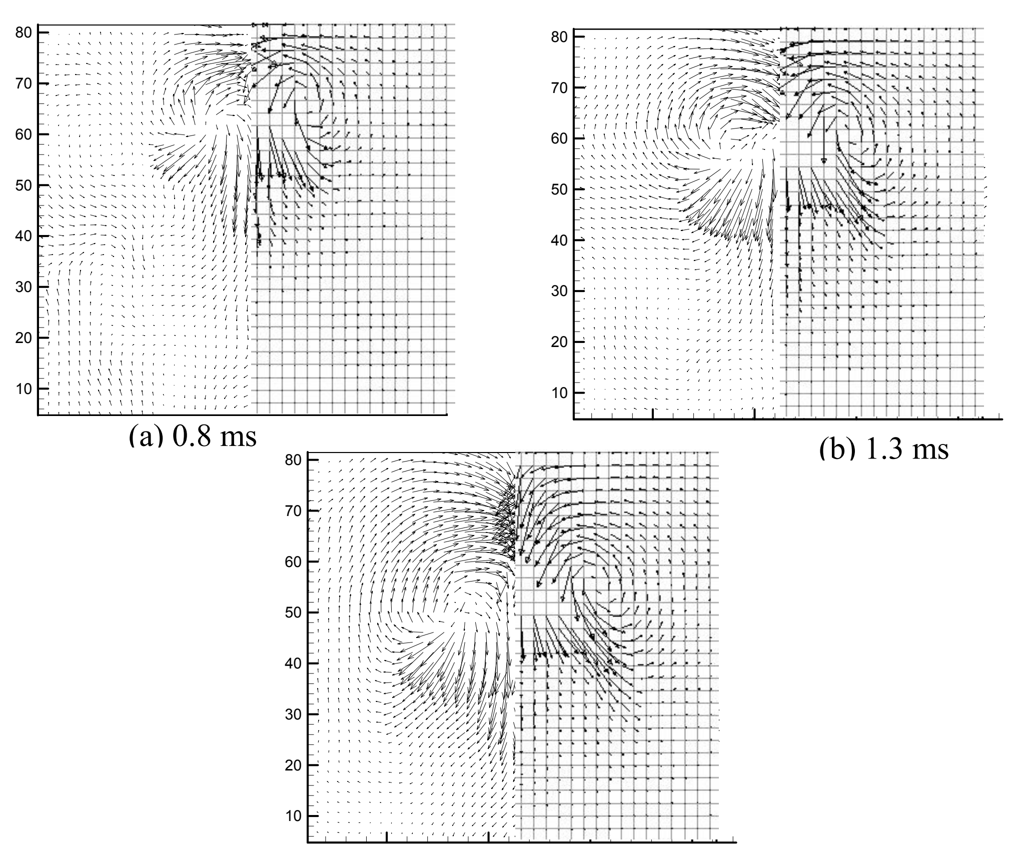

(a) 0.8 ms

(b) 1.3 ms

Figure 23: Comparison of PIV-LIF measured and KIVA-3V predicted velocity vectors at (a) 0.8 ms, (b) 1.3 ms and (c) 1.8 ms after SOI

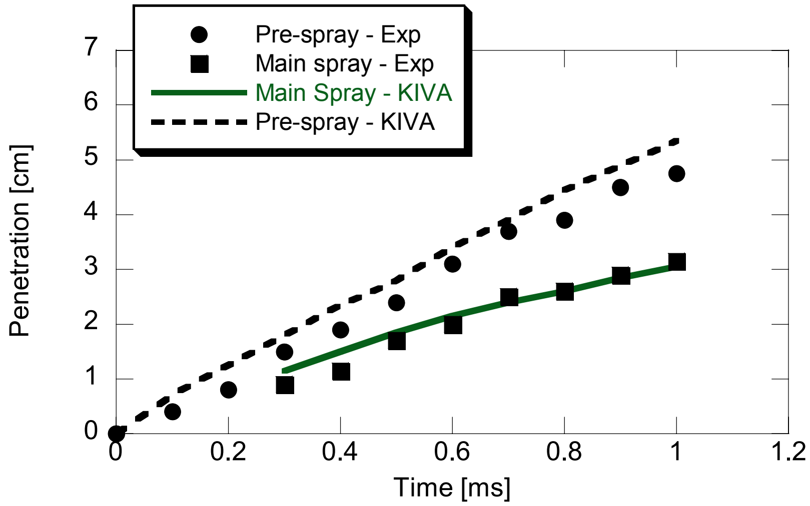

Figure 24: Experimental vs. CFD-predicted tip penetration for P_{amb}=0.1 MPa

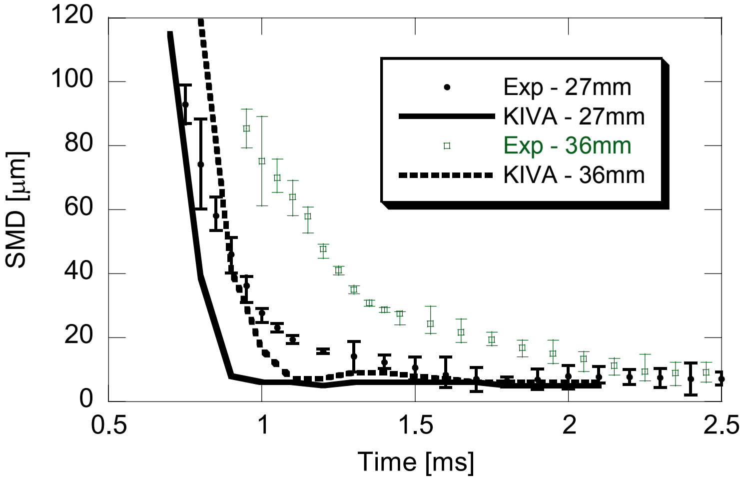

Figure 25: SMD versus time for ambient pressure 0.1 MPa

5.1.2 Injection under P_{amb}=0.4 MPa

Additional runs have been performed for injection under ambient pressure of 0.4 MPa, which corresponds to relatively late injection timings in order to create a stratified mixture in a GDI engine. In Figure 26 the measured and predicted tip penetrations of the pre- and the main spray are plotted against time, showing good agreement between the model and the experiments, even though the predicted penetrations are always slightly overpredicted.

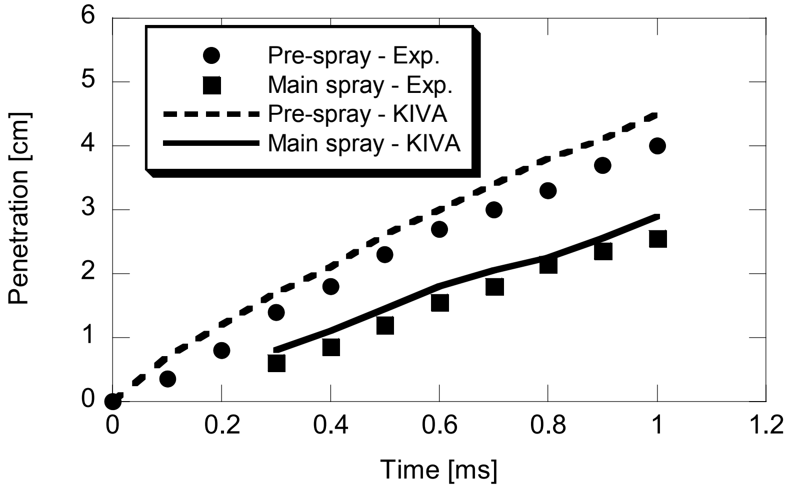

Figure 26: Experimental vs. CFD-predicted tip penetration for P_{amb}=0.4 MPa

The structure of the fuel spray is shown in Figure 27, where both experimental images and CFD predictions are presented. The comparison is very good until 0.7 ms after SOI. For later timings a slight difference appears at the recirculation area, which is significantly higher in the CFD results. Also the curvature of the predicted spray is different than the one observed in the experiments.

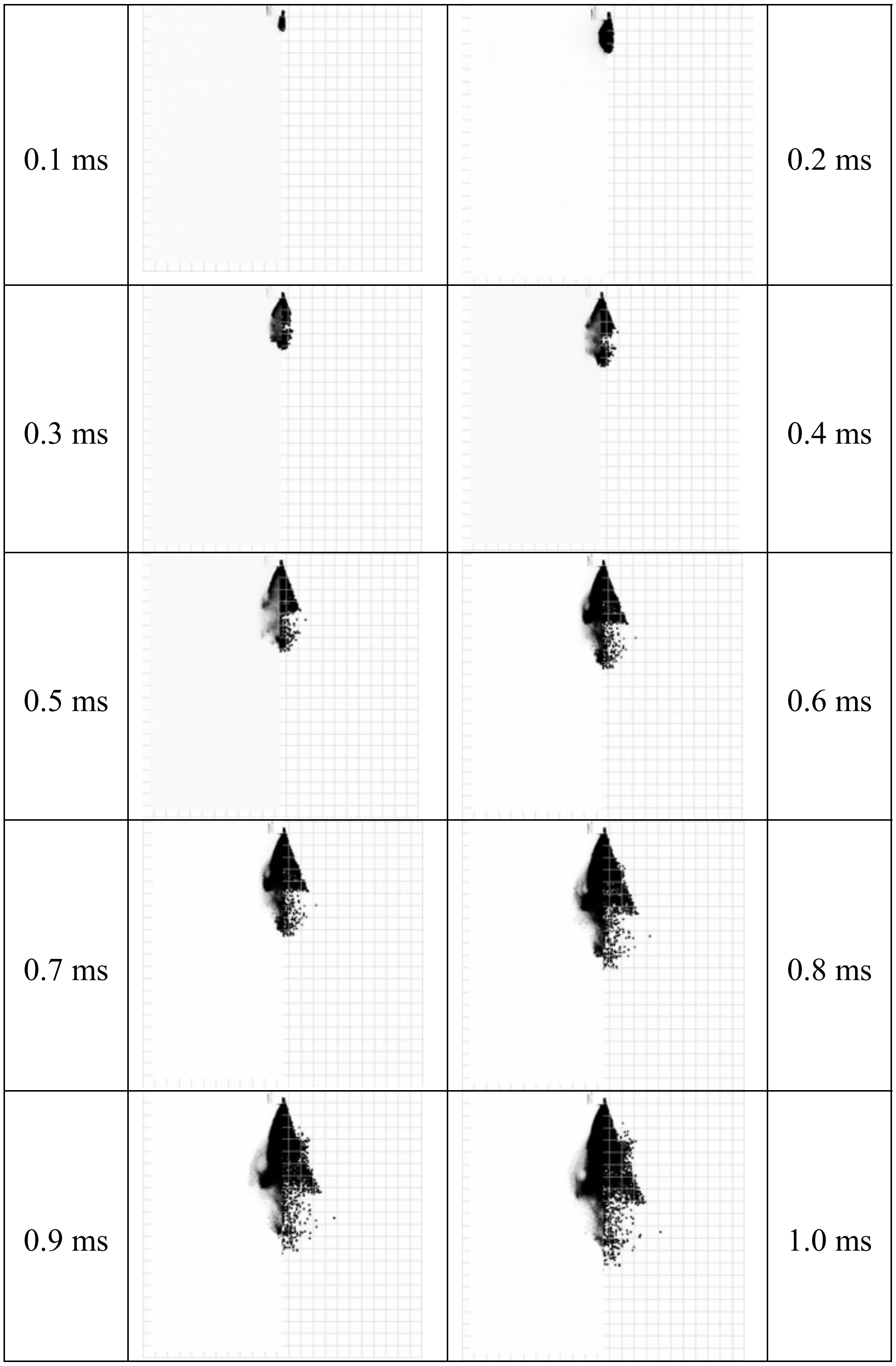

Figure 27: Comparison of spray tomograms (left) with KIVA-3V computational parcels (right) at various instants, under ambient pressure 0.4 MPa

The droplet size comparison is given in Figure 28. The SMD measurements were obtained in two planes, 22mm and 28mm downstream of the nozzle, and the CFD sampling was done within planes located ±2 mm of the specified location. In this case it appears that there is a very good agreement between the experiment and the model, even though at late timings the model tends to underpredict the final size of the drop sizes. However, the rate of change of the drop diameter seems to be very close to the experimental one.

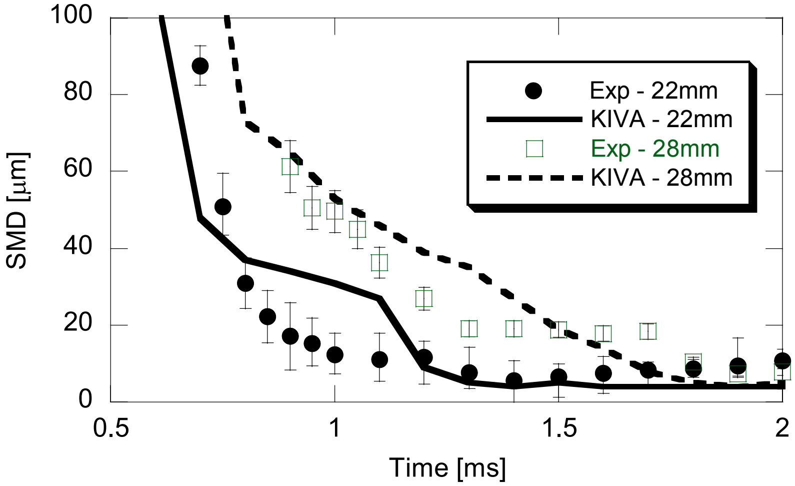

Figure 28: SMD versus time for ambient pressure 0.4 MPa

These results demonstrate substantial improvement over previous efforts to capture the spray characteristics for injections under elevated ambient pressures. In [Chryssakis et al., 2003], the penetration of the main spray was strongly underpredicted when the TAB model was used for the secondary atomization, as illustrated in Figure 29. It is believed that this is due to the higher Weber numbers, resulting in drop atomization according to the multimode and shear breakup mechanisms, while the TAB model has been found to perform well only for low Weber numbers (see Chapter 3).

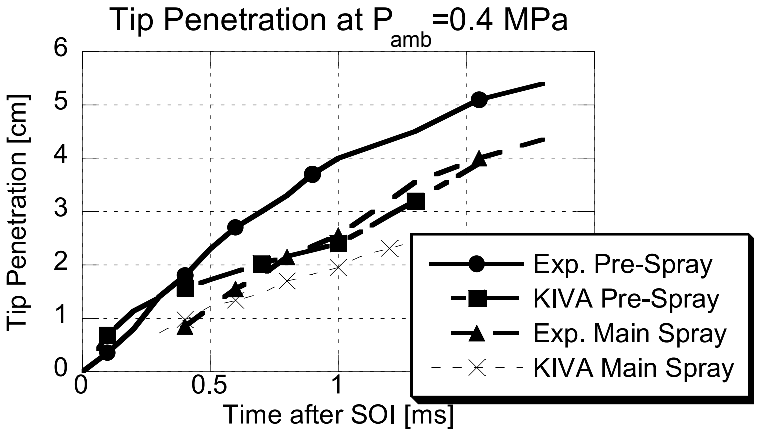

Figure 29: Tip penetration using the TAB model for secondary atomization [Chryssakis et al., 2003]

5.2 Diesel Sprays

Two sets of experimental data are used in order to evaluate the model performance for diesel sprays. The first one consists of measurements by Habchi et. al., [1997], performed at the Institut Français du Pétrole (IFP) and the second one of measurements obtained in the Korea Advanced Institute of Science and Technology (KAIST). The first set of data includes fuel injection under three different injection pressures and measurements of liquid and vapor penetration of the fuel spray. The KAIST data include two different ambient and injection pressure conditions and the measurements consist of spray penetration, cone angle and droplet size observations.

5.2.1 Comparison Against IFP Measurements

The experimental data of [Habchi et al., 1997] have been used as a first step towards evaluating the model for typical diesel spray conditions. Their experimental apparatus consists of a high-pressure, high-temperature, constant volume cell. The injector used is a common rail unit with electronic control that can supply fuel pressure of 20-150 MPa. The injector was fitted with a single-hole tip with the hole on the axis of the injector. Spray penetrations for three different injection pressures were measured with a Mie scattering technique.

The computational grid consists of a constant volume bomb with dimensions 10.5×10.5×10.5 cm. The grid, shown in Figure 30, is finer in the upper third and in the center of the bomb, where the cell size is $\Delta x = \Delta y = \Delta z = 1$ mm.

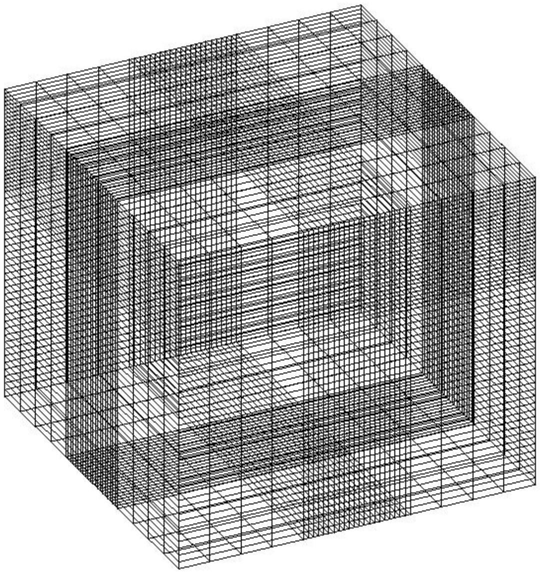

Figure 30: Computational grid for the diesel spray simulations

The secondary atomization mechanisms encountered in this calculation are shown in Figure 31. For the 40 MPa injection pressure 40% of the drops are in the shear breakup regime and 60% atomize according to the catastrophic breakup mechanism. As the injection pressure increases, the number of drops in the catastrophic breakup regime increases, while the shear breakup mechanism becomes less significant. This can be explained due to the higher injection velocity in higher injection pressures, which leads to higher Weber numbers, corresponding to the catastrophic mechanism (*We*>800).

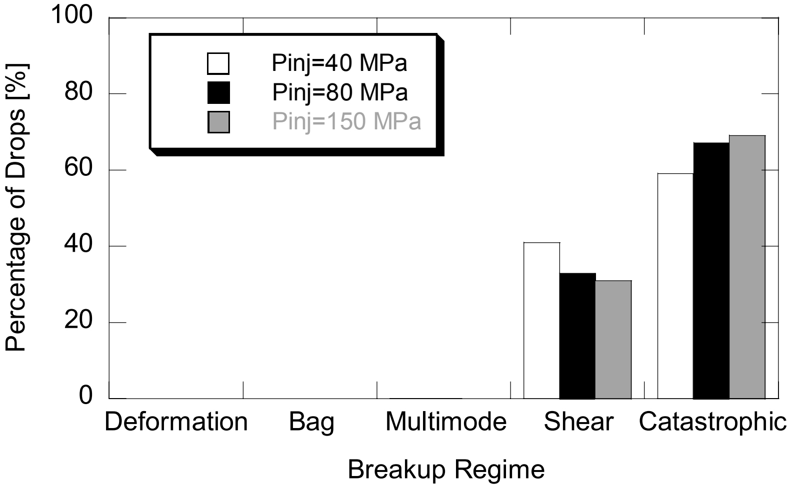

Figure 31: Secondary atomization regimes for IFP data, CFD predictions

In Figure 32 a comparison of spray tip penetration for injection pressures of 40, 80 and 150 MPa is shown, with very good agreement with experimental measurements. The ambient pressure was set to 3 MPa and the temperature to 400K. The model was initialized by injecting blobs with diameter equal to the nozzle diameter (200μm), in order to represent the liquid core of the spray. The constant k_1, controlling the primary breakup rate, was set to 0.5 in order to obtain an atomization rate that results in spray tip penetration in agreement with the experimental measurements. This value has been held constant throughout the injection pressure sweep, showing that the tip penetration scales with injection pressure.

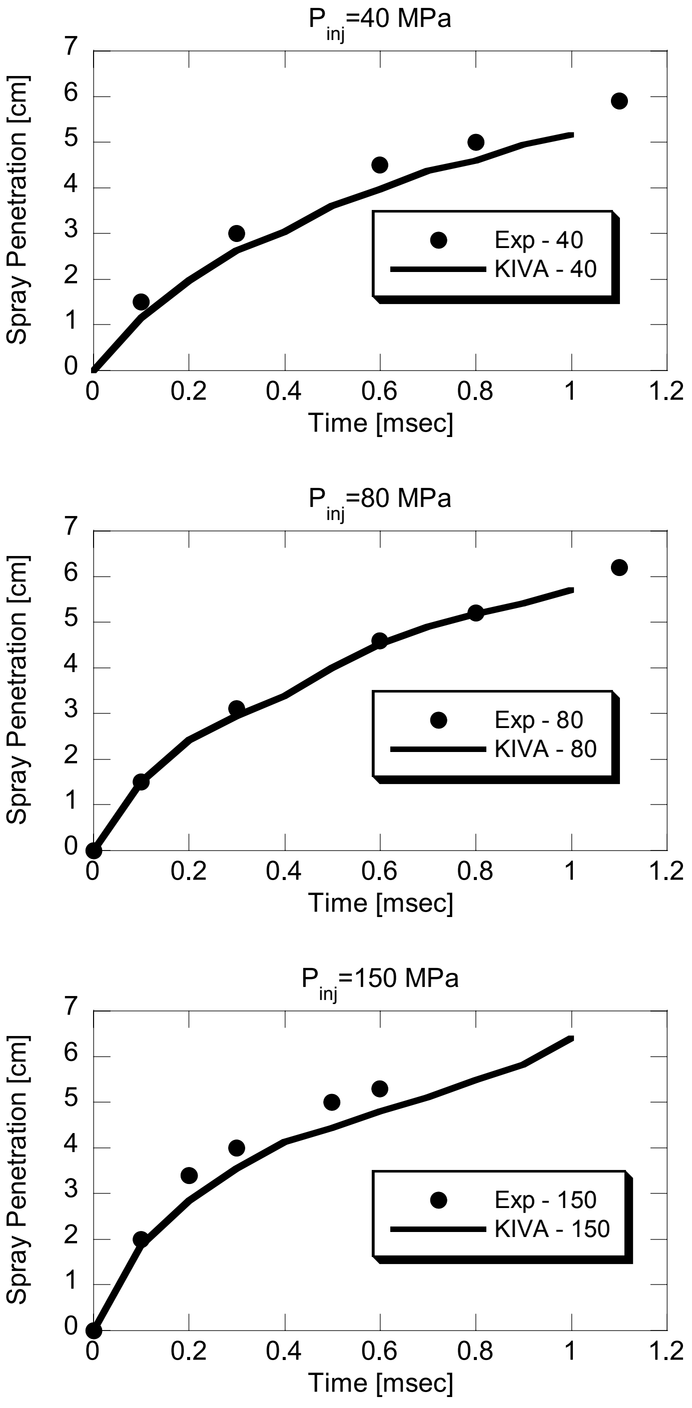

Figure 32: Experimental and CFD-predicted tip penetration for P_{inj}=40, 80, 150 MPa

5.2.2 Comparison Against KAIST Measurements

The experimental setup consists of a cylindrical constant-volume chamber. The chamber has three optical windows and a wall thickness of 40mm. The inner length of the chamber is 250 mm and the inner diameter 260mm, resulting in a volume of 0.01327 m^3. The injector used is a BOSCH fuel injector, with a VCO nozzle. The geometrical characteristics of the nozzle are given in Table 7.

Hole Diameter	0.144 mm
Hole Cross-sectional Area	1.6286×10^{-4} cm^2
Number of Holes	5
Injection Angle	152^o
Hole Length	1.133 mm

Table 7: Geometrical characteristics of the nozzle, KAIST data

For the measurements diesel fuel with density of 840 kg/m^3 was injected in the chamber, which was filled with N_2. The chamber temperature was kept constant at 300 K. Three different combinations of injection and chamber pressure were examined, as summarized in Table 8. Detailed velocity profiles, as well as rail pressure profiles, are measured experimentally, as shown in Figure 33.

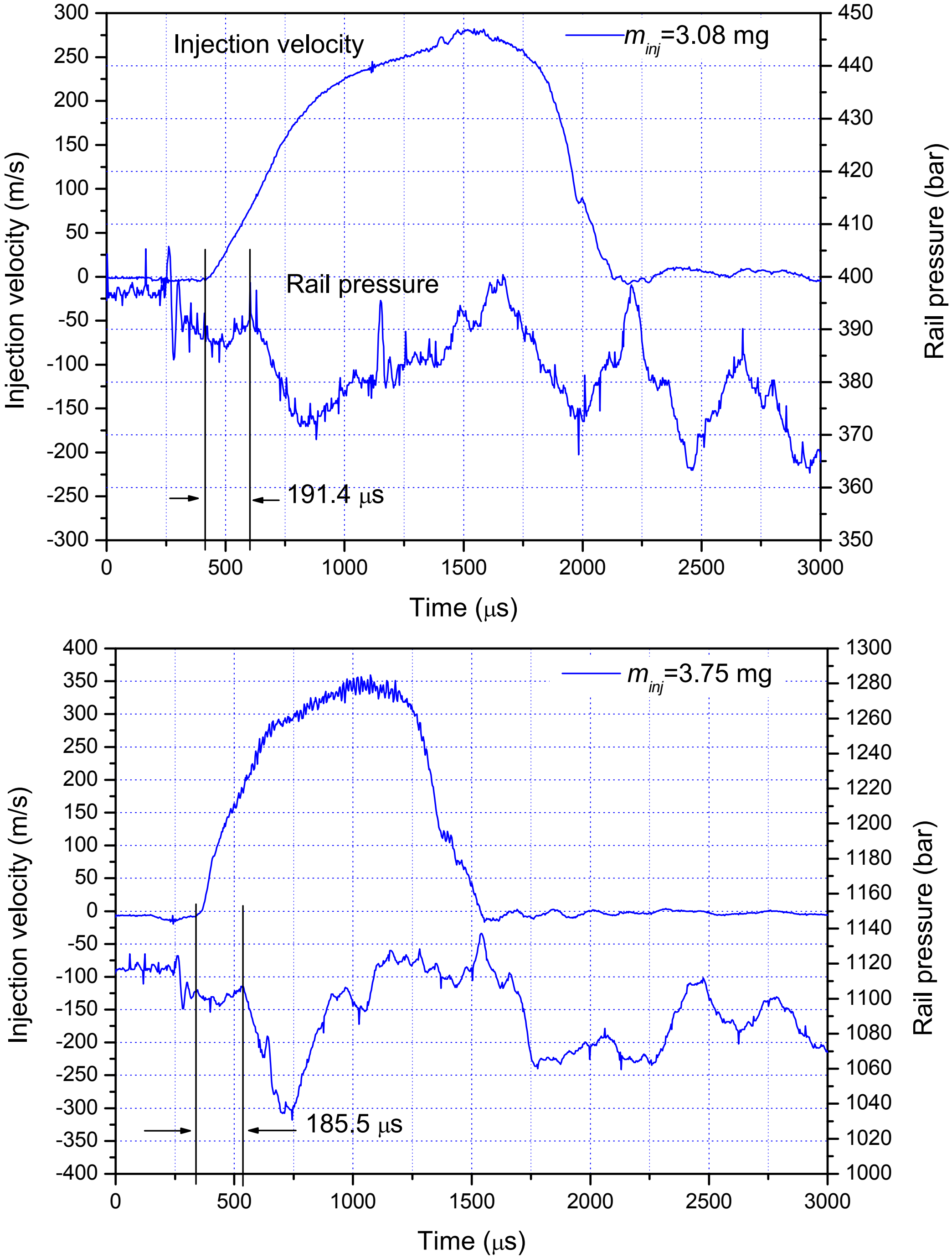

Figure 33: Injection velocity and rail pressure profiles, KAIST measurements.

	P_{inj} [MPa]	P_{amb} [MPa]	Mass [mg]	Inj. Dur. [ms]	Cone Angle [°]
1	39.5	0.1	15.4/5=3.08	1.7	7
2	112	0.1	18.75/5=3.75	1.2	8
3	112	3.0	18.75/5=3.75	1.2	10

Table 8: List of experimental conditions, KAIST data

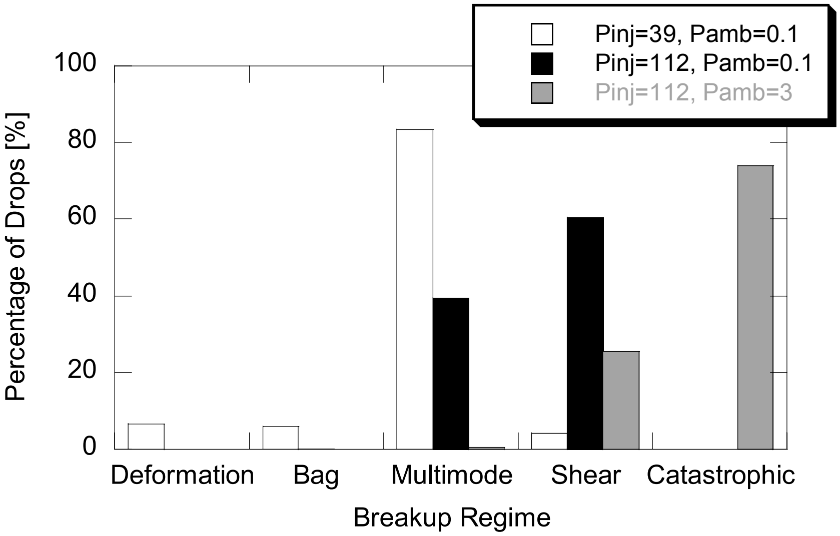

Figure 34: Secondary Atomization Regimes, KAIST data

The secondary breakup regimes for the droplets produced as a result of primary atomization are shown in Figure 34. In the low injection pressure-low ambient pressure case (P_{inj}=39 MPa, P_{amb}=0.1 MPa) the majority of the droplets is found in the multimode breakup regime and approximately 10% are in the deformation and bag breakup regimes. These very low Weber numbers are the result of the initially low injection velocities at the start of injection (see Figure 33). As the injection pressure increases to 112 MPa but the ambient pressure stays low 40% of the drops disintegrate according to the multimode breakup mechanism and the remaining 60% according to shear breakup. When the ambient pressure is increased to 3 MPa the majority of the droplets falls in the catastrophic breakup regime with only 30% in the shear breakup.

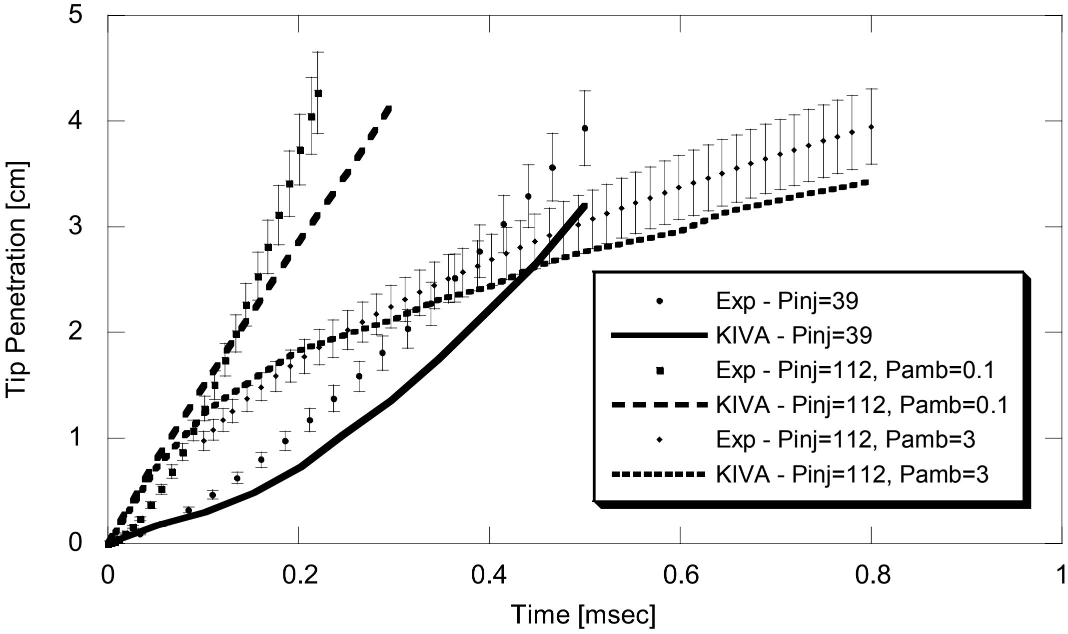

Figure 35: Experimental and CFD-predictions for Tip Penetration, KAIST data

The spray tip penetration for the three cases considered here is plotted in Figure 35. The model tends to underpredict the tip penetration but it can consistently capture the correct trend, even though the cases tested cover a wide range of ambient and injection pressures. It should be noted here that the experimental values for tip penetration are averaged over the 5 jets emerging from a typical 5-hole nozzle. In Figure 36 a typical image illustrates the asymmetries that can exist between the jets. It is believed that using different values for the constant K_c, which takes into account losses in the contraction corner could result in predictions much closer to the experimental averages. However the appropriate value based on geometry is not known for the tested nozzle and an average value of 0.45 has been used, as in the previous case of the IFP data.

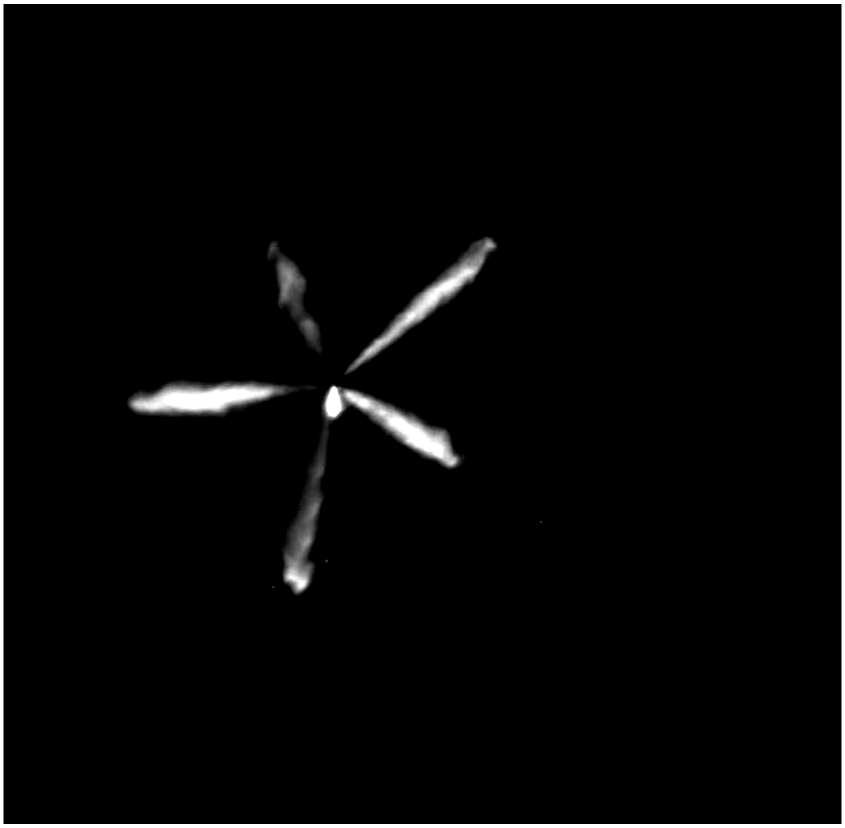

Figure 36: Experimental image of typical diesel sprays from a 5-hole nozzle

The predicted spray structure for all three cases is shown in Figure 37, illustrating the differences in tip penetration and spray development for each condition. In the low injection case the tip penetration is initially increasing slowly due to very low injection speeds but eventually it becomes faster, since the ambient pressure is low and there is no significant aerodynamic resistance. On the other hand, in the high injection pressure-high ambient pressure case, the spray development is initially faster due to higher injection velocities, but it slows down when the aerodynamic drag effects become important. The asymmetries observed in Figure 37, especially in the second column, are due to the turbulence modeling in the primary atomization, which introduces a distribution of breakup lengths. In addition, the injection velocity profile (measured in the experiments) enhances the asymmetry because the drops are injected with varying injection velocities, resulting in a range of predictions for the primary breakup length of each computational parcel.

The first two columns in Figure 37 (low ambient pressure) correspond to early injections, which can be used to achieve Homogeneous Charge Compression Ignition (HCCI) or partially homogeneous diesel combustion. Figure 37 demonstrates that the low injection pressure has the advantage of slow spray development and limited tip penetration, compared to the high injection pressure case. This can lead to reduced wall impingement and wall-film formation. The third column corresponds to conventional diesel combustion, where the fuel injection takes place late in the cycle, when the cylinder pressure is already high. The tip penetration is comparable to the one from the low injection pressure-low ambient pressure combination.

In addition to spray penetration, the droplet size has been measured for injection pressure 39 MPa and 112 MPa under ambient pressure of 0.1 MPa. The results of this comparison are given in Figure 38 for 39 MPa and in Figure 39 for 112 MPa, as a function of time. The measurements were taken at two planes perpendicular to the injection axis, one at $169d_o$ and one at $279d_o$, corresponding to 24 mm and 39 mm from the nozzle, respectively. Here only the averages for each injection pressure are shown, since the individual values at both planes were very close to each other.

	P_{inj}=39 MPa	**P_{inj}=112 MPa,** **P_{amb}=0.1 MPa**	**P_{inj}=112 MPa,** **P_{amb}=3.0 MPa**
0.2 ms	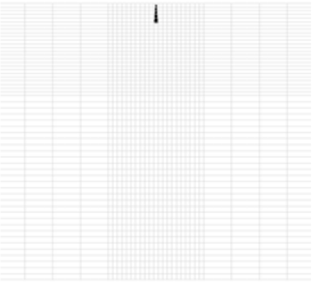	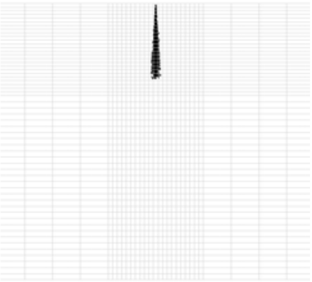	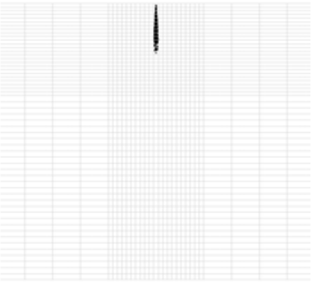
0.3 ms	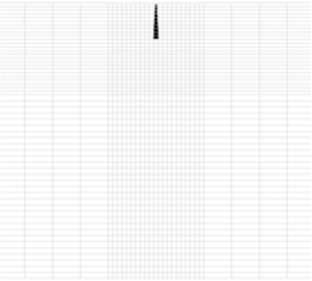	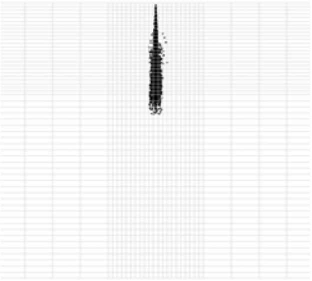	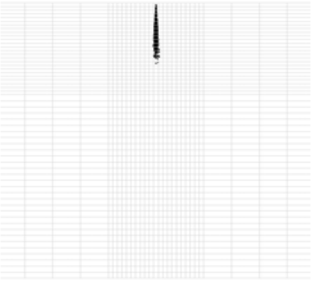
0.4 ms	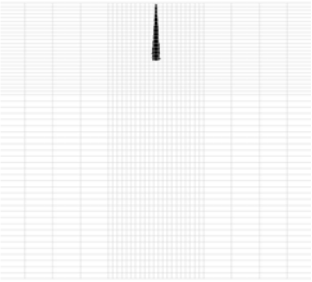	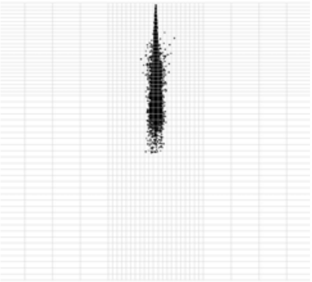	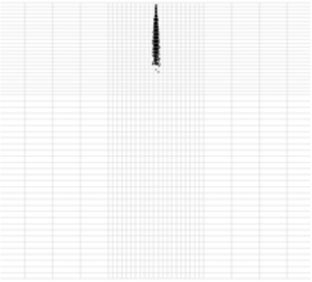
0.5 ms	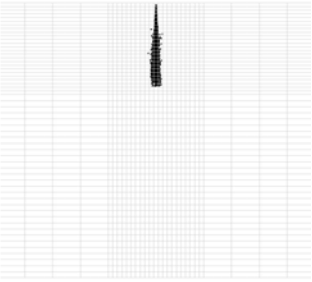	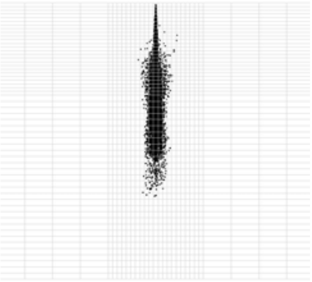	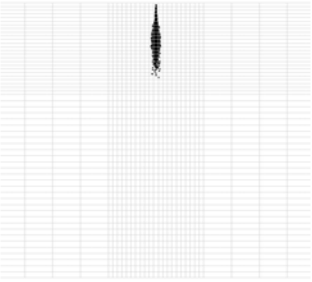

Figure 37: CFD predictions of spray structure, KAIST data

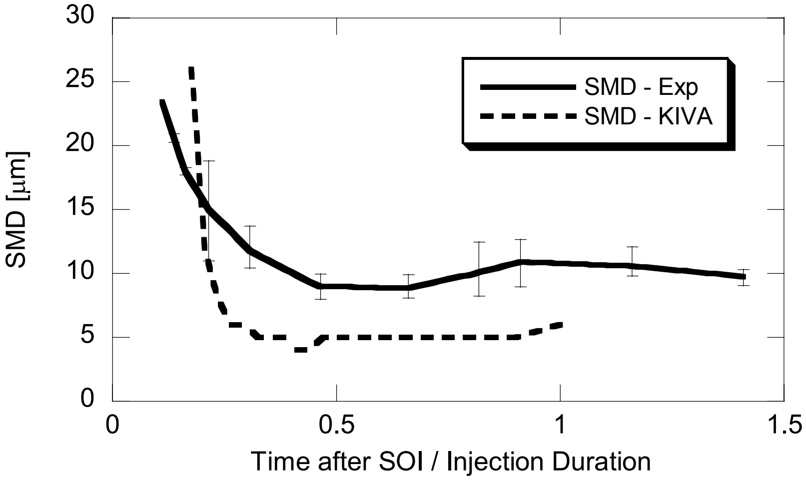

Figure 38: Drop size measurements and comparison with CFD predictions, P_{inj}=39 MPa

In Figure 38 the comparison for the injection pressure of 39 MPa is presented. The initial predicted droplet size is similar to the experimental measurements but the rate of disintegration appears to be much stronger in the model therefore leading to a fast reduction in drop size. It is also obvious that the final drop size is smaller than the measured one. The comparison for the injection pressure of 112 MPa is shown in Figure 39 and in this case the agreement with the experiment is very good. There is only a difference in the initial droplet size. It can be argued that this could be partially due to the fact that some large drops undergoing primary atomization are included in the SMD calculation in the model, hence artificially increasing the predicted drop size. The rate of decrease of the drop diameter is very similar to the experimental one, as well as the final droplet size predicted by the model.

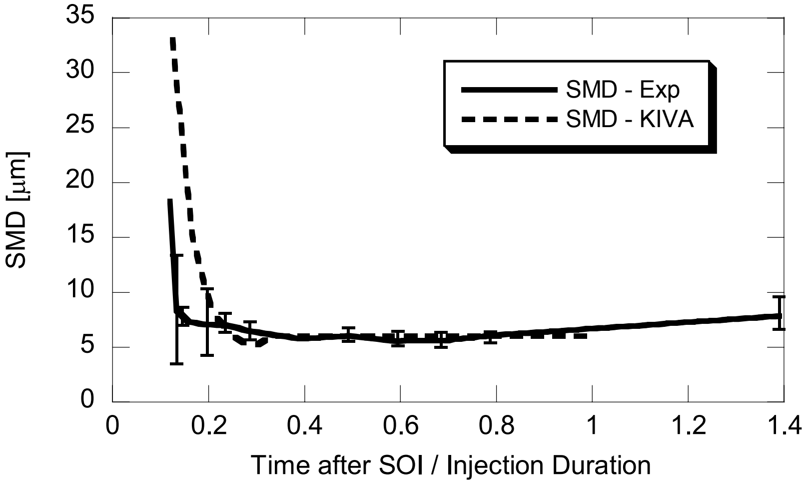

Figure 39: Drop size measurements and comparison with CFD predictions, P_{inj}=112 MPa

5.3 Engine Applications

In addition to the model validation shown in the previous section, two cases demonstrating the capabilities of the model in realistic engine conditions are presented here. They include both a direct-injected optical engine and a small bore diesel engine with an early and a late injection, illustrating the wide range of breakup regimes that have to be modeled, depending on engine operating conditions.

5.3.1 Gasoline Direct Injection Engine

In order to demonstrate the capabilities of the spray model in modeling fuel sprays in GDI engines, a relatively late injection strategy case has been tested, based on the optical engine used at the University of Michigan [Vanzieleghem, 2004, Vanzieleghem et al., 2004, Fissenewert, 1999, Ponti, 2002]. The total mass of 10 mg of iso-octane (C_8H_{18}) has been injected at 67° bTDC with an injection duration of 7° CA, corresponding to an injection pressure of 8.5 MPa. The cylinder pressure during injection ranges from 0.14-0.17 MPa. This operating condition is used here to illustrate a typical injection in GDI engines to create a mixture that is stoichiometric around the spark plug and relatively homogeneous in the remaining cylinder space. An illustration of the fuel spray inside the cylinder is given in Figure 40. The pre-swirl spray can be clearly distinguished from the main spray, penetrating faster and impinging on the piston surface first.

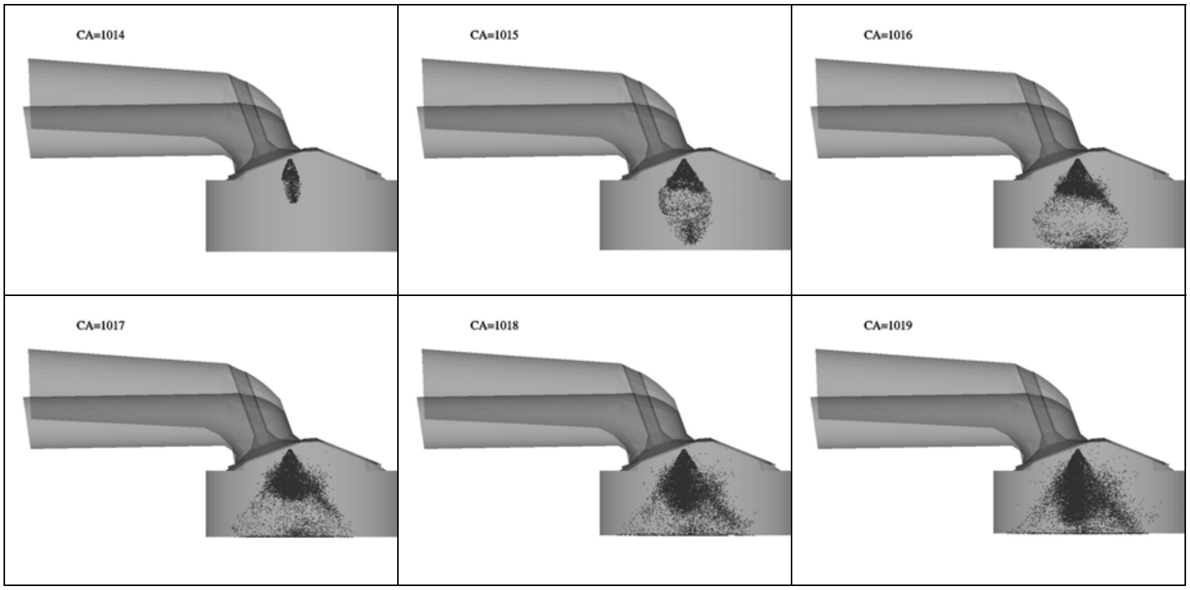

Figure 40: Fuel spray evolution of a typical injection in a GDI engine, SOI=67º bTDC

In Figure 41 the secondary atomization mechanisms for the droplets after primary breakup are shown. The majority of the drops disintegrates based on the multimode breakup mechanism, while approximately 20% fall into the bag breakup regime and 15% have very low Weber numbers and only deform without breaking up. In addition, about 1.5% of the drops is in the shear breakup regime, most likely drops from the pre-swirl spray. Depending on the injection strategy, an earlier injection could be used to achieve a very homogeneous mixture. In this case, the cylinder pressure during injection would be lower and a larger amount of drops would be in the bag and deformation regimes. On the other hand, if a later injection is employed to enhance the mixture stratification, more drops are expected to be found in the shear breakup regime.

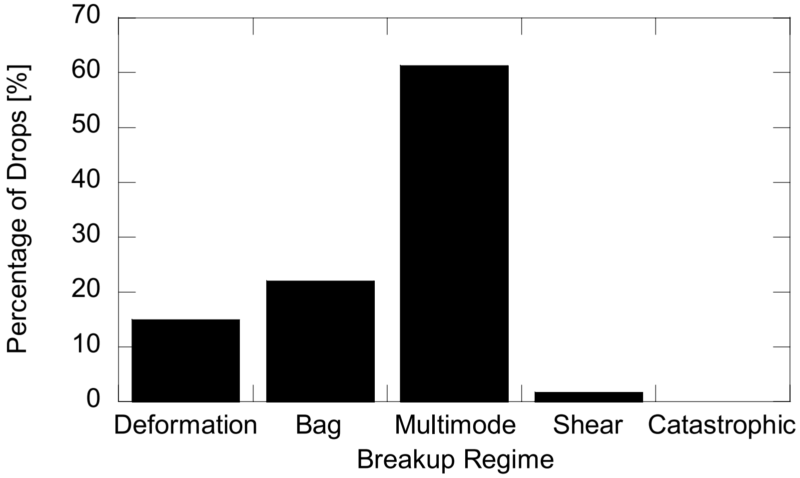

Figure 41: Secondary breakup mechanisms for the two injections of a typical split injection in a GDI engine

A comparison with Mie Scattering measurements obtained by Ponti [2002] for similar conditions has also been performed in order to demonstrate the capability of the model to capture the spray structure in a realistic engine environment. In this case the fuel injection starts at 72° bTDC and the injection duration is 24° CA, corresponding to an injection pressure of 5 MPa. The comparison with the Mie Scattering measurements has been done by creating a new variable in KIVA, defined as:

$$parmie=\Sigma[n \bullet r^2] \tag{5.1}$$

where *n* is the number of droplets and *r* their diameter. This variable reproduces the effect observed in Mie Scattering experiments, since the intensity of the image obtained is proportional to the number of droplets and their surface area. As a result, areas of the spray with low liquid density are not captured in the experiment. This is demonstrated in Figure 42, where the liquid droplets, as predicted in KIVA are compared with a contour plot of the *parmie* variable.

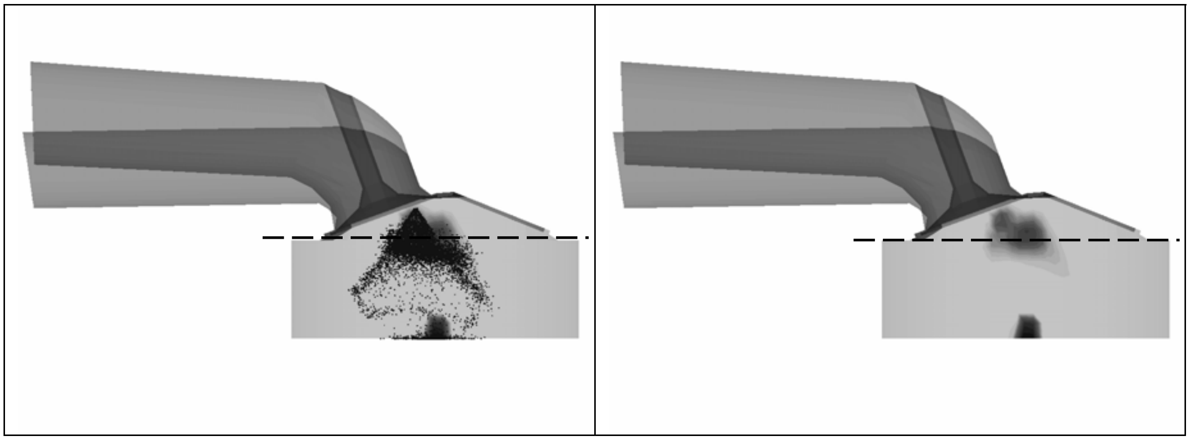

Figure 42: Comparison of liquid droplets and Mie Scattering variable, *parmie*, in KIVA

The comparison of vertical symmetry planes in the engine is shown in

Figure 43 for timings 69°-66° bTDC and in Figure 44 for 65°-62° bTDC. On the left column the KIVA predictions are shown and on the right the experimental observations. In Figure 45 and Figure 46 horizontal planes for the same timings are shown, acquired at the plane shown in Figure 42.

69	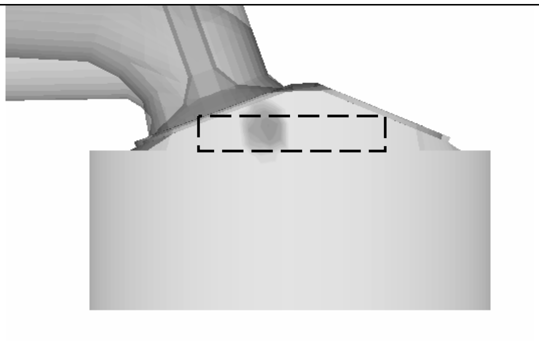	
68	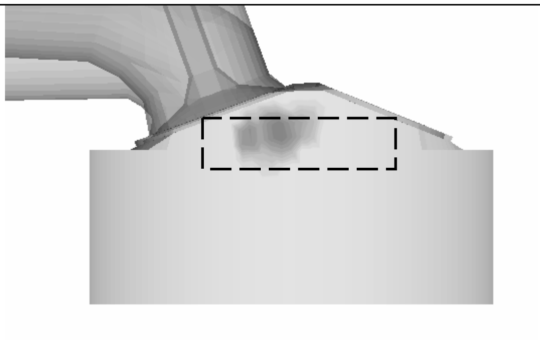	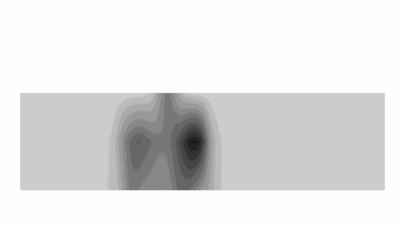
67	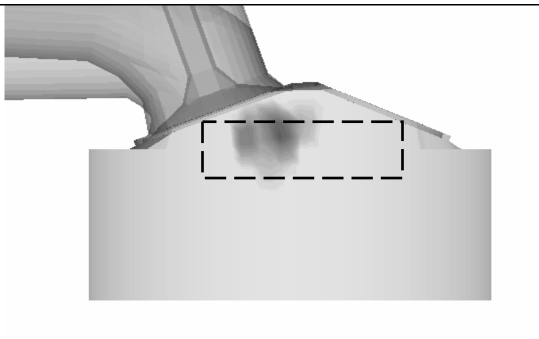	
66	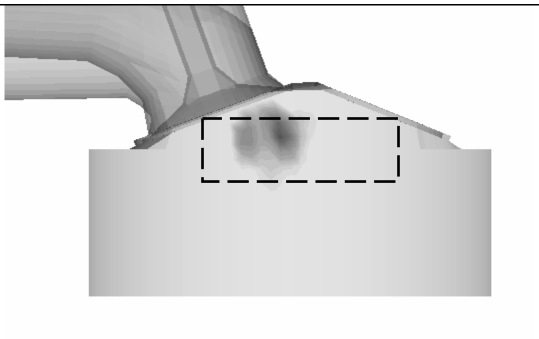	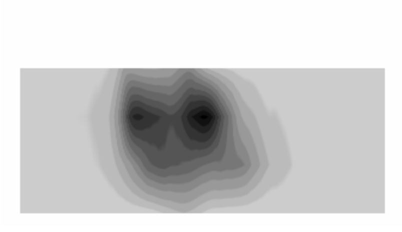

Figure 43: Comparison of Mie Scattering images, vertical view, KIVA (left column) vs. experiment (right column), 69°-66° bTDC

65	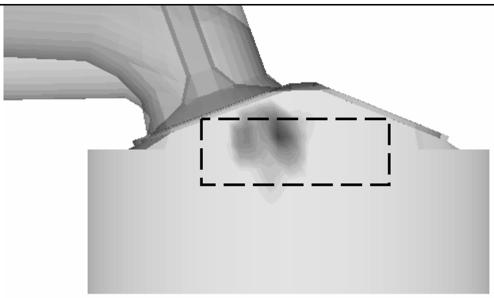	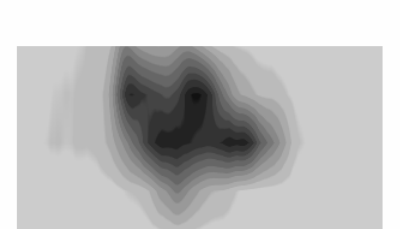
64	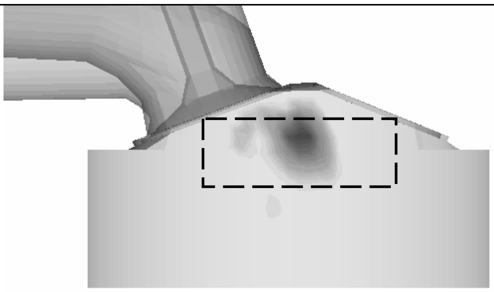	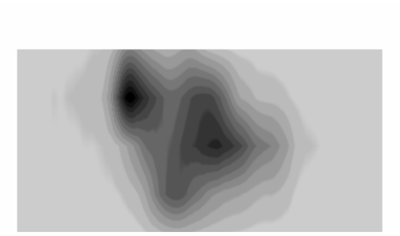
63	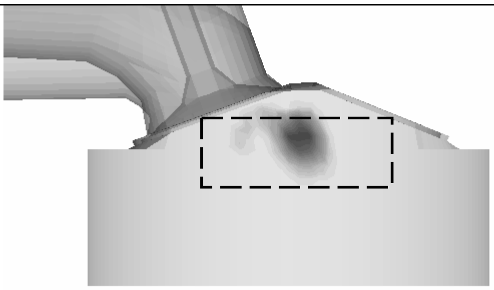	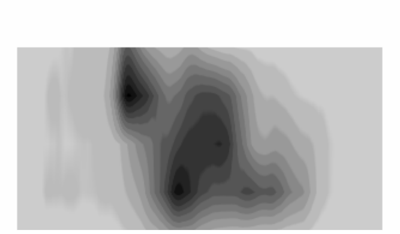
62	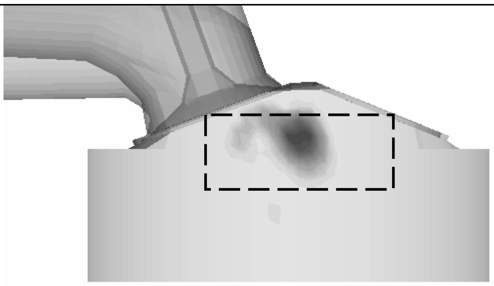	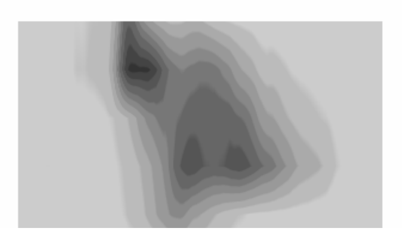

Figure 44: Comparison of Mie Scattering images, vertical view, KIVA (left column) vs. experiment (right column), 65°-62° bTDC

69	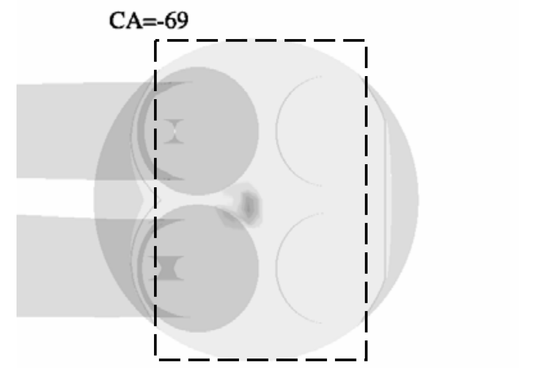	
68	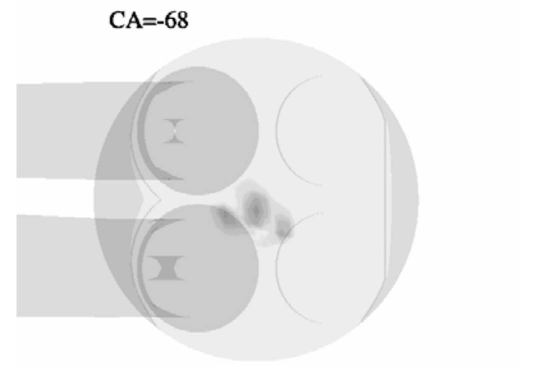	
67	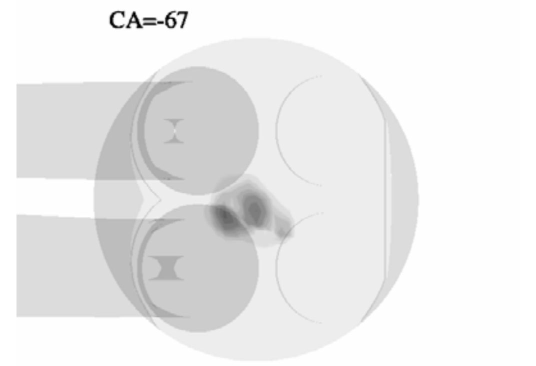	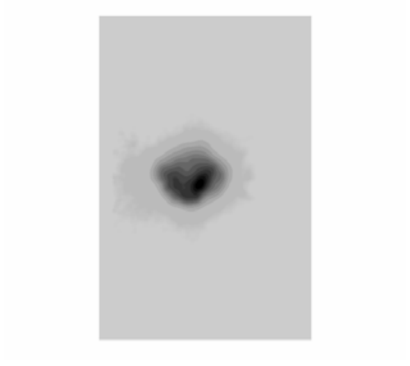
66	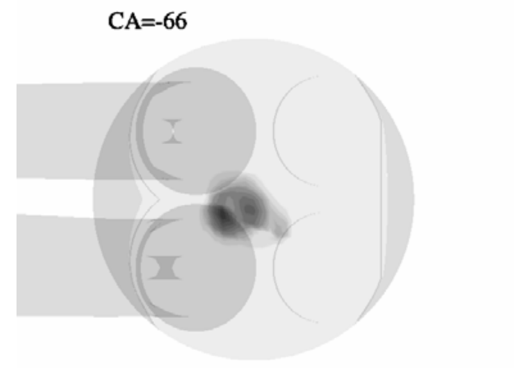	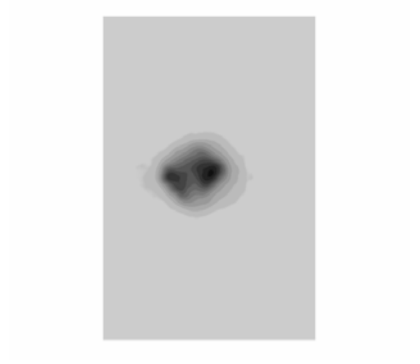

Figure 45: Comparison of Mie Scattering images, horizontal view, KIVA (left column) vs. experiment (right column), 69°-66° bTDC

65	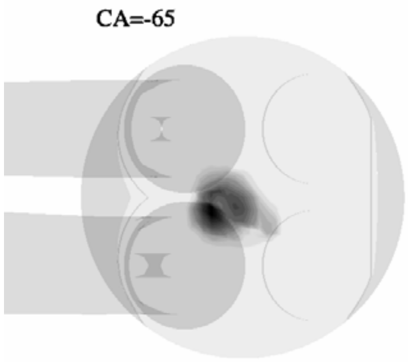	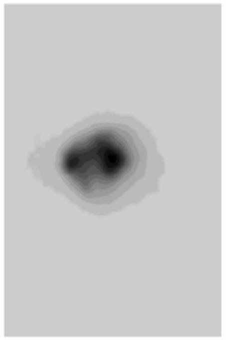
64	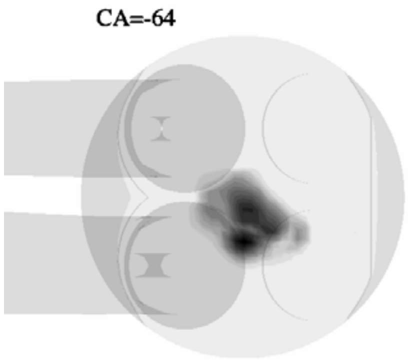	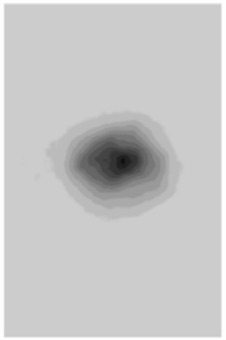
63	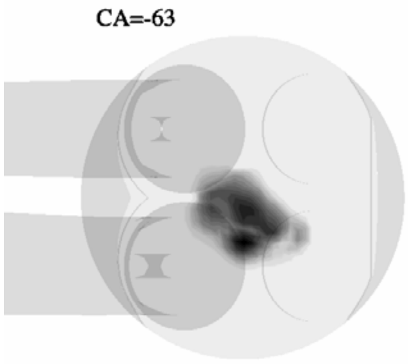	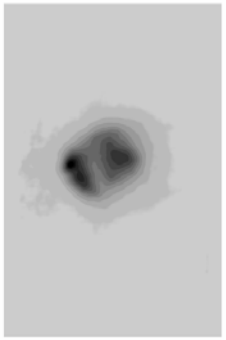
62	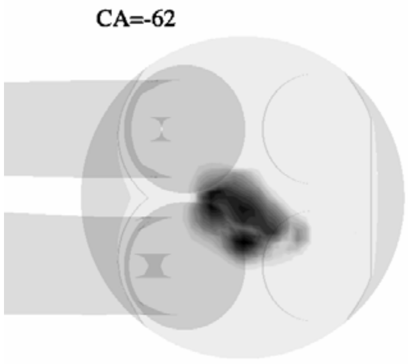	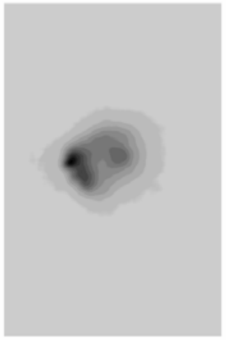

Figure 46: Comparison of Mie Scattering images, horizontal view, KIVA (left column) vs. experiment (right column), 65°-62° bTDC

In Figure 43 and Figure 44 the symmetry plane of the engine is shown and the experimental images cover the area indicated in the left column with a dashed box. The size of the experimental image grows with time, as the area covered with the liquid spray also increases. The agreement between the CFD results and the experiment is reasonably good. Both images show two dark areas, indicating the two sides of the hollow-cone spray. Also, the overall shape of the observed structure is very similar between the predictions and the experiment. The effect of the swirl is also demonstrated in Figure 45 and Figure 46 by the dark areas rotating around the axis of injection. The agreement is satisfactory in this case as well, both in terms of the surface area of the observed liquid spray, as well as the rotating dark areas representing the periphery of the spray.

5.3.2 Direct Injection Diesel Engine

Multiple injection strategies are used in diesel engines in order to reduce both smoke and NO_X emissions by achieving partially homogeneous mixtures, as demonstrated by Lechner et al. [2005]. The fuel injection pressure was set to 100 MPa and the injection timings were 52º bTDC for the pilot injection and 2º bTDC for the main injection. The corresponding cylinder pressures were 0.5 MPa for the pilot and 4.6 MPa for the main injection. The spray evolution for both injections is shown in Figure 47.

The elevated cylinder pressure in the second case leads to higher gas densities and, consequently, Weber numbers. Therefore a larger amount of droplets is expected to be found in the catastrophic breakup regime. In Figure 48 the secondary atomization regimes for the two fuel sprays are shown. In the pilot injection the majority of the droplets disintegrates according to the shear breakup mechanism, while in the main injection the droplets are almost evenly split between the shear and catastrophic mechanisms.

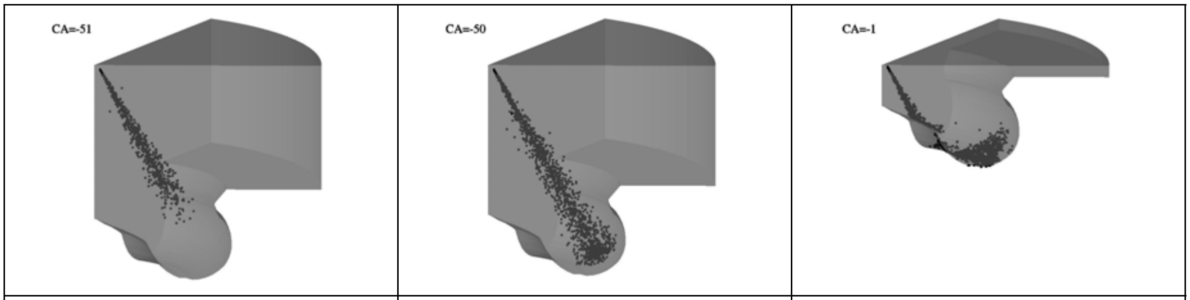

51º bTDC | 50º bTDC | 2º bTDC

Figure 47: Fuel spray evolution of a split injection in a partially homogeneous diesel engine

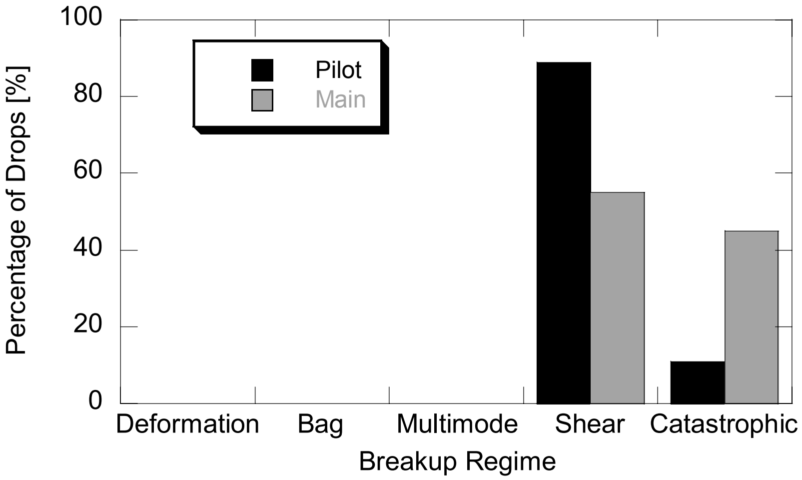

Figure 48: Secondary breakup mechanisms for the two injections of a typical split injection in a partially homogeneous diesel engine

CHAPTER 6

CONCLUSIONS AND RECOMMENDATIONS FOR FUTURE WORK

6.1 Summary

A comprehensive model for the primary and secondary atomization of liquid sprays under high injection pressures has been developed. The primary atomization modeling for high pressure swirl sprays (hollow cone sprays) is based on previous work by [Schmidt et al., 1999, Senecal et al., 1999]. For diesel sprays, which are typically solid-cone jets, the work of Huh et al. [1998] has been adopted, assuming a turbulence induced wave growth process resulting in the disintegration of the liquid core.

The secondary atomization has been divided in four regimes, namely the bag, multimode, shear and the catastrophic breakup regime. In the bag breakup regime a bag and a ring develop and disintegrate into smaller droplets. In multimode breakup a bag and a ring form, as well as a plume and a core drop, depending on the Weber number. In the shear breakup regime a boundary layer stripping model has been used, based on experimental observations by Chou et al., [1997]. The catastrophic atomization process is modeled using an instability analysis that leads to drop fragmentation. Subsequently, the resulting fragments disintegrate following the same boundary layer stripping mechanism encountered in shear breakup.

The model validation has been performed by comparing the model predictions with experimental measurements of isolated drops for the shear breakup mechanism as well as fully-developed non-evaporating gasoline and diesel sprays, covering the entire range of typical automotive applications, from very low to very high Weber numbers. The agreement with experimental data is very good with small discrepancies that can be explained considering that this is a generic model appropriate for a very wide range of applications. In most cases the discrepancies can be the result of uncertainties in the primary breakup modeling.

6.2 Conclusions

The study of secondary atomization regimes has proved the need to use appropriate models for each breakup regime, in order to capture the entire range of physical processes occurring during spray breakup. It was concluded that the bag and multimode atomization regimes are mostly important for gasoline sprays, with the shear breakup mechanism playing a secondary role in extreme cases of high injection and cylinder pressures. For diesel sprays, the shear and catastrophic atomization regime are the dominant mechanisms for droplet breakup, while the multimode becomes significant for combinations of low injection and cylinder pressures. The fact that all breakup regimes are encountered in typical fuel spays in modern internal combustion engines illustrates the need for a unified model that covers the entire range of conditions.

It was concluded from the comparison of CFD predictions with experimental observations for diesel sprays that the coupling of the internal flow in the nozzle, including cavitation phenomena, with the primary atomization model is very important for the accurate prediction of the spray behavior. This coupling will provide the necessary boundary conditions, such as percentage of the orifice covered by vapor, velocity profile, to initialize the primary atomization model, thus leading to more accurate predictions of spray breakup.

The comparison of model predictions with experimental data from realistic fuel injectors has also demonstrated the significance of quantifying the experimental error due to uncertainties in the measuring equipment or due to hardware imperfections. A characteristic example are multihole diesel injector nozzles with asymmetrical fuel jets due to manufacturing imperfections that cause the liquid jets to have varying penetrations and droplet sizes. In this case the average values as well as the maximum and minimum values should be indicated in order to perform a meaningful comparison with CFD results.

Finally, it has been shown that high ambient pressures can affect the spray dynamics, primarily in the area close to the nozzle. This is a due to the high liquid density that affects momentum interactions between neighboring droplets, mainly by changing their aerodynamic drag coefficient. A correction for closely-spaced drops should be introduced in order to account for this effect and provide accurate predictions for the aerodynamic forces experienced by the droplets.

6.3 Contributions

The most important contribution of this work is the development of a comprehensive, unified model for the primary and secondary atomization of typical fuel sprays in internal combustion engine applications. The primary atomization depends on the type of injector but the secondary atomization is common for all sprays. The advantage of this approach is the simplicity offered to the user and the fact that further calibration is not required. When a new injector is introduced the primary atomization model will have to be modified accordingly but the main part of the model (drop deformation and secondary breakup) will remain unchanged.

For the first time it has been demonstrated that a spray breakup model can be used in a wide range of applications ranging from gasoline to diesel sprays with satisfying accuracy for all of them. In addition, it has been demonstrated that different operating conditions in the same engine require the modeling of many different atomization regimes. Therefore a unified model is a valuable tool in order to predict the spray breakup over the entire map of operating conditions and injection strategies of an engine.

Last, but definitely not least, a significant contribution is the review of all major spray models and their critical evaluation. Their strengths and limitations have been analyzed and the atomization regimes they represent have been identified. This is a useful classification that shows in which cases these models can be used with confidence. Furthermore, the physical mechanisms relevant for fuel sprays in internal combustion engines have been summarized.

6.4 Recommendations for Future Work

It has been shown in this work that a generic model can be applied for a wide range of fuel injection applications for internal combustion engines. However there is still lack of detailed knowledge of the primary breakup mechanisms responsible for the initial disintegration of the fuel sprays. An analysis of the fuel injection system, including pressure fluctuations, coupled with a detailed modeling of the internal flow in the nozzle can provide valuable initial conditions for spray modeling. In addition, an Eulerian approach can be applied for the primary atomization to provide more accurate predictions for the liquid jet or sheet breakup as well as for the initial droplet size. The coupling of the upstream processes with the spray modeling will also allow predictions of phenomena such as cavitation induced breakup when two injections are taking place very close in the same engine cycle, as observed by Roth et al. [2005].

As far as the secondary atomization modeling is concerned, corrections for dense sprays can be introduced, as discussed by Grover [2005]. Additionally, the effect of droplet collision and coalescence should be investigated by performing detailed experiments with dense sprays, such as the solid-cone sprays used in diesel applications. These experiments should be designed to provide insight on the frequency of the collisions and on their effect on the colliding droplets. Also the effect of dense sprays on the transition between secondary breakup regimes should be established [Legsfeld et al., 2002].

BIBLIOGRAPHY

1. Aalburg, C., van Leer, B., Faeth, G.M., Deformation and Drag Properties of Round Drops Subjected to shock Wave Disturbances, *AIAA*, vol. 41, No. 12, December 2003
2. Amsden A.A., KIVA-3: A KIVA Program with Block-Structured Mesh for Complex Geometries, Los Alamos National Laboratory LA-12503-MS, 1993
3. Amsden A.A., KIVA-3V: A Block-Structured KIVA Program for Engines with Vertical or Canted Valves, Los Alamos National Laboratory LA-13313-MS, July 1997
4. Amsden A.A., O'Rourke P.J., Butler T.D., KIVA II – A Computer Program for Chemically Reactive Flows with Sprays, Los Alamos National Laboratory LA-11560-MS, 1989
5. Arcoumanis, C., Gavaises, M., Linking Nozzle Flow with Spray Characteristics in a Diesel Fuel Injection System, *Atomization and Sprays*, vol. 8, pp. 307-347, 1998
6. Bayvel L., Orzechowski Z., *Liquid Atomization*, Taylor & Francis, 1993
7. Brennen, C.E., *Cavitation and Bubble Dynamics*, Oxford University Press, 1995
8. Chou, W.-H., Faeth, G.M., Temporal Properties of Secondary Drop Breakup in the Bag Breakup Regime, *Int. J. Multiphase Flow*, vol. 24, pp. 889-912, 1998
9. Chou, W.-H., Hsiang, L.-P., Faeth, G.M., Temporal Properties of Drop Breakup in the Shear Breakup Regime, *Int. J. Multiphase Flow*, vol. 23, No. 4, pp.651-669, 1997
10. Chryssakis C. Modeling Gasoline Sprays Emerging from High-Pressure Swirl Injectors for DISI Engines, M.Sc. Thesis, The University of Michigan, August 2002

11. Chryssakis, C.A., Assanis, D.N., Lee, J.-K., Nishida, K., Fuel Spray Simulation of High-Pressure Swirl-Injector for DISI Engines and Comparison with Laser Diagnostic Measurements, *SAE Technical Paper Series* 2003-01-0007, 2003
12. Chryssakis, C.A., Assanis, D.N., Lee, J.-K., Nishida, K., An Investigation of the Breakup Mechanisms for Swirl Sprays from High-Pressure Swirl Injectors, *9th International Conference on Liquid Atomization & Spray Systems*, Sorrento, Italy, July 2003
13. Chryssakis, C.A., Driscoll, K.D., Sick, V., Assanis, D.N., Validation of an Enhanced Liquid Sheet Atomisation Model Against Quantitative Laser Diagnostic Measurements, *18th Annual Conference on Liquid Atomization and Spray Systems*, Zaragoza, Spain, 9-11 September 2002
14. Clift, R., Grace, J.R., Weber, M.E., *Bubbles, Drops and Particles*, Academic Press, 1978
15. Dai, Z., Faeth, G.M., Temporal Properties of Secondary Drop Breakup in the Multimode Breakup Regime, *Int. J. Multiphase Flow*, vol. 27, pp. 217-236, 2001
16. Dombrowski N., Johns W.R., The Aerodynamic Instability and Disintegration of Viscous Liquid Sheets, *Chem. Eng. Sci.*, vol.18, pp. 203-214, 1963
17. Dorfner V., Domnick J., Durst F., Koehler R., Viscosity and Surface Tension Effects in Pressure Swirl Atomization, *Atomization and Sprays*, vol. 5, pp. 261-285, 1995
18. Faeth G.M., Dynamics of Secondary Drop Breakup –A Rate Controlling Process in Dense Sprays, Invited review article, *ILASS-Europe 2002*, Zaragoza, Spain, 9-11 September 2002
19. Faeth, G.M., Hsiang, L.-P., Wu, P.-K., Structure and Breakup Properties of Sprays, *Int. J. Multiphase Flow,* Vol. 21, Suppl. pp. 99-127, 1995
20. Fishburn, B.D., Boundary layer stripping of liquid drops fragmented by Taylor instability, *Acta Astronautica*, vol. 1, pp. 1267-1284, Pergamon Press, 1974

21. Fissenewert, U., The Design of a Single Cylinder Engine Featuring Optical Access, Diploma Thesis, Technische Universitaet Berlin, 1999
22. Fraser and Eisenklam, Research into the Performance of Atomizers for Liquids, *Imp. Coll. Chem. Eng. Soc. L.*, vol. 7, pp.52-68, 1953
23. Gelfand, B.E., Droplet Breakup Phenomena in Flows with Velocity Lag, *Prog. Energy Combust. Sci.*, vol. 22, pp. 201-265, 1996
24. Grover, R.O., A Methodology for CFD predictions of spark-ignition direct-injection engine conical sprays combining improved physical submodels and system optimization, Ph.D. Thesis, The University of Michigan, 2005
25. Habchi, C., Verhoeven, D., Huynh Huu, C., Lambert, L., Vanhemelryck, J.L., Baritaud, T., Modeling Atomization and Break Up in High-Pressure Diesel Sprays, *SAE Technical Paper Series* 970881, 1997
26. Han Z., Parrish Sc., Farell P.V., Reitz R.D., Modeling Atomization Processes of Pressure-Swirl Hollow-Cone Fuel Sprays, *Atomization and Sprays*, vol. 7, pp. 663-684, 1997
27. Helenbrook, B.T., Edwards, C.F., Quasi-Steady Deformation and Drag of Uncontaminated Liquid Drops, *Int. J. Multiphase Flow*, vol. 28, pp. 1631-1657, 2002
28. Heywood J.B., *Internal Combustion Engine Fundamentals*, McGraw-Hill, 1988
29. Hinze, J.O., Fundamentals of the Hydrodynamic Mechanism of Splitting in Dispersion Processes, *AIChE*, 1, pp.289-295, 1955
30. Hsiang, L.-P., Faeth, G.M., Drop Deformation and Breakup due to Shock Wave and Steady Disturbances, *Int. J. Multiphase Flow*, vol. 21, No. 4, pp. 545-560, 1995
31. Hsiang L.-P., Faeth, G.M., Drop Properties after Secondary Breakup, *Int. J. Multiphase Flow*, vol.19, No. 5, pp. 721-735, 1993
32. Hsiang, L.-P., Faeth, G.M., Near-Limit Drop Deformation and Secondary Breakup, *Int. J. Multiphase Flow*, vol.18, No. 5, pp. 635-652, 1992

33. Huh, K.Y., Lee, E., Koo, J.-Y., Diesel Spray Atomization Model Considering Nozzle Exit Turbulence Conditions, *Atomization and Sprays*, vol. 8, pp. 453-469, 1998
34. Ibrahim, E.A., Yang, H.Q., Przekwas, A.J., Modeling of Spray Droplets Deformation and Breakup*, J. Propulsion Power*, vol. 9, No. 4, pp. 651-654, 1993
35. Krzeczkowski, S.A., Measurement of Liquid Droplet Disintegration Mechanisms, *Int. J. Multiphase Flow*, vol. 6, pp.227-239, 1980
36. Kubo, M., Sakakida, A., Iiyama, A., Technique for Analyzing Swirl Injectors of Direct-Injection Gasoline Engines, *SAE Technical Paper Series* 2001-01-0964, 2001
37. Lechner, G.A., Jacobs, T.J., Chryssakis, C.A., Assanis, D.N., Siewert R.M., Evaluation of A Narrow Spray Cone Angle, Advanced Injection Timing Strategy to Achieve Partially Premixed Compression Ignition Combustion in a Diesel Engine, *SAE 2005 Transactions, 2005-01-0167*, 2005
38. Lee J., Nishida K., Analyses of Pre-Swirl Spray Formation and its Breakup Processes of D.I. Gasoline Spray, *ICLASS 2003*, Sorrento, Italy, 2003
39. Lefebvre A.H., *Atomization and Sprays*, Hemisphere Publishing Corporation, 1989
40. Lengsfeld C.S., Delplanque J.-P., Dunn-Rankin D., Breakup Transitions within Dense Sprays, *Atomization and Sprays*, vol. 12, pp. 501-511, 2002
41. Lin, S.P., Reitz, R.D., Drop and Spray Formation from a Liquid Jet, *Annu. Rev. Fluid Mech.,*vol. 30, pp. 85-105, 1998
42. Liu, A.B., Mather, D., Reitz, R.D., Modeling the Effects of Drop Drag and Breakup on Fuel Sprays, *SAE Technical Paper Series* 930072, 1993
43. Liu, A.B., Reitz, R.D., Mechanisms of Air-Assisted Liquid Atomization, *Atomization and Sprays*, vol. 3, pp. 55-75, 1993
44. Munson, B.R., Young, D.F., Okiishi, T.H., *Fundamentals of Fluid Mechanics*, 2nd edition, John Wiley & Sons, 1994
45. Nicholls, J., Stream and Droplet Breakup by Shock Waves, NASA SP-194, pp. 126-128, 1972

46. O'Rourke, P.J., Amsden, A.A., The TAB Method for Numerical Calculation of Spray Droplet Breakup, *SAE Technical Paper Series* 872089, 1987
47. Park, J.-H., Yoon, Y., Hwang, S.-S., Improved TAB Model for Prediction of Spray Droplet Deformation and Breakup, *Atomisation and Spray Technology*, vol. 12, No.4, pp. 387-402, 2002
48. Patterson, M.A., Reitz, R.D., Modeling the Effects of Fuel Spray Characteristics on Diesel Engine Combustion and Emission, *SAE Technical Paper Series* 980131, 1998
49. Pilch M., Erdman C.A., Use of Breakup Time Data and Velocity History Data to Predict the Maximum Size of Stable Fragments for Acceleration-Induced Breakup of a Liquid Drop, *Int. J. Multiphase Flow*, vol. 13, No. 6, pp. 741-757, 1987
50. Ponti, F., Characterization of the fuel injection, evaporation and mixing in an unthrottled optical SIDI using quasi-3-dimensional imaging, M.Sc. Thesis, The University of Michigan, 2002
51. Pope, S.B., *Turbulent Flows*, Cambridge University Press, 2001
52. Powell, C.F., Yue, Y., Liu, J., Cheong, S.-K., Instantaneous Mass Measurement of Fuel Sprays Using Time-Resolved X-Radiography, *15th Annual Conference on Liquid Atomization and Spray Systems*, Madison, WI, May 2002
53. Ranger, A.A., The Aerodynamic Shattering of Liquid Drops, Ph.D. Thesis, The University of Michigan, 1968
54. Ranger, A.A., and Nichols, J.A., Aerodynamic Shattering of Liquid Drops, *AIAA*, 7, pp.285-290, 1969
55. Reitz, R.D., Modeling Atomization Processes in High-Pressure Vaporizing Sprays, *Atomisation and Spray Technology*, vol. 3, pp. 309-337, 1987
56. Reitz, R.D., Diwakar, R., Structure of High-Pressure Fuel Sprays, *SAE Technical Paper Series* 870598, 1987
57. Roth, H., Giannadakis, E., Gavaises, M., Arcoumanis C., Omae, K., Sakata, I., Nakamura, M., Yanagihara, H., Effect of Multi-Injection Strategy on Cavitation

Development in Diesel Injector Hole Nozzles, *SAE Technical Paper Series* 2005-01-1237, 2005

58. Schlichting, H., *Boundary layer theory*, 6th ed., McGraw-Hill, 1968
59. Schmidt, D.P., Corradini, M.L., The internal flow of diesel fuel injector nozzles: a review, *Int. J. Engine Research*, vol. 2, No. 1, 2001
60. Schmidt, D.P., Nouar, I., Senecal, P.K., Rutland, C.J., Martin, J.K., Reitz, R.D., Pressure-Swirl Atomization in the Near Field, *SAE Technical Paper Series* 1999-01-0496, 1999
61. Senecal, P.K., Schmidt, D.P., Nouar, I., Rutland, C.J., Reitz, R.D., Corradini, M.L., Modeling high-speed viscous liquid sheet atomization, *Int. J. of Multiphase Flow*, 25, pp. 1073-1097, 1999
62. Siebers, D.L., Liquid-Phase Fuel Penetration in Diesel Sprays, *SAE Technical Paper Series* 980809, 1998
63. Soteriou, C., Andrews, R., Smith, M., Direct Injection Diesel Sprays and the Effect of Cavitation and Hydraulic Flip on Atomization, *SAE Technical Paper Series* 950080, 1995
64. Squire, H.B., Investigation of the Instability of a Moving Liquid Film, *Br. J. Appl. Phys.*, vol. 4, pp. 167-169, 1953
65. Tanner, F.X., Liquid Jet Atomization and Droplet Breakup Modeling of Non-Evaporating Diesel Fuel Sprays, *SAE Technical Paper Series* 970050, 1997
66. Taylor, G.I., The instability of liquid surfaces when accelerated in a direction perpendicular to their planes, *Proc. Royal Soc*. A. 201, pp. 192-196, 1950
67. Vanzieleghem, B., Combustion Modeling For Gasoline Direct Injection Engines Using KIVA-3V, Ph.D. Thesis, The University of Michigan, 2004
68. Vanzieleghem, B., Chryssakis, C., Grover, R., Assanis, D., Im, H., Sick, V., Modeling of Gasoline Direct Injection Mixture Formation Using KIVA-3V: Development of Spray Breakup and Wall Impingement Models and Validation with

Optical Engine Planar Laser Induced Fluorescence, *COMODIA 2004*, Yokohama, Japan, August 2004

69. v. Berg, E., Edelbauer, W., Alajbegovic, A., Tatschl, R., Volmajer, M., Kegl, B., Ganippa, L.C., Coupled Simulations of Nozzle Flow, Primary Fuel, Jet Breakup, and Spray Formation, *ASME J. of Eng. for Gas Turbines and Power*, vol. 127, No. 1, 2005
70. White, *Viscous Fluid Flow*, 2nd edition, McGraw-Hill, 1990
71. Yue, Y., Powell, C., Cuenca, R., Poola, R., Wang, J., Parrish, S.E., Measurement of Gasoline Spray Propagation by means of Synchrotron X-Ray, *15th Annual Conference on Liquid Atomization and Spray Systems*, Madison, WI, May 2002